NOTICE

The quality of this microform is heavily dependent upon the quality of the original thesis submitted for microfilming. Every effort has been made to ensure the highest quality of reproduction possible.

If pages are missing, contact the university which granted the degree.

Some pages may have indistinct print especially if the original pages were typed with a poor typewriter ribbon or if the university sent us an inferior photocopy.

Reproduction in full or in part of this microform is governed by the Canadian Copyright Act, R.S.C. 1970, c. C-30, and subsequent amendments.

AVIS

La qualité de cette microforme dépend grandement de la qualité de la thèse soumise au microfilmage. Nous avons tout fait pour assurer une qualité supérieure de reproduction.

S'il manque des pages, veuillez communiquer avec l'université qui a conféré le grade.

La qualité d'impression de certaines pages peut laisser à désirer, surtout si les pages originales ont été dactylographiées à l'aide d'un ruban usé ou si l'université nous a fait parvenir une photocopie de qualité inférieure.

La reproduction, même partielle, de cette microforme est soumise à la Loi canadienne sur le droit d'auteur, SRC 1970, c. C-30, et ses amendements subséquents.

UNIVERSITY OF ALBERTA

A 4 GHz CRYOGENIC NOISE PARAMETER MEASUREMENT SYSTEM

by

HENRIK JOHANSEN

A THESIS

SUBMITTED TO THE FACULTY OF GRADUATE STUDIES AND RESEARCH IN PARTIAL FULFILLMENT OF THE REQUIREMENTS FOR THE DEGREE OF MASTER OF SCIENCE

DEPARTMENT OF ELECTRICAL ENGINEERING

EDMONTON, ALBERTA

FALL 1991

ISBN 0-315-70195-1

UNIVERSITY OF ALBERTA

RELEASE FORM

NAME OF AUTHOR: HENRIK JOHANSEN

TITLE OF THESIS: A 4 GHz CRYOGENIC NOISE PARAMETER MEASUREMENT SYSTEM

DEGREE: MASTER OF SCIENCE

YEAR THIS DEGREE GRANTED: FALL 1991

Henrik Johansen

6165 38 Avenue

Edmonton, Alberta, Canada

T6L 2Z1

Date: August 26th, 1991

University of Alberta

Faculty of Graduate Studies and Research

The undersigned certify they have read, and recommend to the Faculty of Graduate Studies and Research for acceptance, a thesis entitled A 4 GHz CRYOGENIC NOISE PARAMETER MEASUREMENT SYSTEM submitted by HENRIK JOHANSEN in partial fulfillment of the requirements for the degree of MASTER OF SCIENCE.

D. Routledge

.....

Dr. D. Routledge
Supervisor

.....

Dr. J. F. Vaneldik
Supervisor

.....

Dr. A. E. Peterson

.....

Dr. W. R. Tinga

Date: August 20th, 1991

Abstract

A method of measuring the noise and scattering parameters of microwave devices at cryogenic temperatures is described. Principles of obtaining corrected S-parameters are discussed and several methods compared using a sensitivity analysis. The applicability of the error correcting techniques for various analyzer systems is discussed.

A complete derivation of the system of noise measurement is presented, including input tuner loss compensation and a new method of correction for the loss of the cryostat input cable. A numerical simulation is used to verify this method.

Useful details are also included concerning the construction of the necessary hardware components. Drawings and operation of calibration fixtures, cryogenic input tuner, and a stepper motor controller for manual or computer control of the tuner are provided.

Acknowledgements

I would like to express my appreciation for the efforts of Dr. D. Routledge and Dr. J. F. Vaneldik for their supervision and financial support of this project. Additionally, the contributions of the following are gratefully acknowledged:

- Dr. E. C. Valk and Mr. G. Miller for friendly encouragement and numerous useful discussions
- Mr. R. Schmaus for his capable technical assistance
- Dr. W. R. Tinga and Dr. W. A. G. Voss for the use of their S-parameter test system and other instruments
- Mr. P. W. K. Candy for his encouragement to undertake this project
- the examining comittee for reviewing this work
- the Department of Electrical Engineering for providing teaching assistantships

Finally I am grateful to my family for their support and encouragement throughout the project. In particular, thanks to Ramona Whyte for her love and continued understanding.

Table of Contents

Chapter page

1. Introduction....1
   1.1 Radio Astronomy Requirements....1
   1.2 Thesis Organization....2
   1.3 Thermal Noise....3
2. Scattering Parameter Measurement....9
   2.1 Parameter Sets....9
      2.1.1 Scattering Parameters....9
      2.1.2 Scattering Transfer Parameters....11
      2.1.3 R-Parameters....12
   2.2 Scattering Parameter Measurement Techniques....13
      2.2.1 Overview....13
      2.2.2 Vector Automatic Network Analyzers....14
      2.2.3 The HP8410 System....15
      2.2.4 The HP8510 System....20
   2.3 Error Vector Models....21
      2.3.1 Basic Principles....21
      2.3.2 One Port, Four Error Vector Model....24
      2.3.3 Two Port, Eight Error Vector Model....25
      2.3.4 Two Port, Twelve Error Vector Model....32
         2.3.4.1 The OSLT Method....32
         2.3.4.2 The 3ST Method....36
         2.3.4.3 The LRL Method....39
   2.4 Sensitivity Analysis of Error Vector Models....43
      2.4.1 Sensitivity Analysis and Results....43
      2.4.2 LRL Failure Analysis....53

2.5 Cryogenic Measurtment Considerations.....69
3. Noise Parameter Measurement.....72
3.1 Noise Parameter Representation.....72
3.2 Noise Sources and the Noise-Temperature Diagram....76
3.3 The Y-factor Method.....80
3.4 Noise Parameter Measurement
by the Y-factor Method.....83
3.5 Mismatch Factors.....85
3.6 Tuner Loss Compensation Techniques.....86
3.6.1 Method of Strid.....86
3.6.2 Method of Martines and Sannino.....88
3.6.3 The New Loss Compensation Method.....90
3.6.3.1 Tuner Loss Compensation.....91
3.6.3.2 Cryogenic Measurements.....97
3.6.3.3 Tuner Bypass Correction.....105
3.6.3.4 Receiver Isolator Available
Gain Correction.....108
3.7 Effects of Feedback and Cascade Networks
on Noise Parameters.....113
4. Measurement Apparatus.....117
4.1 Introduction.....117
4.2 Cryogenic Equipment Configuration.....117
4.2.1 S-parameter Measurement.....119
4.2.2 Noise Parameter Measurement.....121
4.3 Measurement Apparatus External to the Cryostat....124
4.3.1 S-parameter Measurement Subsystem.....124
4.3.2 Noise Figure Measurement Subsystem.....126

4.3.3 Motor Drive Subsystem.....129
4.4 Calibration and Test Fixtures.....129
4.5 Cryogenic Tuner.....134
4.6 Stepper Motor Controller.....142
4.6.1 Stepper Motor Fundamentals.....143
4.6.1.1 Variable Reluctance Motors.....144
4.6.1.2 Permanent Magnet Motors.....146
4.6.2 Stepper Control Card Circuit.....146
4.6.2.1 Controller Design Description.....146
4.6.2.2 Functional Description.....150
4.6.2.3 Detailed Circuit Description.....153
4.6.2.4 Drive Circuits.....161
5. Experimental Results.....165
5.1 Noise Measurement Simulation.....165
5.1.1 Numerical Simulation Program.....165
5.1.2 Simulation Results.....168
5.2 S-parameter Measurements.....182
5.3 Experimental Noise Measurements.....184
5.3.1 HEMT Measurements.....184
5.3.2 Passive DUT Measurements.....189
6. Recommendations and Conclusions.....193
6.1 Recommendations.....193
6.1.1 System Hardware.....193
6.1.2 Experimental Procedures.....196
6.2 Conclusions.....197
References.....199
Appendix I Noise Parameter Conversions.....205

Appendix II Initial Configuration of J12 on
stepper motor control card.....210
Appendix III Table of Motor Control Card IC Functions....211
Appendix IV Remote Command (IEEE-488) Summary.....212
Appendix V Table of Motor Control Card Jumpers.....214

List of Tables

Table page

2.1 Sensitivity of error vectors to errors in measured standards using the OSLT calibration method.....54

2.2 Sensitivity of error vectors to errors in measured standards using the 3ST calibration method.....55

2.3 Sensitivity of error vectors to errors in measured standards using the LRL calibration method.....56

2.4 Sensitivity of load to errors in measured standards using the OSLT calibration method.....57

2.5 Sensitivity of open to errors in measured standards using the OSLT calibration method.....57

2.6 Sensitivity of direct short to errors in measured standards using the OSLT calibration method.....58

2.7 Sensitivity of offset short ($\Gamma = 1.0 \angle 60^{\circ}$) to errors in measured standards using the OSLT calibration method.....58

2.8 Sensitivity of offset short ($\Gamma = 1.0 \angle -60^{\circ}$) to errors in measured standards using the OSLT calibration method.....59

2.9 Sensitivity of thruline to errors in measured standards using the OSLT calibration method.....59

2.10 Sensitivity of thruline (90° elec. length) to errors in measured standards using the OSLT calibration method.....60

2.11 Sensitivity of load to errors in measured standards using the 3ST calibration method.....60
2.12 Sensitivity of open to errors in measured standards using the 3ST calibration method.....61
2.13 Sensitivity of direct short to errors in measured standards using the 3ST calibration method.....61
2.14 Sensitivity of offset short ($\Gamma = 1.0 \angle 60^{\circ}$) to errors in measured standards using the 3ST calibration method.....62
2.15 Sensitivity of offset short ($\Gamma = 1.0 \angle -60^{\circ}$) to errors in measured standards using the 3ST calibration method.....62
2.16 Sensitivity of thruline to errors in measured standards using the 3ST calibration method.....63
2.17 Sensitivity of thruline (90° elec. length) to errors in measured standards using the 3ST calibration method.....63
2.18 Sensitivity of load to errors in measured standards using the LRL calibration method.....64
2.19 Sensitivity of open to errors in measured standards using the LRL calibration method.....64
2.20 Sensitivity of direct short to errors in measured standards using the LRL calibration method.....65
2.21 Sensitivity of offset short ($\Gamma = 1.0 \angle 60^{\circ}$) to errors in measured standards using the LRL calibration method.....65
2.22 Sensitivity of offset short ($\Gamma = 1.0 \angle -60^{\circ}$) to errors in measured standards using the

LRL calibration method.....66
2.23 Sensitivity of thruline to errors in measured standards using the LRL calibration method.....66
2.24 Sensitivity of thruline (90° elec. length) to errors in measured standards using the LRL calibration method.....67

List of Figures

Figure page

1.1 Two-port noise representations.....6

1.2 Connection of a source admittance to input of a two-port.....8

2.1 Scattering parameters for a linear two-port network....9

2.2 Chain of two-port networks characterized by T-parameters.....12

2.3 A simplified vector network analyzer.....14

2.4 Simplified diagram of the HP8746B S-parameter test set.....18

2.5 The HP8410 VANA system.....19

2.6 S-parameter test set switching arrangement for the HP8510 series VANA.....22

2.7 One-port error vector model.....23

2.8 Single port error vector model.....24

2.9 Two-port, eight error vector model.....26

2.10 The two port, twelve error vector model.....31

2.11 Graphical interpretation of the sensitivity analysis of error vector E to measured standard M.....52

3.1 Graphical representation of noise figure F as a function of source reflection coefficient..73

3.2 Physical interpretation of two-port noise temperature.74

3.3 Apparatus for measurement of RX noise temperature.....78

3.4 Noise-temperature diagram for the apparatus of Figure 3.3.....79

3.5 Graphical interpretation of the Y-factor

calibration step.....81
3.6 Apparatus for measurement of DUT noise temperature....82
3.7 Graphical interpretation of the Y-factor
measurement step.....82
3.8 Noise parameter measurement apparatus
(Y-factor method).....84
3.9 Calibration of mismatched system.....92
3.10 Estimation of inserted network loss.....94
3.11 Calibration of the tuner noise temperature
inside a cryostat.....101
3.12 N-T diagram for the configuration of
Fig. 3.11(a) and (b).....102
3.13 Configuration for the measurement of DUT noise
figure using noise calibration at
the tuner output.....105
3.14 Replacement of the tuner with a two-port
bypass network.....106
3.15 Various two-port connections.....113
4.1 Schematic of the measurement apparatus interior
to the cryostat. Exterior components
shown for S-parameter measurement.....118
4.2 Schematic of the measurement apparatus interior
to the cryostat. Exterior components
shown for noise parameter measurement.....122
4.3 S-parameter measurement system.....125
4.4 Noise parameter measurement system.....127
4.5 Isometric drawing of assembled test fixture.....130
4.6 Detailed drawings of test fixture components.....131

4.7 Stripline conductor patterns.....132
4.8 Source lead shorting blocks.....133
4.9 Cryogenic tuner mechanical drawing.....136
4.10 Square slab-line geometry.....137
4.11 Smith Chart calculation of the tuner range.....139
4.12 Tuner range estimated by numerical computation.....140
4.13 A three phase variable reluctance motor.....144
4.14 Operation of a three phase VR motor.....147
4.15 A hybrid motor with small angular step size.....147
4.16 Operation of a permanent magnet stepper motor showing use of bidirectional current drive.....148
4.17 Block diagram of the stepper motor controller card..151
4.18 (1 of 2) Schematic of main stepper motor controller board.....155
4.18 (2 of 2) Schematic of piggyback counter board and 7-segment display board.....156
4.19 Stepper motor controller board component and jumper location.....157
4.20 Simplified PM motor driving circuit.....162
4.21 Motor drive circuit (as built).....163
5.1 The apparatus as modelled in the simulation.....167
5.2 Simulated measurement of T_{DUT} and $G_{A,DUT}$ with no tuner loss or isolator noise.....170
5.3 Simulation with lossy tuner and noiseless isolator; no tuner loss compensation.....171
5.4 Simulation with lossy tuner and noiseless isolator; single tuner loss compensation at $\Gamma = 0$...172

5.5 Simulation with lossy tuner and noiseless isolator; three loss compensations performed.....173
5.6 Simulation with lossless tuner and noisy isolator; single tuner loss compensation.....175
5.7 Simulation with lossy tuner and noisy isolator; no tuner loss compensation.....176
5.8 Simulation with lossy tuner and noisy isolator; single tuner loss compensation at Γ =0....177
5.9 Simulation with lossy tuner and noisy isolator; tuner loss compensation at three points...178
5.10 Simulation of HEMT measurement with noiseless isolator; and full tuner loss compensation.....180
5.11 HEMT simulation with noisy isolator and lossy tuner; and full tuner loss compensation.....181

Chapter 1

Introduction

1.1 Radio Astronomy Requirements

Radio Astronomy requires receiving equipment which contributes the lowest possible noise to the weak signals being detected. Reduction of unwanted noise is achieved primarily by improving antennas, feed structures and low noise amplifiers. The last decade has seen great improvements in low-noise microwave transistor performance, and many instruments have been upgraded with better amplifiers. Cryogenic amplifier operation, despite the added complexity it imposes, is required for best results. This thesis discusses methods of measuring the noise parameters of a cooled transistor, to provide the information necessary for optimizing amplifier design.

Obtaining the microwave noise parameters of a transistor while cooled to cryogenic temperatures presents a number of difficulties. Detection of the small noise powers generated requires accounting for the noise produced by the measurement system. Some form of variable impedance is needed, which is available inside the cryostat, and whose noise properties are either known a priori or can be determined as part of the measurement procedure. A noise source, with noise power calibration somehow extended to the cryogenic transistor is also required. Finally, the reflection coefficients seen by the transistor must be measured, possibly requiring calibration of a vector

reflectometer to a reference plane inside the cryostat.

1.2 Thesis Organization

This thesis discusses the methods used to overcome these problems, including a new method of noise source calibration for use inside the cryostat. Emphasis is placed on producing a working hardware system for measurement of cryogenic noise parameters and scattering parameters.

Literature reviews are contained at the beginning of the appropriate sections, since the author believes this resulted in a better organized and more readable document. This chapter will present some of the basic noise theory as an introduction to the field. Chapter 2 of this thesis concerns the measurement of scattering parameters and associated calibration methods. This material is presented first, since no noise theory is used in the analysis presented. Chapter 3 discusses noise theory and noise measurement techniques. A novel calibration method is introduced, and the requirements of the experimental apparatus are deduced.

The implementation of the noise parameter measurement method is contained in Chapter 4. Details of the apparatus constructed, particularly a remotely controlled cryogenic tuner, are discussed. Simulation and experimental results are presented in Chapter 5. Conclusions, and proposals for further improvements are contained in the last chapter, Chapter 6.

1.3 Thermal Noise

The field of electrical noise theory began in 1928 with publications by Johnson [1.1] and Nyquist [1.2]. Johnson had measured the e.m.f. of electrical noise in a conductor; he attributed this potential to thermally induced motion of charged carriers. Nyquist confirmed Johnson's results with a theoretical derivation of the expectation of the thermal noise voltage across an open circuited resistor. For a resistance R at physical temperature T, this voltage is given by

$$\langle v_n^2 \rangle = \frac{4\,R\,h\,f\,\Delta f}{e^{hf/kT} - 1} \qquad (1.1)$$

where v_n is the r.m.s. noise voltage

R is the resistance value

h is Planck's constant (6.26×10^{-34} J·s)

k is Boltzmann's constant (1.38×10^{-23} J/K)

T is the absolute temperature

f is the measurement frequency

Δf is the measurement bandwidth

$\langle\ \rangle$ is the expectation operator.

The expectation operator is used since v_n is a stochastic, ergodic and stationary variable and is therefore described by its statistical properties. Over the range of frequencies and temperatures considered in this thesis, the above equation can be approximated (using a series expansion for the exponential function) by the relation

$$\langle v_n^2 \rangle = 4\ R\ k\ T\ \Delta f. \qquad (1.2)$$

The noise power available from a resistor (or other lossy passive device) at temperature T is therefore

$$P = k\ T\ \Delta f \tag{1.3}$$

where P is the average noise power.

Several fundamental properties can be deduced from equations (1.2) and (1.3):

1. Available noise power depends only on the temperature of the resistor, and is therefore independent of the value and composition of the resistor.
2. Measured noise power will be proportional to the measurement system bandwidth, Δf.
3. The noise power spectrum is identical for all lossy materials at the same temperature.

Friis [1.3] proposed a definition of noise figure of a two-port, which was defined in terms of the available signal to noise ratios, such that

$$F = \frac{(S/N)_{IN}}{(S/N)_{OUT}} \tag{1.4}$$

where F is the noise figure

$(S/N)_{IN}$ is the available signal to noise ratio at the input

$(S/N)_{OUT}$ is the available signal to noise ratio at the output.

Although Friis did not use the decibel scale in his paper,

it has become common to express F in units of dB, given by

$$F_{dB} = 10 \log_{10} (F) \qquad (1.5)$$

where F_{dB} is the noise figure expressed in decibels.

The benefits of using the noise figure can be seen by considering the equation which gives the overall noise temperature of a system of N cascaded two-ports:

$$F_{SYS} = F_1 + \frac{F_2}{G_1} + \frac{F_3}{G_1 G_2} + \ldots + \frac{F_N}{G_1 G_2 G_3 \ldots G_{N-1}} \qquad (1.6)$$

where F_{SYS} is the total system noise figure

F_i is the noise figure of the i'th two-port

G_i is the available gain of the i'th two-port.

Equation 1.6 has become known as the "Friis Equation".

Although important, Friis' work did not address the effect of the source impedance on the noise figure. Rothe and Dahlke [1.4] resolved the problem by introducing the concept of representing a noisy two-port (Fig 1.1(a)) by a noiseless two-port with external current and/or voltage noise generators (Fig 1.1(b) through (d)). In general, two noise sources are required to describe a two-port; furthermore, these generators are partially correlated. The correlation coefficient is given by

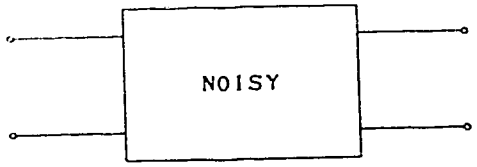

(a) Two-port network with internal noise sources

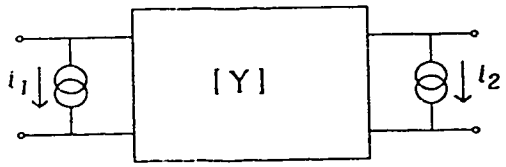

(b) Noise-free two-port with two external noise current generators

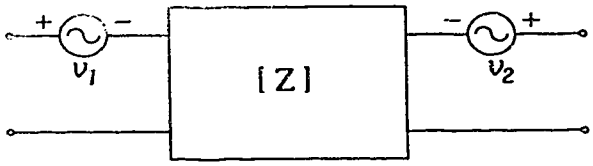

(c) Noise-free two-port with two external noise voltage generators

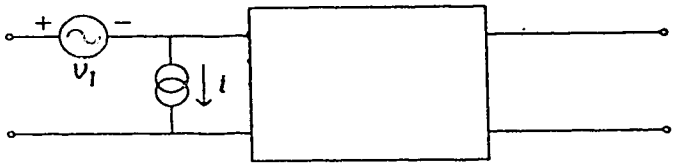

(d) Noise-free two-port with one voltage and one current noise generator at the input port

Figure 1.1: Two-port noise representations

$$\alpha = \frac{\langle i v^* \rangle}{\sqrt{\langle i i^* \rangle \langle v v^* \rangle}}$$

where α is the correlation coefficient,

$*$ is the complex conjugate operator,

v is the noise voltage, and

i is the noise current,

as shown in Figure 1.1(d).

The four quantities Re{α}, Im{α}, $\langle v v^* \rangle$, and $\langle i i^* \rangle$ (or their equivalents in other representations) constitute the four "noise parameters" which, together with the circuit parameters (eg. S-parameters) fully describe the noise behavior of the network.

Rothe and Dahlke also introduced the concept of noise tuning, used to minimize the two-port noise figure by achieving an optimum "noise match" between the signal source and the input port of the two-port (see Figure 1.2). This relationship between noise figure and source admittance is given [1.5] by

$$F = F_{min} + \frac{R_n}{G_s} |Y_s - Y_{opt}|^2 \qquad (1.7)$$

where F is the two-port noise figure for any value of Y_s.

F_{min} is the minimum achievable noise figure

Y_s is the admittance of the source

connected to the input of the two-port

Y_{opt} is the optimum value of Y_s

R_n is a slope factor

$G_s = \mathrm{Re}\{Y_s\}$.

In equation 1.7, the values of F_{min}, R_n, $\mathrm{Re}\{Y_{opt}\}$ and $\mathrm{Im}\{Y_{opt}\}$ constitute the set of four noise parameters. Conversion between this and other sets of noise parameters is given in Appendix I.

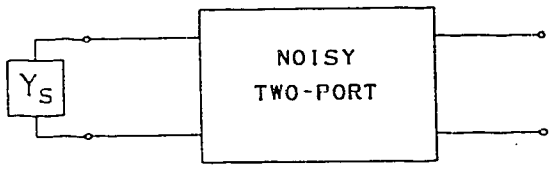

Figure 1.2: Connection of source admittance (Y_S) to input of a two-port

The remainder of this thesis concerns methods for obtaining the four noise parameters for a cryogenically cooled microwave FET transistor. Combined with the device scattering parameters, a complete estimate of the FET characteristics, suitable for low-noise amplifier design, is obtained.

Chapter 2

Scattering Parameter Measurement

2.1 Parameter Sets

2.1.1 Scattering Parameters

The behaviour of electrical n-port networks is often characterized in terms of terminal voltages or currents. At microwave frequencies, measuring such quantities, without disturbing the electromagnetic fields of the variables being sampled (and therefore altering the system being measured), is extremely difficult.

Scattering parameters, or S-parameters, describe the network behaviour in terms of incident and emerging sinusoidal electromagnetic waves at the frequency of interest. This definition permits the use of sampling techniques (eg. directional couplers) which minimize field perturbations as a source of measurement error. Although S-parameters are defined for n-port networks, this thesis will consider only two-port and single port applications.

An arbitrary, linear, two-port network (N) is

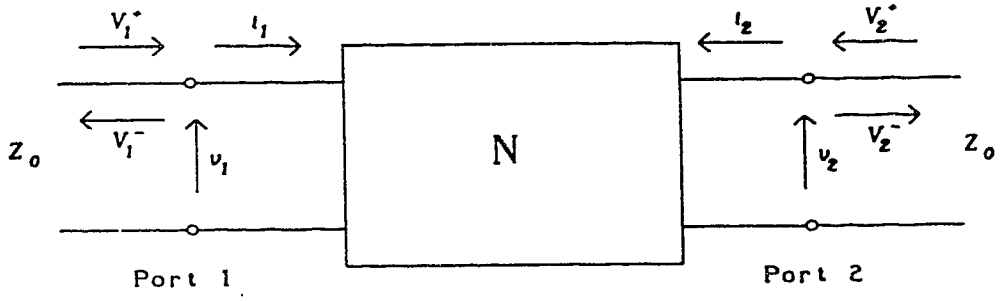

Figure 2.1: Scattering parameters for a linear two-port network. Characteristic impedance of the transmission line is Z_0.

illustrated in Figure 2.1. The incident and emerging waves, denoted a_i and b_i respectively, where i is the port number, are given [2.1] by the relations:

$$a_i = \frac{V_i^+}{\sqrt{Z_0}} \qquad \text{where} \quad i = 1,2 \qquad (2.1)$$

Z_0 = characteristic impedance of line

V_i^+ = incident wave voltage at port i

and

$$b_i = \frac{V_i^-}{\sqrt{Z_0}} \qquad \text{where} \quad i = 1,2 \qquad (2.2)$$

V_i^- = emergent wave voltage at port i.

In most practical applications, and throughout this thesis , the characteristic impedance, Z_0, is 50 ohms. Equations 2.1 and 2.2 can also be expressed in terms of the terminal voltages and currents,

$$a_i = \frac{v_i + i_i Z_0}{2\sqrt{Z_0}} \qquad \text{where} \quad i = 1,2 \qquad (2.3)$$

and

$$b_i = \frac{v_i + i_i Z_0}{2\sqrt{Z_0}} \qquad \text{where} \quad i = 1,2. \qquad (2.4)$$

The S-parameters are defined in terms of the variables a_i and b_i as

$$b_1 = S_{11}a_1 + S_{12}a_2 \qquad (2.5)$$

$$b_2 = S_{21}a_1 + S_{22}a_2 \qquad (2.6)$$

or, in matrix representation,

$$\mathbf{b} = \mathbf{Sa}. \tag{2.7}$$

2.1.2 Scattering Transfer Parameters

The incident and emerging wave variables a and b used to define the S-parameter matrix can also be employed to describe the scattering transfer parameters, or T-parameters.

T-parameters are defined to enable easy use of matrix algebra when calculating the effects of cascaded networks. In terms of the wave quantities, the T-parameters defined [2.2] by the relation

$$\begin{bmatrix} a_1 \\ b_1 \end{bmatrix} = \begin{bmatrix} T_{11} & T_{12} \\ T_{21} & T_{22} \end{bmatrix} \begin{bmatrix} b_2 \\ a_2 \end{bmatrix} . \tag{2.8}$$

The expressions relating S and T parameters are then

$$\begin{bmatrix} T_{11} & T_{12} \\ T_{21} & T_{22} \end{bmatrix} = \frac{1}{S_{21}} \begin{bmatrix} 1 & -S_{22} \\ S_{11} & S_{12}S_{21}-S_{11}S_{22} \end{bmatrix} \tag{2.9}$$

and

$$\begin{bmatrix} S_{11} & S_{12} \\ S_{21} & S_{22} \end{bmatrix} = \frac{1}{T_{11}} \begin{bmatrix} T_{21} & T_{22}T_{11}-T_{12}T_{21} \\ 1 & -T_{12} \end{bmatrix} . \tag{2.10}$$

T-parameters are useful for analysis of cascaded two-ports, as shown in Figure 2.2. The T-parameter matrix of this chain of networks T_s, is given by

$$\mathbf{T}_S = \mathbf{T}_A\mathbf{T}_B\mathbf{T}_C \ldots \mathbf{T}_N . \tag{2.11}$$

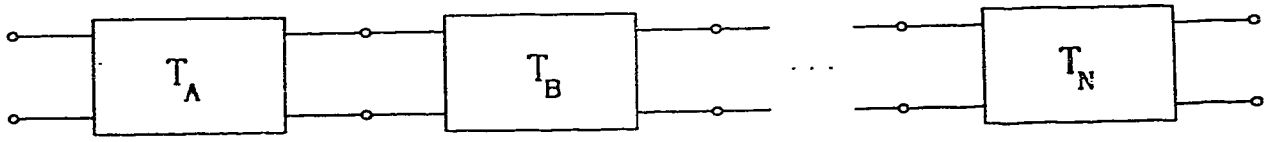

Figure 2.2: Chain of two-port networks characterized by T-parameters.

2.1.3 R-Parameters

R-parameters [2.1] are closely related to T-parameters. Interchanging the a and b variables in 2.8 yields the R matrix

$$\begin{bmatrix} b_1 \\ a_1 \end{bmatrix} = \begin{bmatrix} R_{11} & R_{12} \\ R_{21} & R_{22} \end{bmatrix} \begin{bmatrix} a_2 \\ b_2 \end{bmatrix} . \tag{2.12}$$

In terms of S-parameters, the R-parameters are

$$\begin{bmatrix} R_{11} & R_{12} \\ R_{21} & R_{22} \end{bmatrix} = \frac{1}{S_{21}} \begin{bmatrix} S_{12}S_{21}-S_{11}S_{22} & S_{11} \\ -S_{22} & 1 \end{bmatrix} \tag{2.13}$$

and the inverse relation is

$$\begin{bmatrix} S_{11} & S_{12} \\ S_{21} & S_{22} \end{bmatrix} = \frac{1}{R_{22}} \begin{bmatrix} R_{12} & R_{11}R_{22}-R_{12}R_{21} \\ 1 & -R_{21} \end{bmatrix} . \tag{2.14}$$

Similar to T-parameters, R-parameters are useful for the analysis of cascade connections of networks. The series of networks shown in Figure 2.2 could also be solved using R-parameters:

$$\mathbf{R_S = R_A R_B R_C \ldots R_N} \tag{2.15}$$

These properties are used in some de-embedding schemes which were used in the experimental work for this thesis.

2.2 Scattering Parameter Measurement Techniques

2.2.1 Overview

The techniques of measuring network parameters at microwave frequencies differ significantly from the techniques used at lower frequencies. At lower frequencies, direct observation of voltages and currents is often possible. Such a procedure usually cannot be performed at microwave frequencies without significantly disturbing the signals under investigation. Additionally, microwave measurements are usually to be made inside a shielded enclosure, or in a coaxial line of fixed impedance, where probing of the fields is difficult.

Historically, one of the first successful approaches was to employ a waveguide or coaxial slotted line, where the field sampling probe (it was hoped) introduced a minimum of measurement error. Despite widespread use, the method was slow, usually the desired quantities were not available from a direct readout, and the technique was unsuitable for automation.

An improved approach came with the development of the vector automatic network analyzer (VANA). This equipment uses directional couplers to sample both incident signal and either reflected or transmitted signal as required. A detection circuit determines the complex ratio of the two signals to obtain one of the four S-parameters. Various

arrangements have been provided to permit measurement of all four, depending on the manufacturer and model of the analyzer. The HP8410 equipment used for the experimental work of this thesis is one example, and will be discussed in further detail.

An alternative approach has been proposed by Engen [2.3]. The six-port network analyzer circumvents the complex ratio detection requirement, and uses only power magnitude measurements. Computational requirements exceed that of the VANA and this system cannot provide even crude measurements without computer support. Frequency sweeping is also not provided, and although measurements at several frequencies can be made, the convenience of having a "real-time" display for monitoring adjustments is lost.

2.2.2 Vector Automatic Network Analyzers

VANA systems, including error modelling and correction, have been evolving for some time. Hackborn [2.4] presented an early example of computerized error correction in 1968.

Figure 2.3 depicts a simple network analyzer system, usually called a reflectometer. The waves a_1, b_1, a_2, and b_2 are sampled by the directional couplers, yielding the

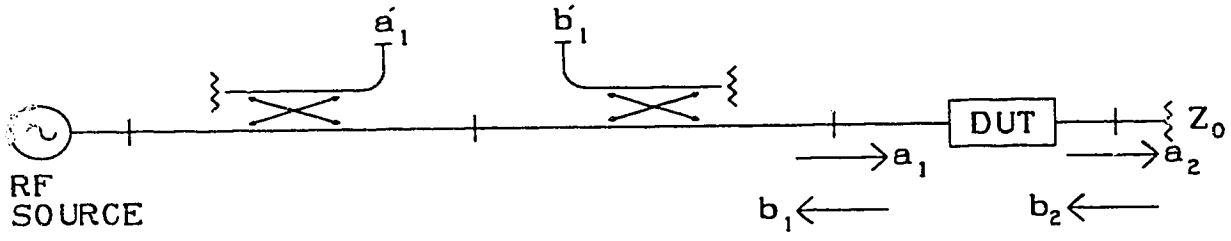

Figure 2.3: A simplified vector network analyzer.

quantities a'_1, b'_1, a'_2, and b'_2. Only two quantities can be sampled simultaneously with the hardware illustrated; reconnection of the couplers is necessary to obtain all four S-parameters. In principle, with identical, perfect directional couplers and a non-reflecting load, the complex ratios of the appropriate a' and b' values yield the desired S-parameters when corrected to the desired reference plane. Practical implementation of such a system involves three major items of interest:

a) the realization of complex ratio detection,

b) switching of the signal paths to permit two or four of the S-parameters to be measured without reconnection, and

c) minimization of coupler and load related errors and computer correction of these errors.

Solutions used for two commercial VANA systems will be discussed with regard to the methods employed to reduce or eliminate these problems.

2.2.3 The HP8410 System

This system was introduced by Hewlett-Packard in the late 1960's [2.5]. It consists of a number of compatible components, a subset of which would be procured to meet the user's display presentation and measurement frequency needs. Experimental work for this thesis was performed using a modified HP8410 system, and it is therefore described here in greater detail than other systems. Gaining an understanding of the operating principles of this

instrument, and correction of the errors inherent in the results obtained with it, formed an important part of the work described in this thesis. The "Line-Reflection-Line" (LRL) method of calibration (see section 2.3.4.3) was found to be unsuitable, although this was not apparent from the outset.

Figure 2.4 shows a simplified diagram of the RF portion of the HP8746B S-parameter test set. The RF input is supplied from an external oscillator, and a sample is provided to the reference output port. A line stretcher is provided to adjust the line length for this signal to match the desired reference plane of the test signal at either (but in general, not both) of the two ports. An attenuator sets the incident RF level supplied to the network being examined, usually referred to as the device under test (DUT). A set of six coaxial relays are switched to apply the incident RF signal to the appropriate port, and select the required reflected or transmitted sample for the test channel output. Terminations are applied to the coaxial signal paths as necessary. The output of the HP8746B consists of the reference signal and the test channel signal. One of the four S-parameters can be determined by the network analyzer from the complex ratio of these two microwave signals. Suitable switching permits measurement of all four S-parameters.

The test and reference signals are supplied to the HP8411A harmonic converter, as shown in Reference 2.5. Here the microwave signals are heterodyned to the first

intermediate frequency (IF) of 20.278 MHz. A voltage controlled oscillator (VCO) is used to drive a comb generator; one of the output harmonics is used to mix the incoming signals to the first IF.

The HP8410 network analyzer section peforms two functions. First, the 20.278 MHz IF test and reference signals are heterodyned to the second IF of 278 kHz. These IF outputs are supplied to the polar display section. The second function is to achieve phase locking of the comb generator in the harmonic converter. A phase detector compares the phase of the first IF of the reference channel and a 20.278 MHz crystal oscillator. The output of the phase detector is low pass filtered and amplified. Gain and bandwidth adjustments are required, because the VCO tuning sensitivity is proportional to the harmonic number used in phase locking. Lock detection circuits switch a triangular waveform to the VCO when the loop is unlocked. This causes the comb generator to sweep the band, with the intention of achieving a lock condition when one of the harmonics is 20.278 MHz higher or lower than the RF source frequency. Once the source signal has been captured the VCO drive is switched from the search circuit to the filtered phase detector output, thereby closing the phase locked loop.

The second IF signals are used by the HP8414A polar display unit which performs the complex ratio detection. Two balanced modulator circuits are used to extract the sine and cosine components of the complex ratio. This provides the S-parameter measurement desired in a rectangular form,

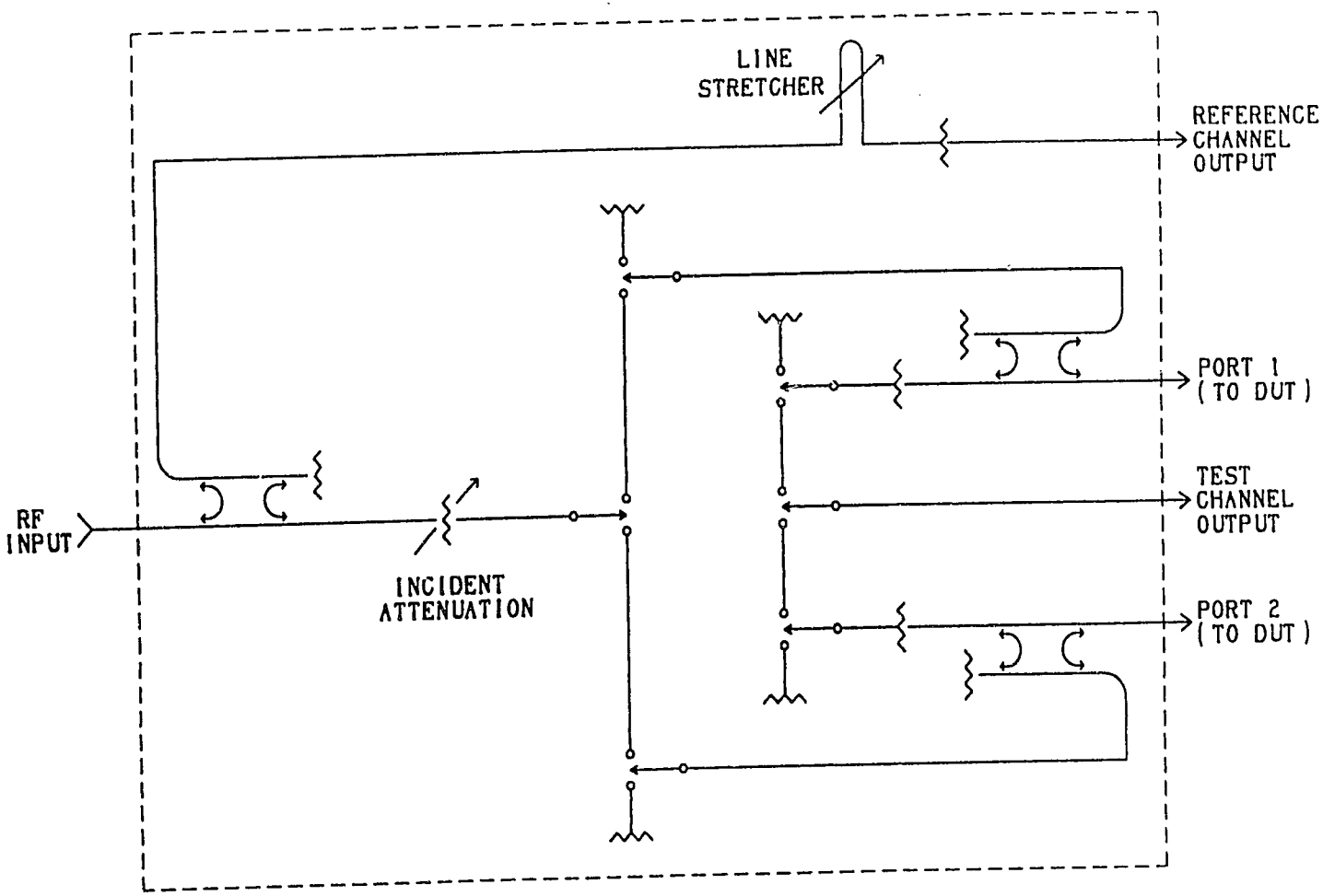

Figure 2.4: Simplified diagram of the HP8746B S-parameter test set.

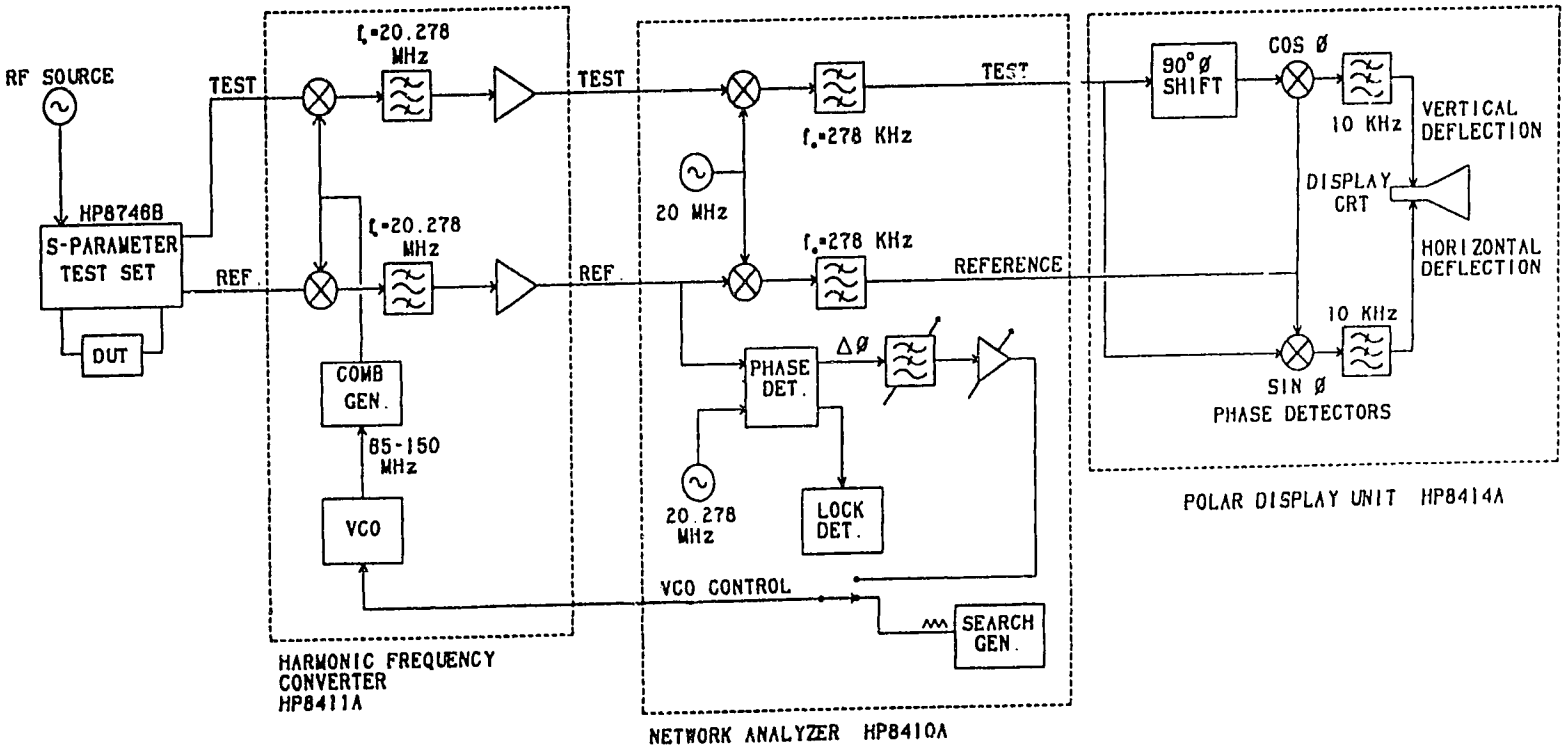

Figure 2.5: The HP8410 VANA system. Details of the HP8746B unit are shown in Figure 2.4. Certain functions are not implemented exactly as shown.

which is supplied to a CRT display.

No numerical correction of errors was available with the original HP8410 system. S-parameter data was displayed graphically on a CRT only. An advantage of the system is the ability to accommodate swept RF measurements, giving real-time feedback on the effects of DUT adjustment.

The system used for the measurements in this thesis has been modified to provide computer input of S-parameters using data acquisition of the vertical and horizontal CRT drive voltages. This provides measured, though uncorrected, values of S-parameters in rectangular form. Computer control of the various relays and other functions has also been incorporated, such that the control computer (HP-85) can obtain values for all four S-paramters under program control. The measurement control program "SPARAMS" also incorporates error correction, using techniques described later in this chapter.

2.2.4 The HP8510 System

The HP8510 system is Hewlett-Packard's successor to the HP8410 described in the previous section. Computer control, data aquisition, and error correction are provided with the system. The switching scheme in the S-parameter test set portion has been altered significantly as shown in Figure 2.6. Compared with the HP8410, switching has been simplified, and four directional couplers are used. This allows measurement of the four quantities (a_0, b_0, a_3, b_3 in Figure 2.6) in both switch positions.

The additional information is used to advantage in the error correction procedure. Repeatable errors caused by imperfect switching or termination effects can be removed using an eight error vector model (Figure 2.9) for each switch position. The thru-short-delay (TSD) method [2.6], a special case of the line-reflection-line (LRL) method, is often used for this calibration. Additionally, leakage errors analogous to E_{03} and E_{30} of Figure 2.10 can also be removed.

The measurement system used for the experimental portion of this thesis cannot utilize these improvements. Details of this improved correction algorithm have therefore not been included.

2.3 Error Vector Models

2.3.1 Basic Principles

The accuracy of VANA S-parameter measurements can be improved by various error correction methods. Modelling the imperfections in the instrument with a set of error vectors [2.7] is a common technique. Figure 2.7 illustrates the principle of ascribing the imperfections of the reflectometer apparatus to the existence of a fictitious error network (or "error box") which corrupts the measurement. Provided that the errors are repeatable, it may be possible to determine the effects of the error box. The measured values can then be corrected using the knowledge of these effects. Overall instrumentation accuracy, thereby, is enhanced.

Error vector correction consists basically of three

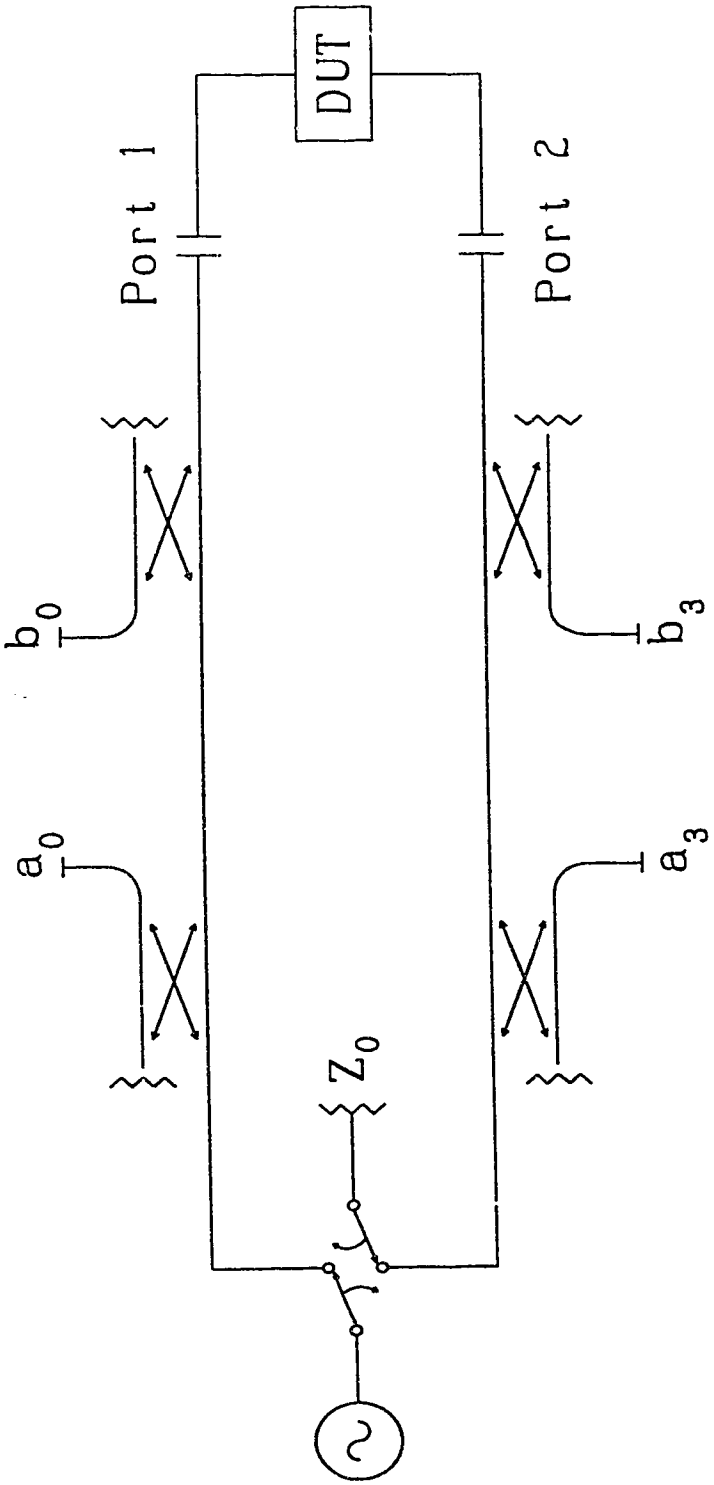

Figure 2.6: S-parameter test set switching arrangement for the HP8510 series VANA.

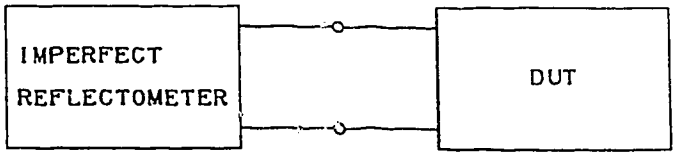

(a) Measurement apparatus.

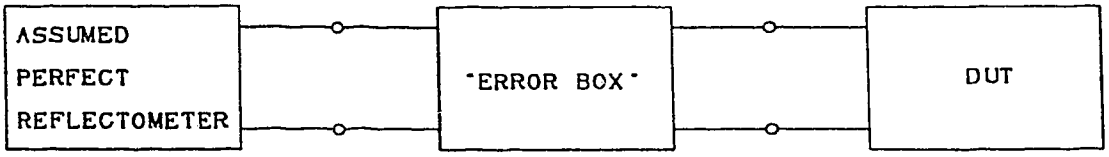

(b) Error model of the imperfect apparatus.

Figure 2.7: One-port error vector model.

steps. First, an appropriate model for the error terms, suitable for the instrument used, is selected. Second, a set of "standards" is chosen. These are networks with properties which can be determined a priori, usually from physical considerations. A sufficient number of unique standards is necessary to allow calculation of the error vectors. Third, with the standards and error vector model selected, the equations for error vector calculation and DUT de-embedding are determined, and are usually incorporated in some form of computer control system. Users of modern VANA systems are often provided with the error correction program by the vendor. The option of using differing sets of standards may also be provided.

Errors of a non-repeatable nature cannot be corrected by these methods. Typical examples include random noise in

the data and failure of connectors to mate repeatably. Measurement inaccuracies caused by non-linearities in instrumentation cannot be corrected either, since the models used contain insufficient parameters to characterize such errors.

2.3.2 One Port, Four Error Vector Model

Figure 2.8 shows the signal flow graph of a four error vector model for single port error correction. The actual DUT with reflection coefficient Γ_A, is assumed to be connected to the perfect measurement apparatus (which measures Γ_M) via a fictitious two-port error network consisting of E_{00}, E_{11}, E_{01}, and E_{10}. Γ_A cannot be measured directly, but is related to Γ_M by equation 2.16:

$$\Gamma_M = E_{00} + \frac{E_{01}E_{10}\Gamma_A}{1 - E_{11}\Gamma_A} \qquad (2.16)$$

Solution of the error network requires only the three terms E_{00}, E_{11}, and $E_{01}E_{10}$. Vectors E_{01} and E_{10} appear only as a product in these equations, therefore the individual values need not be determined. By using three different

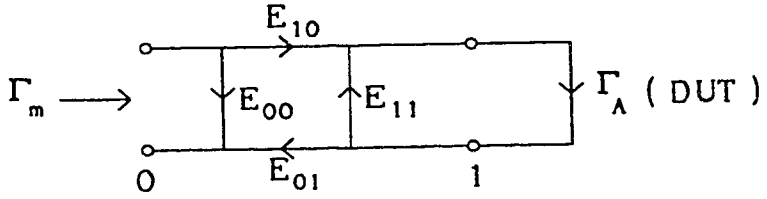

Figure 2.8: Single port error vector model.

reflection coefficients (A,B,C), the values of Γ_M (M_A, M_B, M_C respectively) can be measured. Substitution of these values into 2.16 provides three equations, which through algebraic manipulation yield the relationships required to solve for the error vectors:

$$E_{11} = \frac{(C-B)M_A + (A-C)M_B + (B-A)M_C}{A(C-B)M_A + B(A-C)M_B + C(B-A)M_C} \tag{2.17}$$

$$E_{00} = M_B - \frac{B(M_A-M_B)(1-AE_{11})}{(A-B)} \tag{2.18}$$

$$E_{01}E_{10} = \frac{(M_A-M_B)(1-AE_{11})(1-BE_{11})}{(A-B)} \; . \tag{2.19}$$

To de-embed the actual reflection coefficient of the DUT, Γ_A, and thereby correct the measured value Γ_M, the inverse relationship of equation 2.16 is used:

$$\Gamma_A = \frac{\Gamma_M - E_{00}}{E_{11}(\Gamma_M-E_{00}) + E_{01}E_{10}} \; . \tag{2.20}$$

The two-port calibration procedures discussed later also provide the values necessary for one-port calibration.

2.3.3 Two Port, Eight Error Vector Model

De-embedding a two-port DUT can be performed using the eight error vector model of Figure 2.9. The composite measured network is then considered to be a cascade connection of network A, the DUT, and network B. Expressing the parameters of the two error boxes and the DUT in terms

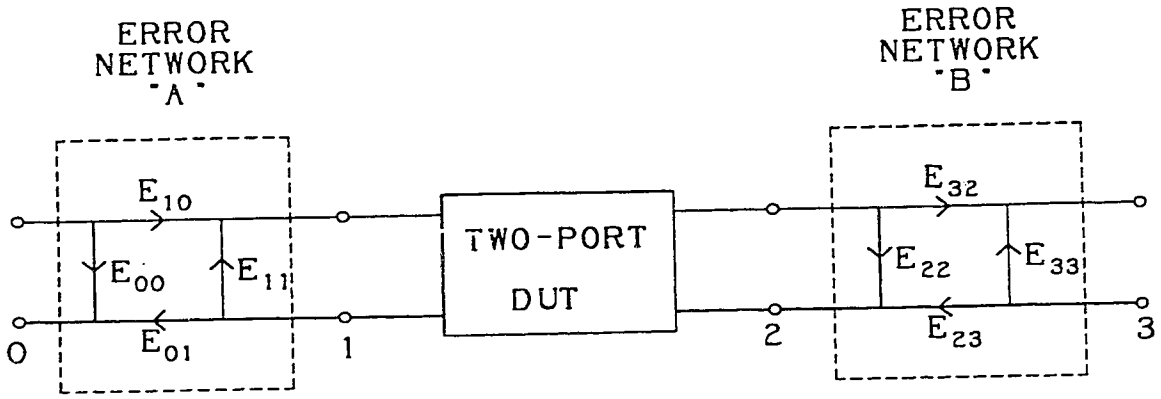

Figure 2.9: Two port, eight error vector model.

of T-parameters yields a single expression for the measured values:

$$T_M = T_A T_{DUT} T_B \tag{2.21}$$

The de-embedding equation is given by [2.8]:

$$T_{DUT} = T_A^{-1} \; T_M \; T_B^{-1} \tag{2.22}$$

where T_M = T-parameters of the measured network

T_A = T-parameters of error network A

T_{DUT} = T-parameters of the DUT

T_B = T-parameters of error network B

Soares [2.1] expresses the same relation, in terms of R-parameters:

$$R_{DUT} = R_A^{-1} \; R_M \; R_B^{-1} \tag{2.23}$$

where R_M = R-parameters of the measured network

R_A = R-parameters of error network A

R_{DUT} = R-parameters of the DUT

R_B = R-parameters of error network B

Values for the error vectors are established by measuring a number of known standards connected in place of the DUT. Sufficient data is thereby obtained to allow solution of eight quantities: E_{00}, E_{11}, E_{22}, E_{33}, $E_{01}E_{10}$, $E_{01}E_{23}$, $E_{10}E_{32}$, $E_{23}E_{32}$. The last four terms are not independent, as can be shown by

$$E_{01}E_{10} = \frac{E_{01}E_{23}\ E_{10}E_{32}}{E_{23}E_{32}} \ . \qquad (2.24)$$

The data is therefore overdetermined, and relation 2.24 can be employed to check self-consistency. Each of these four terms can be cross-checked in this manner.

The calibration standards chosen are three terminations at each port. This method is referred to as "three shorts plus thruline" or simply "3ST" calibration. The ideal S-parameters of these standards are assumed to be:

Standard #1 $\quad S_1 = \begin{bmatrix} A & 0 \\ 0 & D \end{bmatrix}$ ...two reflections

Standard #2 $\quad S_2 = \begin{bmatrix} B & 0 \\ 0 & F \end{bmatrix}$ ...two reflections

Standard #3 $\quad S_3 = \begin{bmatrix} C & 0 \\ 0 & G \end{bmatrix}$ ...two reflections

Standard #4 $\quad S_4 = \begin{bmatrix} 0 & H \\ H & 0 \end{bmatrix}$ ...thruline

Using the signal flowgraph of Figure 2.9 and applying

Mason's rule [2.9], the following equations describing the measured quantities in terms of the known standards and the unknown error vectors can be found.

Measurement of the reflection coefficients at port 1 for standards 1,2, and 3 gives:

$$M_A = E_{00} + \frac{A\ E_{01}E_{10}}{1 - A\ E_{11}} \tag{2.25}$$

$$M_B = E_{00} + \frac{B\ E_{01}E_{10}}{1 - B\ E_{11}} \tag{2.26}$$

$$M_C = E_{00} + \frac{C\ E_{01}E_{10}}{1 - C\ E_{11}} \tag{2.27}$$

where M_X is the measured value of the actual reflection coefficient X.

Similarly, at port 2:

$$M_D = E_{33} + \frac{D\ E_{23}E_{32}}{1 - D\ E_{22}} \tag{2.28}$$

$$M_F = E_{33} + \frac{F\ E_{23}E_{32}}{1 - F\ E_{22}} \tag{2.29}$$

$$M_G = E_{33} + \frac{G\ E_{23}E_{32}}{1 - G\ E_{22}} \tag{2.30}$$

Standard #4 yields

$$M_{00} = E_{00} + \frac{E_{01}E_{10}\ H^2E_{22}}{1 - H^2E_{11}E_{22}} \tag{2.31}$$

$$M_{03} = \frac{H\ E_{01}E_{23}}{1 - H^2E_{11}E_{22}} \tag{2.32}$$

$$M_{33} = E_{33} + \frac{E_{23}E_{32}\ H^2E_{11}}{1 - H^2E_{11}E_{22}} \tag{2.33}$$

$$M_{30} = \frac{H\ E_{10}E_{32}}{1 - H^2E_{11}E_{22}} \tag{2.34}$$

where M_{ij} is the measured transmission coefficient from port j to port i.

The preceding set of equations can be solved to provide the eight error vectors. The solution is presented below.

$$E_{11} = \frac{(C-B)M_A + (A-C)M_B + (B-A)M_C}{A(C-B)M_A + B(A-C)M_B + C(B-A)M_C} \tag{2.35}$$

$$E_{01}E_{10} = \left(\frac{1}{A-B}\right)(M_A-M_B)(1-E_{11}A)(1-E_{11}B) \tag{2.36}$$

$$E_{00} = M_A - \frac{E_{01}E_{10}A}{1-E_{11}A} \tag{2.37}$$

$$E_{22} = \frac{(G-F)M_D + (D-G)M_F + (F-D)M_G}{D(G-F)M_D + F(D-G)M_F + G(F-D)M_G} \tag{2.38}$$

$$E_{23}E_{32} = \left(\frac{1}{D-F}\right)(M_D - M_F)(1 - E_{22}D)(1 - E_{22}F) \tag{2.39}$$

$$E_{33} = M_D - \frac{E_{23}E_{33}D}{1 - E_{22}D} \tag{2.40}$$

$$E_{10}E_{32} = M_{03}\left(\frac{1}{H} - E_{11}E_{22}H\right) \tag{2.41}$$

$$E_{01}E_{23} = M_{30}\left(\frac{1}{H} - E_{11}E_{22}H\right) \tag{2.42}$$

As mentioned earlier, equation 2.23 can be used to de-embed the DUT; however, some additional manipulation is necessary. This problem results from the inability to separate the pairs of error vectors into their constituent components, which are required to solve the R-matrices. Consider the R_A and R_B matrices

$$R_A = \frac{1}{E_{10}} \begin{bmatrix} E_{01}E_{10}-E_{00}E_{11} & E_{00} \\ -E_{11} & 1 \end{bmatrix} \tag{2.43}$$

and

$$R_B = \frac{1}{E_{32}} \begin{bmatrix} E_{23}E_{32}-E_{22}E_{23} & E_{22} \\ -E_{33} & 1 \end{bmatrix} \tag{2.44}$$

where E_{10} and E_{32} are not available as separate entities. Analytic solution of the inversion of 2.43 and 2.44 provides matrices where the problem resolves itself, as shown below:

$$R_A^{-1} = \frac{1}{E_{01}E_{10}} \begin{bmatrix} 1 & E_{11} \\ -E_{00} & E_{01}E_{10}-E_{00}E_{11} \end{bmatrix} \tag{2.45}$$

$$R_B^{-1} = \frac{1}{E_{23}E_{32}} \begin{bmatrix} 1 & E_{33} \\ -E_{22} & E_{23}E_{32}-E_{22}E_{33} \end{bmatrix} \tag{2.46}$$

No difficulties of this nature are encountered with the R_M matrix, as all four S-parameters are determined by measurement. The eight vector model is useful for systems having error networks which meet the following criteria:

a) the network is repeatable between all measurements

b) the error vectors do not change when measuring

the four S-parameters

c) there is no "feed through" bypassing the DUT.

These criteria place some restrictions on the use of this error removal scheme. Connectors must be of reasonable quality to ensure repeatability. The instrumentation must exhibit minimal changes in the error-causing mechanisms when switching between S-parameters. Finally, there should be negligible internal leakage of signals between the measurement ports. Failure to meet these requirements may necessitate a more complex model.

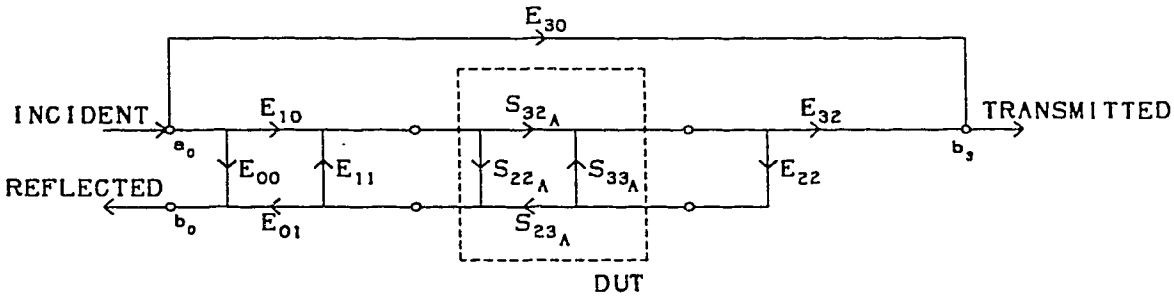

(a) Forward measurement of S_{11_M} and S_{21_M}.

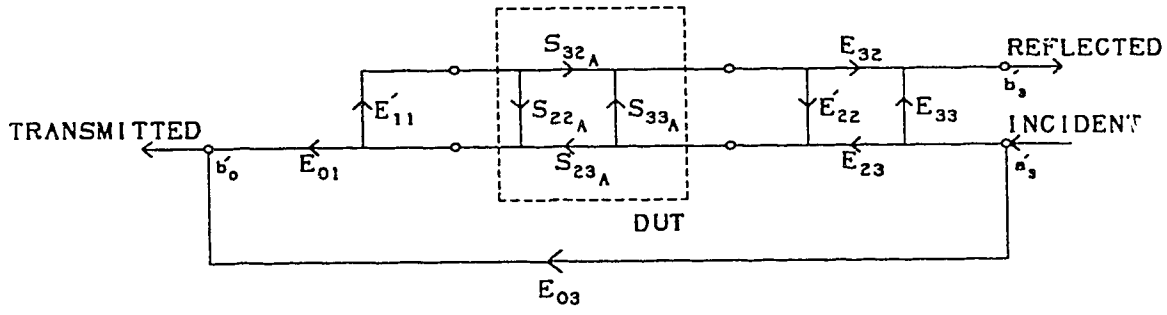

(b) Reverse measurement of S_{12_M} and S_{22_M}.

Figure 2.10: The two port, twelve error vector model.

2.3.4 Two Port, Twelve Error Vector Model

The twelve vector model is intended to overcome some of the limitations imposed by the simpler eight vector model. Figure 2.10 shows the signal flowgraphs. Two are used, one for forward and one for reverse measurements. Vectors E_{03} and E_{30} account for signal leakage between ports. E_{11} and E_{22} (forward) become E'_{11} and E'_{22} (reverse) to allow for differences in the reflection coefficient seen from the DUT when the S-parameter test set switches the port at which incident signal power is applied.

Three different sets of calibration standards were considered for the twelve vector model. The open-short-load-thruline (OSLT) method is a standard technique which has been used by others. An existing program ("SPARAMS") has sucessfully used this algorithm with a modified HP8410 system. The 3ST method described previously is also usable with the twelve vector model. An additional method, known as LRL (line-reflect-line) has also been derived; however, this method was unsuccessful as described herein, and should not be used in this form. It is included here for completeness and as a useful illustration of the sensitivity analysis method to be presented later.

2.3.4.1 The OSLT Method

The OSLT technique uses four standards. The open circuit is assumed to have a reflection coefficient 'A', rather than the value of 1 + j0. An estimate of the fringing capacitance is often used to obtain a numerical

value for 'A'. Both the short and load standards are modelled as being ideal. A sliding load can be used to improve the approximation of a perfect match. The thruline is assumed to have a transmission coefficient H. In the special case of a zero length line, the value of H becomes 1 + j0. S-parameters of the standards are therefore:

Standard # 1 $S_1 = \begin{bmatrix} A & 0 \\ 0 & A \end{bmatrix}$ open

Standard # 2 $S_2 = \begin{bmatrix} -1 & 0 \\ 0 & -1 \end{bmatrix}$ short

Standard # 3 $S_3 = \begin{bmatrix} 0 & 0 \\ 0 & 0 \end{bmatrix}$ load

Standard # 4 $S_4 = \begin{bmatrix} 0 & H \\ H & 0 \end{bmatrix}$ thruline

Using the flowchart of figure 2.10 and the S-parameters of the standards, the equations of measurement can be found using Mason's Rule. The twelve equations are shown below:

Equations of measurement for standard #1: (open)

$$M_{01} = E_{00} + \frac{E_{01}E_{10}A}{1 - E_{11}A} \qquad (2.47)$$

$$M'_{01} = E_{33} + \frac{E_{23}E_{32}A}{1 - E_{22}A} \qquad (2.4$$

Equations of measurement for standard #2: (short)

$$M_{02} = E_{00} - \frac{E_{01}E_{10}}{1 + E_{11}} \tag{2.49}$$

$$M'_{02} = E_{33} - \frac{E_{32}E_{23}}{1 + E_{22}} \tag{2.50}$$

Equations of measurement for standard #3: (load-50Ω)

$$M_{03} = E_{00} \tag{2.51}$$

$$M'_{03} = E_{33} \tag{2.52}$$

$$M_{33} = E_{30} \tag{2.53}$$

$$M'_{33} = E_{03} \tag{2.54}$$

Equations of measurement for standard #4: (thruline)

$$M_{04} = E_{00} + \frac{E_{01}E_{10}E'_{22}H^2}{1 - E_{11}E'_{22}H^2} \tag{2.55}$$

$$M'_{04} = E_{33} + \frac{E_{23}E_{32}E'_{11}H^2}{1 - E'_{11}E_{22}H^2} \tag{2.56}$$

$$M_{34} = E_{30} + \frac{E_{10}E_{32}H}{1 - E_{11}E'_{22}H^2} \tag{2.57}$$

$$M'_{34} = E_{03} + \frac{E_{01}E_{23}H}{1 - E'_{11}E_{22}H^2} \tag{2.58}$$

where, for the ith standard,

M_{0i} = reflection coefficient - forward direction

M'_{0i} = reflection coefficient - reverse direction

M_{3i} = transmission coefficient - forward direction

M'_{3i} = transmission coefficient - reverse direction

Four equations describe the measured S-parameters of the DUT, which can be obtained from the signal flowgraph of figure 2.10. These can be rearranged to yield an explicit solution of the actual DUT S-parameters in terms of the measurements and error vectors:

$$S_{11} = \frac{1}{d}\left\{ \frac{(S_{11m}-E_{00})}{E_{01}E_{10}}\left[1 + \frac{E_{22}(S_{22m}-E_{33})}{E_{23}E_{32}} \right] - \frac{E'_{22}(S_{21m}-E_{30})(S_{12m}-E_{03})}{E_{10}E_{32}\quad E_{01}E_{23}} \right\} \tag{2.59}$$

$$S_{12} = \frac{1}{d}\left[1+ \frac{(S_{11m}-E_{00})(E_{11}-E'_{11})}{E_{01}E_{10}}\right]\left[\frac{S_{12m}-E_{03}}{E_{01}E_{23}}\right] \tag{2.60}$$

$$S_{21} = \frac{1}{d}\left[1+ \frac{(S_{22m}-E_{33})(E_{22}-E'_{22})}{E_{23}E_{32}}\right]\left[\frac{S_{21m}-E_{30}}{E_{10}E_{32}}\right] \tag{2.61}$$

$$S_{22} = \frac{1}{d}\left\{ \frac{(S_{22m}-E_{33})}{E_{23}E_{32}}\left[1 + \frac{E_{11}(S_{11m}-E_{00})}{E_{01}E_{10}} \right] - \frac{E'_{11}(S_{21m}-E_{30})(S_{12m}-E_{03})}{E_{10}E_{32}\quad E_{01}E_{23}} \right\} \tag{2.62}$$

where

$$d = \left[1 + \frac{E_{11}(S_{11m}-E_{00})}{E_{01}E_{10}} \right]\left[1 + \frac{E_{22}(S_{22m}-E_{33})}{E_{23}E_{32}} \right] - \frac{E'_{11}E'_{22}(S_{21m}-E_{30})(S_{12m}-E_{03})}{E_{10}E_{32}\quad E_{01}E_{23}} \tag{2.63}$$

and the "m" subscript denotes measured quantities.

Details of the derivation of these formulas can be found in a thesis by Chau [2.10].

2.3.4.2 The 3ST Method

Three different offset shorts plus a thruline are used for the 3ST method. In fact, the "three shorts" can be any three unique reflection coefficients. One advantage of the technique is the elimination of the matched load as a standard. Disadvantages include frequency sensitivity and bandwidth limitations. Soares [2.1] states that the method does not yield good accuracy for the terms E_{00} and E_{33}.

Let the four standards be defined by the following S-parameters:

Standard #1 $$S_1 = \begin{bmatrix} A & 0 \\ 0 & D \end{bmatrix}$$ two reflections

Standard #2 $$S_2 = \begin{bmatrix} B & 0 \\ 0 & F \end{bmatrix}$$ two reflections

Standard #3 $$S_3 = \begin{bmatrix} C & 0 \\ 0 & G \end{bmatrix}$$ two reflections

Standard #4 $$S_4 = \begin{bmatrix} 0 & H \\ H & 0 \end{bmatrix}$$ thruline

The measured data equations are then given by:

Standard #1:

$$M_{01} = E_{00} + \frac{A\ E_{01} E_{10}}{1 - A\ E_{11}} \qquad (2.64)$$

$$M'_{01} = E_{33} + \frac{D\ E_{23}E_{32}}{1 - D\ E_{22}} \tag{2.65}$$

$$M_{31} = E_{30} \tag{2.66}$$

$$M'_{31} = E_{03} \tag{2.67}$$

Standard #2:

$$M_{02} = E_{00} + \frac{B\ E_{01}E_{10}}{1 - B\ E_{11}} \tag{2.68}$$

$$M'_{02} = E_{33} + \frac{F\ E_{23}E_{32}}{1 - F\ E_{22}} \tag{2.69}$$

$$M_{32} = E_{30} \tag{2.70}$$

$$M'_{32} = E_{03} \tag{2.71}$$

Standard #3:

$$M_{03} = E_{00} + \frac{C\ E_{01}E_{10}}{1 - C\ E_{11}} \tag{2.72}$$

$$M'_{03} = E_{33} + \frac{G\ E_{23}E_{32}}{1 - G\ E_{22}} \tag{2.73}$$

$$M_{33} = E_{30} \tag{2.74}$$

$$M'_{33} = E_{03} \tag{2.75}$$

Standard #4:

$$M_{04} = E_{00} + \frac{H^2 E_{01} E_{10} E'_{22}}{1 - H^2 E_{11} E'_{22}} \tag{2.76}$$

$$M'_{04} = E_{33} + \frac{H^2 E_{23} E_{32} E'_{11}}{1 - H^2 E'_{11} E_{22}} \tag{2.77}$$

$$M_{34} = E_{30} + \frac{H\ E_{10} E_{32}}{1 - H^2 E_{11} E'_{22}} \tag{2.78}$$

$$M'_{34} = E_{03} + \frac{H\ E_{01} E_{23}}{1 - H^2 E'_{11} E_{22}} \tag{2.79}$$

The measured data equations can be solved to give expressions for the error vectors. Values of E_{03} and E_{30} are overdetermined, and are estimated by averaging the three available values for each.

$$E_{30} = \frac{1}{3}\ (M_{31} + M_{32} + M_{33}) \tag{2.80}$$

$$E_{03} = \frac{1}{3}\ (M'_{31} + M'_{32} + M'_{33}) \tag{2.81}$$

$$E_{11} = \frac{(C-B)M_{01} + (A-C)M_{02} + (B-A)M_{03}}{A(C-B)M_{01} + B(A-C)M_{02} + C(B-A)M_{03}} \tag{2.82}$$

$$E_{01}E_{10} = \frac{(M_{01} - M_{02})(1 - AE_{11})(1 - BE_{11})}{(A - B)} \tag{2.83}$$

$$E_{00} = M_{02} - \frac{B(M_{01} - M_{02})(1 - AE_{11})}{(A - B)} \tag{2.84}$$

$$E_{22} = \frac{(G-F)M'_{01} + (D-G)M'_{02} + (F-D)M'_{03}}{D(G-F)M'_{01} + F(D-G)M'_{02} + G(F-D)M'_{03}} \tag{2.85}$$

$$E_{23}E_{32} = \frac{(M'_{01} - M'_{02})(1 - DE_{22})(1 - FE_{22})}{(D - F)} \tag{2.86}$$

$$E_{33} = M'_{02} - \frac{F(M'_{01} - M'_{02})(1 - DE_{22})}{(D - F)} \tag{2.87}$$

$$E'_{22} = \frac{(M_{04} - E_{00})}{H^2 (E_{01}E_{10} + (M_{04} - E_{00})E_{11})} \tag{2.88}$$

$$E_{10}E_{32} = (M_{34} - E_{30})\left(\frac{1}{H} - H E_{11}E'_{22}\right) \tag{2.89}$$

$$E'_{11} = \frac{(M'_{04} - E_{33})}{H^2 (E_{23}E_{32} + (M'_{04} - E_{33})E_{22})} \tag{2.90}$$

$$E_{01}E_{23} = (M'_{34} - E_{03})\left(\frac{1}{H} - H E'_{11}E_{22}\right) \tag{2.91}$$

The de-embedding equations are the same as those given for the OSLT method (2.59 through 2.63).

The LRL Method

The LRL method [2.11] requires only 3 standards: two thrulines of different electrical length and a two-port with reflections only. A special case of the LRL method is the thru-short-delay (TSD) calibration, which uses a zero length thruline for one of the two lines and two shorts for the reflection coefficients. The author attempted to use the

LRL method, as described here, without success. Reasons for the failure are discussed later.

The S-parameters of the three devices to be measured as calibration standards are assumed to be:

Standard #1 $\quad S_1 = \begin{bmatrix} 0 & A \\ A & 0 \end{bmatrix}$ line 1

Standard #2 $\quad S_2 = \begin{bmatrix} 0 & B \\ B & 0 \end{bmatrix}$ line 2

Standard #3 $\quad S_3 = \begin{bmatrix} C & 0 \\ 0 & D \end{bmatrix}$ two reflections

Solution for the measured values of the composite network can be obtained by applying Mason's rule [2.9] to the signal flowgraph of Figure 2.10. The following equations describe the measured values in terms of the unknown error vectors and the postulated standards. The notation used is consistent with the "SPARAMS" program used by the existing HP8410 VANA system.

Equations for measurement of standard #1:

$$M_{01} = E_{00} + \frac{A^2 E_{01} E_{10} E'_{22}}{1 - A^2 E_{11} E'_{22}} \tag{2.92}$$

$$M'_{01} = E_{33} + \frac{A^2 E_{23} E_{32} E'_{11}}{1 - A^2 E'_{11} E_{22}} \tag{2.93}$$

$$M_{31} = E_{30} + \frac{A\ E_{10}E_{32}}{1 - A^2E_{11}E_{22}'} \tag{2.94}$$

$$M_{31}' = E_{03} + \frac{A\ E_{01}E_{23}}{1 - A^2E_{11}'E_{22}} \tag{2.95}$$

Similarly, for standard #2:

$$M_{02} = E_{00} + \frac{B^2E_{01}E_{10}E_{22}'}{1 - B^2E_{11}E_{22}'} \tag{2.96}$$

$$M_{02}' = E_{33} + \frac{B^2E_{23}E_{32}E_{11}'}{1 - B^2E_{11}'E_{22}} \tag{2.97}$$

$$M_{32} = E_{30} + \frac{B\ E_{10}E_{32}}{1 - B^2E_{11}E_{22}'} \tag{2.98}$$

$$M_{32}' = E_{03} + \frac{B\ E_{01}E_{23}}{1 - B^2E_{11}'E_{22}} \tag{2.99}$$

Finally, standard #3 yields:

$$M_{03} = E_{00} + \frac{C\ E_{01}E_{10}}{1 - C\ E_{11}} \tag{2.100}$$

$$M_{03}' = E_{33} + \frac{D\ E_{23}E_{32}}{1 - D\ E_{22}} \tag{2.101}$$

$$M_{33} = E_{30} \tag{2.102}$$

$$M'_{33} = E_{03} \tag{2.103}$$

The preceding equations can be solved by back substitution and algebraic manipulation, yielding the following set of equations which describe the error vectors in terms of the known standards and associated measured values.

$$\text{Let} \quad k = \frac{1}{AB}\left[\frac{B\,M_{31} + A\,M_{32} - (A+B)\,M_{33}}{A\,M_{31} + B\,M_{32} - (A+B)\,M_{33}}\right] \tag{2.104}$$

$$\text{and} \quad k' = \frac{1}{AB}\left[\frac{B\,M'_{31} + A\,M'_{32} - (A+B)\,M'_{33}}{A\,M'_{31} + B\,M'_{32} - (A+B)\,M'_{33}}\right] \tag{2.105}$$

then

$$E_{03} = M'_{33} \tag{2.106}$$

$$E_{30} = M_{33} \tag{2.107}$$

$$E_{10}E_{32} = \frac{1}{A}(M_{31} - M_{32})(1 - A^2k) \tag{2.108}$$

$$E_{01}E_{23} = \frac{1}{A}(M'_{31} - M'_{32})(1 - A^2k') \tag{2.109}$$

$$E_{00} = M_{01} - \frac{A\,(M_{01} - M_{02})}{(A^2 - B^2)}(A - B^2k) \tag{2.110}$$

$$E_{33} = M'_{01} - \frac{A\,(M'_{01} - M'_{02})}{(A^2 - B^2)}(A - B^2k') \tag{2.111}$$

$$E'_{22} = \frac{C\,(M_{01} - E_{00})(1 - A^2k)}{A^2(M_{03} - E_{00})} + Ck \tag{2.112}$$

$$E_{11} = \frac{E'_{22}}{k} \tag{2.113}$$

$$E_{01}E_{10} = (M_{03} - E_{00})\left(\frac{1}{C} - E_{11}\right) \tag{2.114}$$

$$E'_{11} = \frac{D\,(M'_{01} - E_{33})(1 - A^2k')}{A^2(M'_{03} - E_{33})} + Dk' \tag{2.115}$$

$$E_{22} = \frac{E'_{11}}{k'} \tag{2.116}$$

$$E_{23}E_{32} = (M'_{03} - E_{33})\left(\frac{1}{D} - E_{22}\right) \tag{2.117}$$

The LRL method has been used successfully by others [2.11, 2.12], but the author's implementation failed due to what initially appeared to be very high sensitivity to error in the measurement of the standards. To obtain some information on the relative sensitivity of various calibration methods prior to investing resources in the construction of suitable cryogenic standards, the analysis of the following section was performed.

2.4 Sensitivity Analysis of Error Vector Models

2.4.1 Sensitivity Analysis and Results

The error models previously discussed are intended to permit accurate S-parameter measurements despite hardware limitations. Calibration data obtained using any measurement hardware system will, in general, be subject to

non-repeatable errors (due to imperfect switching or connections, for example) which the correction algorithm cannot remove. Some form of sensitivity analysis to determine the effects of these errors is desirable, but cannot be obtained easily by direct differentiation of the functions involved. Both the input and output variables of the correction algorithm are complex, and the method described here sucessfully addresses this difficulty. The author thanks Eric Valk [2.13], who had prepared the following sensivitity algorithm for his own purposes, for sharing his work. (Application of this method to investigate the VANA error correction is the author's work.)

Suppose the sensitivity of the following function is desired:

$$w=f(z) \qquad \text{where} \qquad z=a+jb \;\; ; \; a,b \text{ real} \qquad (2.118)$$
$$w=u+jv \;\; ; \; u,v \text{ real}$$

The derivatives of 2.118 in the vicinity of some arbitrary point z_o can be written:

$$\frac{\partial w}{\partial a} = \alpha + j\gamma \qquad \text{where} \qquad \alpha = \frac{\partial u}{\partial a} \qquad (2.119)$$
$$\gamma = \frac{\partial v}{\partial a}$$

$$\text{and} \quad \frac{\partial w}{\partial b} = \beta + j\varepsilon \qquad \text{where} \qquad \beta = \frac{\partial u}{\partial b} \qquad (2.120)$$
$$\varepsilon = \frac{\partial v}{\partial b}$$

To obtain a maximum value of sensitivity at z_0, let

$$Q = \frac{|\Delta w|}{|\Delta z|} \qquad \text{where} \qquad \Delta w = \Delta u + j\Delta v$$
$$\approx (\alpha\Delta a + \beta\Delta b) + j(\gamma\Delta a + \varepsilon\Delta b)$$
$$\Delta z = \Delta a + j\Delta b \qquad (2.121)$$

Then,

$$Q^2 = \frac{(\Delta u^2 + \Delta v^2)}{(\Delta a^2 + \Delta b^2)} \qquad (2.122)$$

which, after some algebraic manipulation, can be expressed as

$$Q^2 = \left[(\alpha^2 + \gamma^2)R^2 + 2(\alpha\beta + \gamma\varepsilon)R + (\beta^2 + \varepsilon^2)\right] (R^2 + 1)^{-1}$$

$$\text{where} \quad R = \frac{\Delta a}{\Delta b} \qquad (2.123)$$

R is related to the angle of Δz, the input perturbation vector, by the relation

$$\arg(\Delta z) = \tan^{-1}\left[\frac{\Delta b}{\Delta a}\right] = \tan^{-1}\left[\frac{1}{R}\right]. \qquad (2.124)$$

Equation 2.123 can therefore be differentiated with respect to R to find the angle of Δw which maximizes (or minimizes) the value of Q:

$$\frac{\partial(Q^2)}{\partial R} = 2\left[(\alpha\beta+\gamma\varepsilon) + (\alpha^2+ \gamma^2- \beta^2- \varepsilon^2)R - (\alpha\beta+\gamma\varepsilon)R^2\right] (R^2+1)^{-2} \qquad (2.125)$$

Equating 2.125 to zero gives the value of R, denoted R_o, at which these extrema occur:

$$0 = R_o^2 - 2PR_o - 1$$

$$\text{where} \quad P = \frac{1}{2}\left[\frac{\alpha^2+ \gamma^2- \beta^2- \varepsilon^2}{\alpha\beta + \gamma\varepsilon}\right] \qquad (2.126)$$

and therefore

$$R_o = P \pm \sqrt{P^2+ 1} \qquad (2.127)$$

Substituting 2.127 into 2.123 and solving for the

extrema of Q, similarly denoted Q_0, yields

$$Q_0^2 = (\alpha^2 + \gamma^2) + (\alpha\beta + \gamma\varepsilon)\left[P \pm \sqrt{P^2 + 1}\right]^{-1} \qquad (2.128)$$

It now remains only to select the proper sign in 2.128; the program written by the author uses the pragmatic approach of calculating both solutions and selecting the larger. The smaller solution represents a sensitivity minimum.

Special cases exist where equations 2.126 and 2.128 cannot be used. For example, if

$$\alpha = \beta = \gamma = \varepsilon = 0 \qquad (2.129)$$

then

$$Q_0 = 0. \qquad (2.130)$$

This is obvious since if the derivatives are all zero, then the value of w remains essentially unchanged for small perturbations.

If the condition

$$\alpha\beta + \gamma\varepsilon = 0 \qquad (2.131)$$

occurs, then P becomes either infinite or zero depending on the sign in equation 2.125. Substituting this expression for P into 2.127 and taking limits for both possibilities of P yields:

$$Q_0^2 = \alpha^2 + \gamma^2 \quad \text{if } P \to \infty \qquad (2.132)$$

and

$$Q_0^2 = \beta^2 + \varepsilon^2 \quad \text{if } P \to 0 \qquad (2.133)$$

or simply calculate both results and select the larger.

Normalized sensitivity is usually defined as [2.14]

$$S_n = \lim_{\Delta z \to 0} \frac{\Delta w / w}{\Delta z / z} \quad . \tag{2.134}$$

For purposes of evaluating S-parameter error correction methods, the following (not normalized) definition is used.

$$S = \lim_{\Delta z \to 0} \frac{\Delta w}{\Delta z} \tag{2.135}$$

This avoids difficulties in evaluating at the center of the Smith Chart where the value of z is zero. Using this method, the sensitivity of both the error vectors and the corrected measurements were determined for the various error models previously presented.

A disadvantage of this analysis is the assumption of a particular set of error vectors. The method does not provide sensitivity values for all possible values of the error vectors; indeed, to consider the entire set of all combinations of twelve complex vectors would result in a very large amount of data. The sensitivity data presented here is therefore based on a single set of error vectors, which are assumed to represent the hardware errors reasonably in the HP8410 system used. These values were obtained at 4 GHz from the working OSLT calibration system which has been used successfully for several years.

Having obtained a set of assumed values for the error vectors, the perfect standards required by each calibration method were then embedded, or corrupted, by the error vectors to obtain the hypothetical measured values which would be obtained from the imperfect measurement hardware. The sensitivity algorithm was then utilized to estimate the maximum sensitivity of each error vector to an error in each measurement of a calibration standard.

The error vectors are normally used to correct (through the de-embedding process) the corrupted measured values of a DUT. Perturbing the measured values of the standards and using the resulting error vectors to de-embed a DUT yields the sensitivity of a simulated measurement to errors in the standards measurement. The DUT to be de-embedded must be previously corrupted in the same manner as the standards. The sensitivities of both error vector and DUT measurements for various error correction schemes are presented in tabular form below.

This sensitivity analysis was initially performed for three two-port S-parameter calibration techniques : the OSLT, the 3ST, and the LRL method. An initial set of error vectors was obtained from a previous OSLT calibration of the HP8410 VANA system at 4.0 GHz:

$E_{00} = -0.02839808 + j0.009611275$

$E_{11} = 0.02637238 - j0.002081863$

$E_{22} = 0.04485809 - j0.01121445$

$E'_{11} = 0.03005592 - j0.002960020$

$E'_{22} = 0.04734705 - j0.02749767$

$E_{33} = -0.02234590 + j0.02750831$

$E_{03} = 0.0004214467 - j0.001047665$

$E_{30} = 0.0005761075 - j0.001212357$

$E_{01}E_{10} = 0.5873697 - j0.04349688$

$E_{01}E_{23} = 0.6317348 - j0.1666115$

$E_{10}E_{23} = 0.5500944 - j0.1878251$

$E_{23}E_{32} = 0.5112533 - j0.3893004$

Although unlikely to be the final error vectors required, the sensitivity results obtained were useful in comparing methods. Additionally, the S-parameters of seven standard two-ports were computed :

OPEN (both ports)

$$S_{O_A} = \begin{bmatrix} 1 & 0 \\ 0 & 1 \end{bmatrix}$$

LOAD (both ports)

$$S_{L_A} = \begin{bmatrix} 0 & 0 \\ 0 & 0 \end{bmatrix}$$

SHORT (at reference plane)

$$S_{S_A} = \begin{bmatrix} -1 & 0 \\ 0 & -1 \end{bmatrix}$$

SHORT #1 (120° offset)

$$S_{S1_A} = \begin{bmatrix} -1 \angle +120^\circ & 0 \\ 0 & -1 \angle +120^\circ \end{bmatrix}$$

SHORT #2 (-120° offset)

$$S_{S2_A} = \begin{bmatrix} -1 \angle -120^\circ & 0 \\ 0 & -1 \angle -120^\circ \end{bmatrix}$$

THRULINE (no delay)

$$S_{T_A} = \begin{bmatrix} 1 & 0 \\ 0 & 1 \end{bmatrix}$$

THRULINE (90° delay)

$$S_{T1_A} = \begin{bmatrix} 0 & 1 \angle -90^\circ \\ 1 \angle -90^\circ & 0 \end{bmatrix}$$

By using the error vectors, and the embedding equations, the measured (ie. corrupted) S-parameters of the loads were computed. The appropriate measured loads for each calibration were then used to simulate a calibration, and the error vectors were determined. Comparing these results with the original error vectors is a useful verification of the equations and computer program. Similarly, all seven "measured" standards were de-embedded and proper functioning of this algorithm confirmed.

Once proper operation of the various programs was established, the real and imaginary part of each measured standard was perturbed by a small quantity, the new values of the error vectors were determined, and finite difference approximations to α, β, γ and ε were computed. The sensitivity, Q, was then calculated using 2.128 through 2.133. The process was repeated to establish a matrix of sensitivities relating all the input and output variables. A graphical interpretation of the analysis is shown in Figure 2.11. These results were tabulated in Tables 2.1, 2.2 and 2.3 for the three calibration schemes.

Extending this method further, the measured loads can be de-embedded using the perturbed error vectors to estimate the sensitivity of de-embedded DUT values to errors in measurement of the standards. Tables 2.4 to 2.10 give the

results for all seven loads for the OSLT method. Similarly, Tables 2.11 to 2.17 and 2.18 to 2.24 present the results for the 3ST and the LRL method respectively.

Table 2.1 shows the sensitivity of the twelve error vectors to the measured data of the calibration standards using the OSLT method. Values range to a maximum of 1.7, with six of them exceeding unity. The large number of zeros in this and subsequent tables usually indicate measurements not used to determine the error vectors.

The results shown in Table 2.2 indicate a marginal improvement in calibration using the 3ST method over the OSLT technique. Maximum sensitivity remains at 1.7; however, only two values exceed unity.

The failure of the LRL method as implemented is clearly seen in Table 2.3. A total of eleven values are greater than ten, with a maximum sensitivity of 36.8. This extreme sensitivity accounts for the difficulties encountered when trying to use the equations previously presented.

Having estimated the effects of errors in measured standards on the error vectors, the effect on simulated DUT measurements is considered next. Tables 2.4 through 2.10 show the sensitivity of seven two-ports when using the OSLT method. Results vary from a maximum of 1.6 for an open circuit to 3.0 for shorts at $\pm 60^{\circ}$ and 3.4 for the 90° thruline. Good results can usually be expected with the OSLT method, since these figures represent the maximum sensitivities and typical values would likely be better.

Tables 2.11 through 2.17 contain the results of the

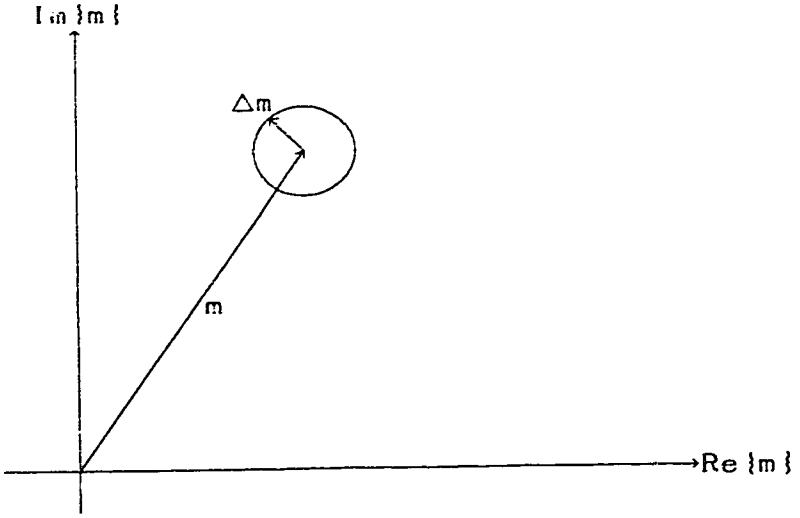

(a) Circular perturbation of measured standard M by ΔM.

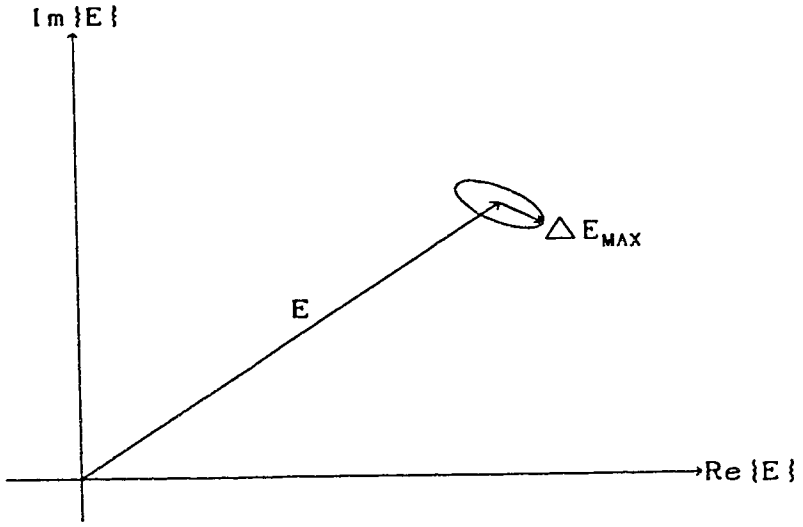

(b) Corresponding maximum error (ΔE_{MAX}) in vector E.

Figure 2.11: Graphical interpretation of the sensitivity analysis of error vector E to measured standard M.

same analysis using the 3ST technique. Sensitivities range from 0.6 for a matched termination to 1.8 for a direct short. This indicates that overall performance is slightly better than the OSLT method, although choosing between the

two may well be decided by availability of the required standards. Additionally, the results given are peculiar to the sample error vectors used, and can therefore not be considered as an indication of superiority for all conditions.

Finally, Tables 2.18 through 2.24 contain the sensitivities for the unsatisfactory LRL method. Both thrulines and the matched load achieved reasonable values of 1.7 or less. The worst results were values of 91.4 for an open, followed by 77.6 and 72.3 for offset shorts at -120° and $+120^{\circ}$ respectively. Obviously this method is unsuitable; these figures demonstrate both the cause of the difficulties encountered and the value of performing such a sensitivity analysis.

2.4.2 LRL Failure Analysis

The analysis of the previous section clearly indicated a problem with the LRL method as used, but an important question remained: why did the author's implementation fail so badly while others claim to have used it successfully? The answer consists of two parts: the author's algorithm failure, and the hardware requirements of the LRL method.

Using the twelve error vector model, a minimum of twelve unique S-parameter readings are required to obtain a solution for the error vectors. The LRL standards provide exactly twelve values, so in general the problem is neither over- nor under-determined. However, consider the two line standards. Measurements of S_{11} (or S_{22}) will yield

Table 2.1: Sensitivity of error vectors to errors in measured standards using the OSLT calibration method.

	E_{03}	E_{30}	$E_{32}E_{10}$	$E_{01}E_{23}$	E_{00}	E_{33}	E'_{22}	E'_{11}	E_{11}	E_{22}	$E_{01}E_{10}$	$E_{23}E_{32}$
M_{01}	0.0	0.0	0.0	0.0	0.0	0.0	0.0	0.0	0.8	0.0	0.5	0.0
M_{02}	0.0	0.0	0.0	0.0	0.0	0.0	0.0	0.0	0.9	0.0	0.5	0.0
M_{03}	0.0	0.0	0.1	0.0	1.0	0.0	1.7	0.0	1.7	0.0	0.1	0.0
M_{04}	0.0	0.0	0.0	0.0	0.0	0.0	1.7	0.0	0.0	0.0	0.0	0.0
M_{31}	0.0	0.0	0.0	0.0	0.0	0.0	0.0	0.0	0.0	0.0	0.0	0.0
M_{32}	0.0	0.0	0.0	0.0	0.0	0.0	0.0	0.0	0.0	0.0	0.0	0.0
M_{33}	0.0	1.0	1.0	0.0	0.0	0.0	0.0	0.0	0.0	0.0	0.0	0.0
M_{34}	0.0	0.0	1.0	0.0	0.0	0.0	0.0	0.0	0.0	0.0	0.0	0.0
M'_{01}	0.0	0.0	0.0	0.0	0.0	0.0	0.0	0.0	0.0	0.7	0.0	0.5
M'_{02}	0.0	0.0	0.0	0.0	0.0	0.0	0.0	0.0	0.0	0.8	0.0	0.5
M'_{03}	0.0	0.0	0.0	0.1	0.0	1.0	0.0	1.6	0.0	1.6	0.0	0.1
M'_{04}	0.0	0.0	0.0	0.0	0.0	0.0	0.0	1.6	0.0	0.0	0.0	0.0
M'_{31}	0.0	0.0	0.0	0.0	0.0	0.0	0.0	0.0	0.0	0.0	0.0	0.0
M'_{32}	0.0	0.0	0.0	0.0	0.0	0.0	0.0	0.0	0.0	0.0	0.0	0.0
M'_{33}	1.0	0.0	0.0	1.0	0.0	0.0	0.0	0.0	0.0	0.0	0.0	0.0
M'_{34}	0.0	0.0	0.0	1.0	0.0	0.0	0.0	0.0	0.0	0.0	0.0	0.0

Table 2.2: Sensitivity of error vectors to errors in measured standards using the 3ST calibration method.

	E_{03}	E_{30}	$E_{10}E_{32}$	$E_{01}E_{23}$	E_{00}	E_{33}	E'_{22}	E'_{11}	E_{11}	E_{22}	$E_{01}E_{10}$	$E_{23}E_{32}$
M_{01}	0.0	0.0	0.0	0.0	0.4	0.0	0.6	0.0	0.6	0.0	0.3	0.0
M_{02}	0.0	0.0	0.0	0.0	0.3	0.0	0.5	0.0	0.6	0.0	0.3	0.0
M_{03}	0.0	0.0	0.0	0.0	0.3	0.0	0.6	0.0	0.6	0.0	0.3	0.0
M_{04}	0.0	0.0	0.0	0.0	0.0	0.0	1.7	0.0	0.0	0.0	0.0	0.0
M_{31}	0.0	0.3	0.3	0.0	0.0	0.0	0.0	0.0	0.0	0.0	0.0	0.0
M_{32}	0.0	0.3	0.3	0.0	0.0	0.0	0.0	0.0	0.0	0.0	0.0	0.0
M_{33}	0.0	0.3	0.3	0.0	0.0	0.0	0.0	0.0	0.0	0.0	0.0	0.0
M_{34}	0.0	0.0	1.0	0.0	0.0	0.0	0.0	0.0	0.0	0.0	0.0	0.0
M'_{01}	0.0	0.0	0.0	0.0	0.0	0.4	0.0	0.6	0.0	0.5	0.0	0.3
M'_{02}	0.0	0.0	0.0	0.0	0.0	0.3	0.0	0.5	0.0	0.5	0.0	0.3
M'_{03}	0.0	0.0	0.0	0.0	0.0	0.3	0.0	0.5	0.0	0.5	0.0	0.3
M'_{04}	0.0	0.0	0.0	0.0	0.0	0.0	0.0	1.6	0.0	0.0	0.0	0.0
M'_{31}	0.3	0.0	0.0	0.3	0.0	0.0	0.0	0.0	0.0	0.0	0.0	0.0
M'_{32}	0.3	0.0	0.0	0.3	0.0	0.0	0.0	0.0	0.0	0.0	0.0	0.0
M'_{33}	0.3	0.0	0.0	0.3	0.0	0.0	0.0	0.0	0.0	0.0	0.0	0.0
M'_{34}	0.0	0.0	0.0	1.0	0.0	0.0	0.0	0.0	0.0	0.0	0.0	0.0

Table 2.3: Sensitivity of error vectors to errors in measured standards using the LRL calibration method.

	E_{03}	E_{30}	$E_{10}E_{32}$	$E_{01}E_{23}$	E_{00}	E_{33}	E'_{22}	E'_{11}	E_{11}	E_{22}	$E_{01}E_{10}$	$E_{23}E_{32}$
M_{01}	0.0	0.0	0.0	0.0	0.5	0.0	0.8	0.0	0.4	0.0	0.3	0.0
M_{02}	0.0	0.0	0.0	0.0	0.5	0.0	0.9	0.0	0.5	0.0	0.8	0.0
M_{03}	0.0	0.0	0.0	0.0	0.0	0.0	0.1	0.0	0.0	0.0	1.1	0.0
M_{31}	0.0	0.0	0.5	0.0	0.0	0.0	0.9	0.0	16.9	0.0	9.7	0.0
M_{32}	0.0	0.0	0.5	0.0	0.0	0.0	0.9	0.0	18.1	0.0	10.4	0.0
M_{33}	0.0	1.0	0.7	0.0	0.0	0.0	1.2	0.0	23.2	0.0	13.3	0.0
M'_{01}	0.0	0.0	0.0	0.0	0.0	0.5	0.0	0.8	0.0	1.3	0.0	0.3
M'_{02}	0.0	0.0	0.0	0.0	0.0	0.5	0.0	0.8	0.0	1.4	0.0	1.4
M'_{03}	0.0	0.0	0.0	0.0	0.0	0.0	0.0	0.1	0.0	0.1	0.0	1.1
M'_{31}	0.0	0.0	0.0	0.5	0.0	0.0	0.0	0.8	0.0	30.0	0.0	18.4
M'_{32}	0.0	0.0	0.0	0.5	0.0	0.0	0.0	0.8	0.0	31.6	0.0	19.4
M'_{33}	1.0	0.0	0.0	0.7	0.0	0.0	0.0	1.1	0.0	36.8	0.0	22.6

Table 2.4: Sensitivity of load to errors in measured standards using the OSLT calibration method.

	S_{11}	S_{12}	S_{21}	S_{22}
M_{01}	0.0	0.0	0.0	0.0
M_{02}	0.0	0.0	0.0	0.0
M_{03}	1.7	0.0	0.0	0.0
M_{04}	0.0	0.0	0.0	0.0
M_{31}	0.0	0.0	0.0	0.0
M_{32}	0.0	0.0	0.0	0.0
M_{33}	0.0	0.0	1.7	0.0
M_{34}	0.0	0.0	0.0	0.0
M'_{01}	0.0	0.0	0.0	0.0
M'_{02}	0.0	0.0	0.0	0.0
M'_{03}	0.0	0.0	0.0	1.6
M'_{04}	0.0	0.0	0.0	0.0
M'_{31}	0.0	0.0	0.0	0.0
M'_{32}	0.0	0.0	0.0	0.0
M'_{33}	0.0	1.5	0.0	0.0
M'_{34}	0.0	0.0	0.0	0.0

Table 2.5: Sensitivity of open to errors in measured standards using the OSLT calibration method.

	S_{11}	S_{12}	S_{21}	S_{22}
M_{01}	1.6	0.0	0.0	0.0
M_{02}	0.0	0.0	0.0	0.0
M_{03}	0.0	0.0	0.0	0.0
M_{04}	0.0	0.0	0.0	0.0
M_{31}	0.0	0.0	0.0	0.0
M_{32}	0.0	0.0	0.0	0.0
M_{33}	0.0	0.0	1.6	0.0
M_{34}	0.0	0.0	0.0	0.0
M'_{01}	0.0	0.0	0.0	1.4
M'_{02}	0.0	0.0	0.0	0.0
M'_{03}	0.0	0.0	0.0	0.0
M'_{04}	0.0	0.0	0.0	0.0
M'_{31}	0.0	0.0	0.0	0.0
M'_{32}	0.0	0.0	0.0	0.0
M'_{33}	0.0	1.4	0.0	0.0
M'_{34}	0.0	0.0	0.0	0.0

Table 2.6: Sensitivity of direct short to errors in measured standards using the OSLT calibration method.

	S_{11}	S_{12}	S_{21}	S_{22}
M_{01}	0.0	0.0	0.0	0.0
M_{02}	1.8	0.0	0.0	0.0
M_{03}	0.0	0.0	0.0	0.0
M_{04}	0.0	0.0	0.0	0.0
M_{31}	0.0	0.0	0.0	0.0
M_{32}	0.0	0.0	0.0	0.0
M_{33}	0.0	0.0	1.9	0.0
M_{34}	0.0	0.0	0.0	0.0
M'_{01}	0.0	0.0	0.0	0.0
M'_{02}	0.0	0.0	0.0	1.7
M'_{03}	0.0	0.0	0.0	0.0
M'_{04}	0.0	0.0	0.0	0.0
M'_{31}	0.0	0.0	0.0	0.0
M'_{32}	0.0	0.0	0.0	0.0
M'_{33}	0.0	1.7	0.0	0.0
M'_{34}	0.0	0.0	0.0	0.0

Table 2.7: Sensitivity of offset short ($\Gamma = 1.0 \angle 60^0$) to errors in measured standards using the OSLT calibration method.

	S_{11}	S_{12}	S_{21}	S_{22}
M_{01}	1.4	0.0	0.0	0.0
M_{02}	0.9	0.0	0.0	0.0
M_{03}	3.0	0.0	0.0	0.0
M_{04}	0.0	0.0	0.0	0.0
M_{31}	0.0	0.0	0.0	0.0
M_{32}	0.0	0.0	0.0	0.0
M_{33}	0.0	0.0	1.6	0.0
M_{34}	0.0	0.0	0.0	0.0
M'_{01}	0.0	0.0	0.0	1.2
M'_{02}	0.0	0.0	0.0	0.9
M'_{03}	0.0	0.0	0.0	2.7
M'_{04}	0.0	0.0	0.0	0.0
M'_{31}	0.0	0.0	0.0	0.0
M'_{32}	0.0	0.0	0.0	0.0
M'_{33}	0.0	1.6	0.0	0.0
M'_{34}	0.0	0.0	0.0	0.0

Table 2.8: Sensitivity of offset short ($\Gamma = 1.0 \angle -60^0$) to errors in measured standards using the OSLT calibration method.

	S_{11}	S_{12}	S_{21}	S_{22}
M_{01}	1.4	0.0	0.0	0.0
M_{02}	0.9	0.0	0.0	0.0
M_{03}	3.0	0.0	0.0	0.0
M_{04}	0.0	0.0	0.0	0.0
M_{31}	0.0	0.0	0.0	0.0
M_{32}	0.0	0.0	0.0	0.0
M_{33}	0.0	0.0	1.7	0.0
M_{34}	0.0	0.0	0.0	0.0
M'_{01}	0.0	0.0	0.0	1.2
M'_{02}	0.0	0.0	0.0	0.9
M'_{03}	0.0	0.0	0.0	2.7
M'_{04}	0.0	0.0	0.0	0.0
M'_{31}	0.0	0.0	0.0	0.0
M'_{32}	0.0	0.0	0.0	0.0
M'_{33}	0.0	1.5	0.0	0.0
M'_{34}	0.0	0.0	0.0	0.0

Table 2.9: Sensitivity of thruline to errors in measured standards using the OSLT calibration method.

	S_{11}	S_{12}	S_{21}	S_{22}
M_{01}	0.0	0.0	0.0	0.0
M_{02}	0.0	0.0	0.0	0.0
M_{03}	0.0	0.0	0.0	0.0
M_{04}	1.7	0.0	0.0	0.0
M_{31}	0.0	0.0	0.0	0.0
M_{32}	0.0	0.0	0.0	0.0
M_{33}	0.0	0.0	0.0	0.0
M_{34}	0.1	0.0	1.7	0.1
M'_{01}	0.0	0.0	0.0	0.0
M'_{02}	0.0	0.0	0.0	0.0
M'_{03}	0.0	0.0	0.0	0.0
M'_{04}	0.0	0.1	0.1	1.6
M'_{31}	0.0	0.0	0.0	0.0
M'_{32}	0.0	0.0	0.0	0.0
M'_{33}	0.0	0.0	0.0	0.0
M'_{34}	0.1	1.5	0.0	0.0

Table 2.10: Sensitivity of thruline (90^0 elec. length) to errors in measured standards using the OSLT calibration method.

	S_{11}	S_{12}	S_{21}	S_{22}
M_{01}	0.0	0.0	0.1	0.0
M_{02}	0.0	0.0	0.1	0.0
M_{03}	3.4	0.1	0.2	0.0
M_{04}	1.7	0.0	0.1	0.0
M_{31}	0.0	0.0	0.0	0.0
M_{32}	0.0	0.0	0.0	0.0
M_{33}	0.1	0.0	2.5	0.1
M_{34}	0.1	0.0	1.7	0.1
M'_{01}	0.0	0.0	0.0	0.0
M'_{02}	0.0	0.1	0.0	0.0
M'_{03}	0.0	0.1	0.2	3.1
M'_{04}	0.0	0.1	0.1	1.6
M'_{31}	0.0	0.0	0.0	0.0
M'_{32}	0.0	0.0	0.0	0.0
M'_{33}	0.1	2.2	0.0	0.1
M'_{34}	0.1	1.5	0.0	0.0

Table 2.11: Sensitivity of load to errors in measured standards using the 3ST calibration method.

	S_{11}	S_{12}	S_{21}	S_{22}
M_{01}	0.6	0.0	0.0	0.0
M_{02}	0.5	0.0	0.0	0.0
M_{03}	0.6	0.0	0.0	0.0
M_{04}	0.0	0.0	0.0	0.0
M_{31}	0.0	0.0	0.6	0.0
M_{32}	0.0	0.0	0.6	0.0
M_{33}	0.0	0.0	0.6	0.0
M_{34}	0.0	0.0	0.0	0.0
M'_{01}	0.0	0.0	0.0	0.6
M'_{02}	0.0	0.0	0.0	0.5
M'_{03}	0.0	0.0	0.0	0.5
M'_{04}	0.0	0.0	0.0	0.0
M'_{31}	0.0	0.5	0.0	0.0
M'_{32}	0.0	0.5	0.0	0.0
M'_{33}	0.0	0.5	0.0	0.0
M'_{34}	0.0	0.0	0.0	0.0

Table 2.12: Sensitivity of open to errors in measured standards using the 3ST calibration method.

	S_{11}	S_{12}	S_{21}	S_{22}
M_{01}	0.6	0.0	0.0	0.0
M_{02}	1.1	0.0	0.0	0.0
M_{03}	1.1	0.0	0.0	0.0
M_{04}	0.0	0.0	0.0	0.0
M_{31}	0.0	0.0	0.5	0.0
M_{32}	0.0	0.0	0.5	0.0
M_{33}	0.0	0.0	0.5	0.0
M_{34}	0.0	0.0	0.0	0.0
M'_{01}	0.0	0.0	0.0	0.6
M'_{02}	0.0	0.0	0.0	1.0
M'_{03}	0.0	0.0	0.0	1.0
M'_{04}	0.0	0.0	0.0	0.0
M'_{31}	0.0	0.5	0.0	0.0
M'_{32}	0.0	0.5	0.0	0.0
M'_{33}	0.0	0.5	0.0	0.0
M'_{34}	0.0	0.0	0.0	0.0

Table 2.13: Sensitivity of direct short to errors in measured standards using the 3ST calibration method.

	S_{11}	S_{12}	S_{21}	S_{22}
M_{01}	1.8	0.0	0.0	0.0
M_{02}	0.0	0.0	0.0	0.0
M_{03}	0.0	0.0	0.0	0.0
M_{04}	0.0	0.0	0.0	0.0
M_{31}	0.0	0.0	0.6	0.0
M_{32}	0.0	0.0	0.6	0.0
M_{33}	0.0	0.0	0.6	0.0
M_{34}	0.0	0.0	0.0	0.0
M'_{01}	0.0	0.0	0.0	1.7
M'_{02}	0.0	0.0	0.0	0.0
M'_{03}	0.0	0.0	0.0	0.0
M'_{04}	0.0	0.0	0.0	0.0
M'_{31}	0.0	0.6	0.0	0.0
M'_{32}	0.0	0.6	0.0	0.0
M'_{33}	0.0	0.6	0.0	0.0
M'_{34}	0.0	0.0	0.0	0.0

Table 2.14: Sensitivity of offset short ($\Gamma = 1.0 \angle 60^0$) to errors in measured standards using the 3ST calibration method.

	S_{11}	S_{12}	S_{21}	S_{22}
M_{01}	0.0	0.0	0.0	0.0
M_{02}	1.6	0.0	0.0	0.0
M_{03}	0.0	0.0	0.0	0.0
M_{04}	0.0	0.0	0.0	0.0
M_{31}	0.0	0.0	0.5	0.0
M_{32}	0.0	0.0	0.5	0.0
M_{33}	0.0	0.0	0.5	0.0
M_{34}	0.0	0.0	0.0	0.0
M'_{01}	0.0	0.0	0.0	0.0
M'_{02}	0.0	0.0	0.0	1.5
M'_{03}	0.0	0.0	0.0	0.0
M'_{04}	0.0	0.0	0.0	0.0
M'_{31}	0.0	0.5	0.0	0.0
M'_{32}	0.0	0.5	0.0	0.0
M'_{33}	0.0	0.5	0.0	0.0
M'_{34}	0.0	0.0	0.0	0.0

Table 2.15: Sensitivity of offset short ($\Gamma = 1.0 \angle -60^0$) to errors in measured standards using the 3ST calibration method.

	S_{11}	S_{12}	S_{21}	S_{22}
M_{01}	0.0	0.0	0.0	0.0
M_{02}	0.0	0.0	0.0	0.0
M_{03}	1.7	0.0	0.0	0.0
M_{04}	0.0	0.0	0.0	0.0
M_{31}	0.0	0.0	0.6	0.0
M_{32}	0.0	0.0	0.6	0.0
M_{33}	0.0	0.0	0.6	0.0
M_{34}	0.0	0.0	0.0	0.0
M'_{01}	0.0	0.0	0.0	0.0
M'_{02}	0.0	0.0	0.0	0.0
M'_{03}	0.0	0.0	0.0	1.5
M'_{04}	0.0	0.0	0.0	0.0
M'_{31}	0.0	0.5	0.0	0.0
M'_{32}	0.0	0.5	0.0	0.0
M'_{33}	0.0	0.5	0.0	0.0
M'_{34}	0.0	0.0	0.0	0.0

Table 2.16: Sensitivity of thruline to errors in measured standards using the 3ST calibration method.

	S_{11}	S_{12}	S_{21}	S_{22}
M_{01}	0.0	0.0	0.0	0.0
M_{02}	0.0	0.0	0.0	0.0
M_{03}	0.0	0.0	0.0	0.0
M_{04}	1.7	0.0	0.0	0.0
M_{31}	0.0	0.0	0.0	0.0
M_{32}	0.0	0.0	0.0	0.0
M_{33}	0.0	0.0	0.0	0.0
M_{34}	0.1	0.0	1.7	0.1
M'_{01}	0.0	0.0	0.0	0.0
M'_{02}	0.0	0.0	0.0	0.0
M'_{03}	0.0	0.0	0.0	0.0
M'_{04}	0.0	0.1	0.1	1.6
M'_{31}	0.0	0.0	0.0	0.0
M'_{32}	0.0	0.0	0.0	0.0
M'_{33}	0.0	0.0	0.0	0.0
M'_{34}	0.1	1.5	0.0	0.0

Table 2.17: Sensitivity of thruline (90^0 elec. length) to errors in measured standards using the 3ST calibration method.

	S_{11}	S_{12}	S_{21}	S_{22}
M_{01}	1.2	0.0	0.1	0.0
M_{02}	1.1	0.0	0.1	0.0
M_{03}	1.1	0.0	0.1	0.0
M_{04}	1.7	0.0	0.1	0.0
M_{31}	0.0	0.0	0.8	0.0
M_{32}	0.0	0.0	0.8	0.0
M_{33}	0.0	0.0	0.8	0.0
M_{34}	0.1	0.0	1.7	0.1
M'_{01}	0.0	0.0	0.1	1.1
M'_{02}	0.0	0.0	0.1	1.0
M'_{03}	0.0	0.0	0.1	1.0
M'_{04}	0.0	0.1	0.1	1.6
M'_{31}	0.0	0.7	0.0	0.0
M'_{32}	0.0	0.7	0.0	0.0
M'_{33}	0.0	0.7	0.0	0.0
M'_{34}	0.1	1.5	0.0	0.0

Table 2.18: Sensitivity of load to errors in measured standards using the LRL calibration method.

	S_{11}	S_{12}	S_{21}	S_{22}
M_{01}	0.8	0.0	0.0	0.0
M_{02}	0.9	0.0	0.0	0.0
M_{03}	0.0	0.0	0.0	0.0
M_{31}	0.0	0.0	0.0	0.0
M_{32}	0.0	0.0	0.0	0.0
M_{33}	0.1	0.0	1.7	0.0
M'_{01}	0.0	0.0	0.0	0.8
M'_{02}	0.0	0.0	0.0	0.8
M'_{03}	0.0	0.0	0.0	0.0
M'_{31}	0.0	0.0	0.0	0.0
M'_{32}	0.0	0.0	0.0	0.0
M'_{33}	0.0	1.5	0.0	0.0

Table 2.19: Sensitivity of open to errors in measured standards using the LRL calibration method.

	S_{11}	S_{12}	S_{21}	S_{22}
M_{01}	1.0	0.0	0.0	0.0
M_{02}	2.5	0.0	0.0	0.0
M_{03}	1.8	0.0	0.0	0.0
M_{31}	33.3	0.0	0.0	0.0
M_{32}	31.3	0.0	0.0	0.0
M_{33}	50.6	0.0	1.8	0.0
M'_{01}	0.0	0.0	0.0	1.2
M'_{02}	0.0	0.0	0.0	4.1
M'_{03}	0.0	0.0	0.0	1.7
M'_{31}	0.0	0.0	0.0	53.0
M'_{32}	0.0	0.0	0.0	50.5
M'_{33}	0.0	1.8	0.0	91.4

Table 2.20: Sensitivity of direct short to errors in measured standards using the LRL calibration method.

	S_{11}	S_{12}	S_{21}	S_{22}
M_{01}	0.0	0.0	0.0	0.0
M_{02}	0.0	0.0	0.0	0.0
M_{03}	1.8	0.0	0.0	0.0
M_{31}	0.0	0.0	0.0	0.0
M_{32}	0.0	0.0	0.0	0.0
M_{33}	0.0	0.0	1.9	0.0
M'_{01}	0.0	0.0	0.0	0.0
M'_{02}	0.0	0.0	0.0	0.0
M'_{03}	0.0	0.0	0.0	1.7
M'_{31}	0.0	0.0	0.0	0.0
M'_{32}	0.0	0.0	0.0	0.0
M'_{33}	0.0	1.6	0.0	0.0

Table 2.21: Sensitivity of offset short ($\Gamma = 1.0 \angle 60^0$) to errors in measured standards using the LRL calibration method.

	S_{11}	S_{12}	S_{21}	S_{22}
M_{01}	1.6	0.0	0.0	0.0
M_{02}	1.7	0.0	0.0	0.0
M_{03}	1.8	0.0	0.0	0.0
M_{31}	30.2	0.0	0.0	0.0
M_{32}	28.2	0.0	0.0	0.0
M_{33}	40.6	0.0	1.7	0.0
M'_{01}	0.0	0.0	0.0	1.7
M'_{02}	0.0	0.0	0.0	3.2
M'_{03}	0.0	0.0	0.0	1.7
M'_{31}	0.0	0.0	0.0	50.6
M'_{32}	0.0	0.0	0.0	44.3
M'_{33}	0.0	1.7	0.0	72.3

Table 2.22: Sensitivity of offset short ($\Gamma = 1.0 \angle -60^0$) to errors in measured standards using the LRL calibration method.

	S_{11}	S_{12}	S_{21}	S_{22}
M_{01}	1.0	0.0	0.0	0.0
M_{02}	2.1	0.0	0.0	0.0
M_{03}	1.8	0.0	0.0	0.0
M_{31}	27.3	0.0	0.0	0.0
M_{32}	27.8	0.0	0.0	0.0
M_{33}	44.6	0.0	2.0	0.0
M'_{01}	0.0	0.0	0.0	2.3
M'_{02}	0.0	0.0	0.0	3.1
M'_{03}	0.0	0.0	0.0	1.7
M'_{31}	0.0	0.0	0.0	43.2
M'_{32}	0.0	0.0	0.0	47.6
M'_{33}	0.0	1.9	0.0	77.6

Table 2.23: Sensitivity of thruline to errors in measured standards using the LRL calibration method.

	S_{11}	S_{12}	S_{21}	S_{22}
M_{01}	1.7	0.0	0.0	0.0
M_{02}	0.0	0.0	0.0	0.0
M_{03}	0.0	0.0	0.0	0.0
M_{31}	0.1	0.0	1.7	0.1
M_{32}	0.0	0.0	0.0	0.0
M_{33}	0.0	0.0	0.0	0.0
M'_{01}	0.0	0.1	0.1	1.6
M'_{02}	0.0	0.0	0.0	0.0
M'_{03}	0.0	0.0	0.0	0.0
M'_{31}	0.1	1.6	0.0	0.0
M'_{32}	0.0	0.0	0.0	0.0
M'_{33}	0.0	0.1	0.1	0.0

Table 2.24: Sensitivity of thruline (90^{o} elec. length) to errors in measured standards using the LRL calibration method.

	S_{11}	S_{12}	S_{21}	S_{22}
M_{01}	0.0	0.0	0.0	0.0
M_{02}	1.7	0.0	0.0	0.0
M_{03}	0.0	0.0	0.0	0.0
M_{31}	0.0	0.0	0.0	0.0
M_{32}	0.1	0.0	1.7	0.1
M_{33}	0.0	0.0	0.0	0.0
M'_{01}	0.0	0.0	0.0	0.0
M'_{02}	0.0	0.1	0.1	1.6
M'_{03}	0.0	0.0	0.0	0.0
M'_{31}	0.0	0.0	0.0	0.0
M'_{32}	0.1	1.6	0.0	0.0
M'_{33}	0.0	0.1	0.1	0.0

different i[illegible]ion about the error vectors because the phase shift difference of the two lines causes error vectors on different sides of the line to combine differently.

Consider the special case where the S-parameter test set hardware presents an exact Z_o load to the DUT. Now the values of S_{11} (or S_{22}) for the two lines will be identical due to the perfect termination, assuming also perfect lines and connectors. With only ten unique values, the solution is now under-determined, and the LRL algorithm as presented could obviously not solve for the twelve error vectors. Although it is unlikely that the measured values would be exactly identical, it is reasonable to expect very high sensitivity in the vicinity of a singular solution.

Successful users of the LRL method use a hardware system which supplies the additional information needed to overcome this problem. The HP8510 system provides the extra data by using four directional couplers, while the HP8410 uses only two. In fact, Hewlett-Packard uses an eight error vector model for both forward and reverse directions, for a total of sixteen error vectors using the thru-short-delay (TSD) method. The TSD method is a special case of the LRL method, where one of the two thrulines is of zero length.

In conclusion, the twelve error vector LRL method seems unsuitable for the hardware system used for this thesis, and further attempts to use it as originally derived were abandoned. However, the sensitivity analysis used above is useful both as a general technique, and specifically to quantify the expected performance of a calibation. Any user

can estimate S-parameter sensitivity for a particular experiment simply by supplying the obtained error vectors and the measured DUT S-parameters to the algorithms, as explained.

2.5 Cryogenic Measurement Considerations

Calibration inside a cryostat necessitates the fabrication of standard two-port networks whose S-parameters can be determined from physical considerations, and which will withstand both thermal cycling and low temperatures. The author's previous experience indicates that commercial resistive devices (ie. resistors and attenuators) often do not survive cryogenic operation. Furthermore, it is difficult to be certain that the resistivity at microwave frequencies is relatively temperature independent. For reasons to be explained in later chapters, the standards were built in stripline configurations. A cryogenic matched termination in stripline, while desirable from a calibration standpoint, was abandoned as being impractical to fabricate with the confidence of performance required of a calibration standard.

Open circuits and thrulines were eventually selected as standards because of the ease of precise manufacture and confidence in the predictability of the device characteristics. Care was taken to ensure that the fixtures were as nearly identical as possible, since the calibration algorithm cannot correct for differences in connector transitions and parasitics among the various fixtures.

Initially, the LRL method had been considered as a

candidate for a single tier calibration of the entire system. Only three standards plus the DUT would be required, and these could thus be switched easily by a "binary tree" configuration of relays in the cryostat. Even following the initial failure of the LRL method, some consideration was given to the idea of using LRL with a reduced eight error vector model.

Eventually, the concept of a second tier LRL calibration was also abandoned in view of the following considerations:

1. Calibrating with all apparatus in the final assembled state is preferred to reduce reconnecting as a source of random error. It would be difficult to fit all the noise measurement apparatus, calibration standards and switching relays into the cryostat at the same time.
2. One of the two lines must be longer than the other. Accommodating this requirement, either by having one oversized calibration fixture or by "folding" the line inside the fixture is awkward. The latter remedy also raised concerns regarding the effect of the "folds" on the calibration procedure - the two lines should be identical in parasitics. Even if, say, mitered corners were used, the distance between some of the corners would likely be different in the two standards, and the effects of parasitics would not combine in the same manner.

The 3ST method was finally selected, despite its requiring four cryostat runs to obtain the calibration data. Error

vectors were calculated by a FORTRAN program, "ERRVECT", written by the author. This software is available upon request from the LNA Group, Department of Electrical Engineering, University of Alberta.

Chapter 3

Noise Parameter Measurement

3.1 Noise Parameter Representation

The concept of four noise parameters being sufficient to describe the noise behaviour of a two-port was introduced in chapter 1. Over the years a large number of parameter sets have been introduced, resulting in a variety of notations with varying degrees of consistency. For example, in a recent tutorial paper, Meer [3.1] provides a table of noise figure notations which cross-reference his paper and 34 others. This thesis does not attempt to present the numerous variations, only those utilized in this research. However, a number of noise parameter sets (and associated conversion equations) are needed since the analysis undertaken may definitely favour a particular representation. This is similar to the selection of Y, Z, S, or T parameters for network calculations to simplify analysis. Additionally, certain parameter sets exhibit fundamental limits on some variables; this constitutes a useful check that the measured values represent at least a physically possible device. Failure to meet such criteria is an indication of measurement or calculation error.

Voltage and current source representations have been discussed previously. Conversion equations between a model with two voltage sources (Figure 1.1(c)) and a voltage plus current model (Figure 1.1(d)) are given in appendix I(A).

The complex correlation coefficient, α, must satisfy the relation

$$|\alpha| \leq 1. \qquad (3.1)$$

Use of voltage and/or current sources permits easy use of circuit theory for computing the effects of network configurations. This will be expanded upon in the section on network effects.

Other noise parameter equations exist which present the noise figure as a function of four quantities describing the attributes of a quasi-paraboloid (Figure 3.1). The minimum of this function is usually denoted F_{min} (or F_{opt}) and is

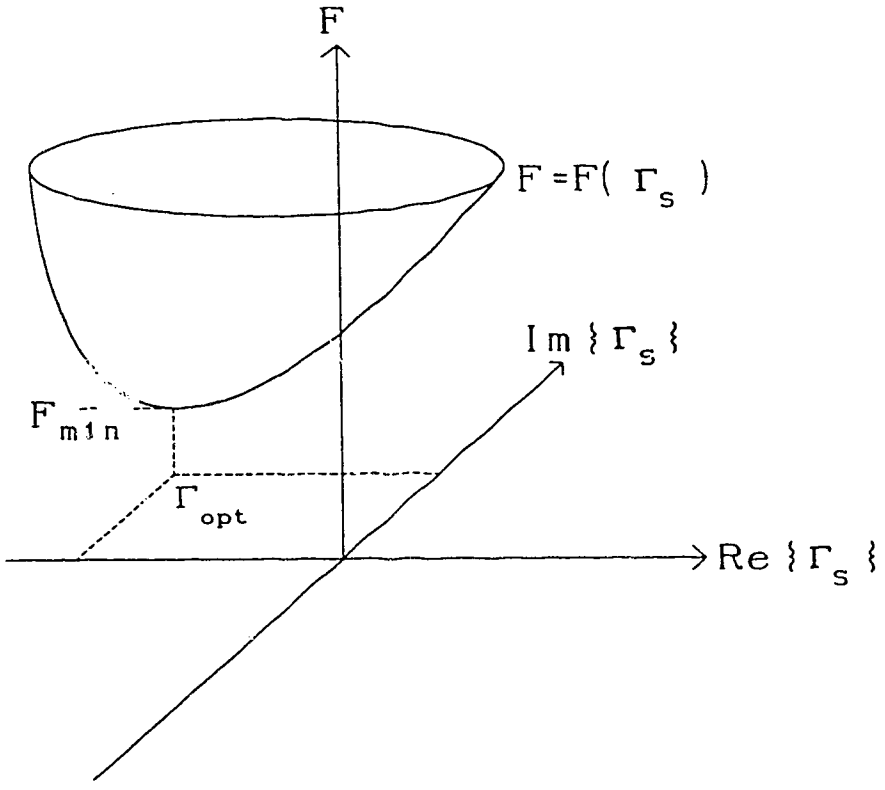

Figure 3.1: Graphical representation of noise figure F as a function of source reflection coefficient.

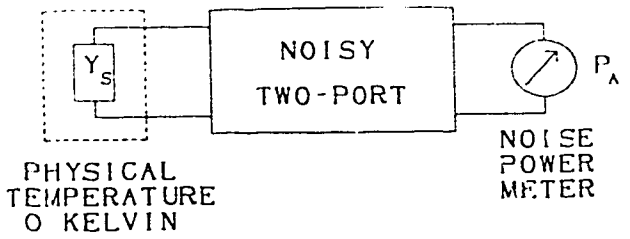

(a) Noisy two-port with noiseless (0 Kelvin) source admittance Y_s.

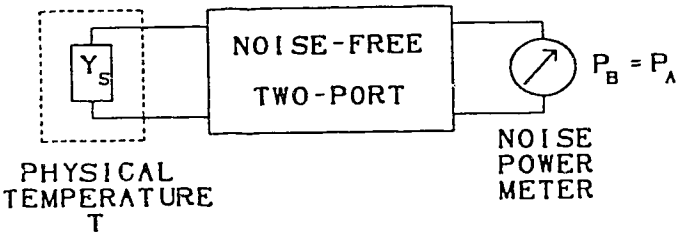

(b) Noise-free two-port with source admittance Y_s at physical temperature T.

Figure 3.2: Physical interpretation of two-port noise temperature.

the minimum noise figure obtainable by tuning the input impedance connected to the noisy two-port under consideration. A complex variable (eg. Y_{opt}, Γ_{opt}) denotes the source conditions for realizing the noise figure minimum. One additional term (eg. r_n, R_n, N) is the "slope factor" quantifying how rapidly the noise figure increases as the tuning departs from the optimum match. An example of this type of equation is

$$F = F_{min} + \frac{R_n}{G_s}\left[(G_s-G_{opt})^2 + (B_s-B_{opt})^2\right] \qquad (3.2)$$

as published by the IRE noise subcommitee in 1960 [3.2]. Some authors (eg. [3.3], [3.4]) abbreviate the equation to the form

$$F = F_{opt} + \frac{R_n}{G_s} \left| Y_s - Y_{opt} \right|^2 . \qquad (3.3)$$

Of particular interest is an expression (3.4) from a paper by Lange [3.3], and used by Pospieszalski [3.5] in the form

$$T = T_{min} + \frac{4NT_0 \left|\Gamma_{opt} - \Gamma_s\right|^2}{\left(1-|\Gamma_s|^2\right)\left(1-|\Gamma_{opt}|^2\right)} , \qquad (3.4)$$

where T is the noise temperature of the two-port,

Γ_s is the source reflection coefficient,

Γ_{opt} is the optimum value of Γ_s,

T_{min} is the minimum value of T obtained at the condition $\Gamma_s = \Gamma_{opt}$.

For any physical two-port, the inequality

$$T_{min} \leq 4NT_0 \qquad (3.5)$$

must be satisfied. Equation 3.4 is expressed as noise temperature, rather than noise figure; the relationship between these quantities is given by

$$T = T_0(F-1), \qquad (3.6)$$

where T_0 is the reference temperature (290K).

Unlike noise figure, the noise temperature is not defined

with respect to any particular reference temperature.

3.2 Noise Sources and the Noise-Temperature Diagram

Figure 3.2 illustrates a physical interpretation of the noise temperature of a two-port. In diagram 3.2(a) the source admittance temperature has been fictitiously lowered to absolute zero, and so generates no noise. Under these conditions, the power meter indicates some value corresponding to the noise power originating from the two-port and possibly from the power meter itself. In Figure 3.2(b), the same two-port is now assumed to be noise free and connected to the same source admittance, now assumed to be at physical temperature T. Under the conditions where the power meter reads the same as before, the value of T is referred to as the noise temperature of the two-port. Any noise contributed by the power meter is assumed constant, and therefore does not affect the value of T obtained by this experiment.

The foregoing interpretation of noise temperature leads directly to the noise-temperature (N-T) diagram, which will be introduced below. Frequently a passive noise source of known physical temperature is not used; active noise sources calibrated in terms of temperature equivalent are more convenient.

Noise sources (NS) are usually characterized by their noise temperature. This quantity refers to the physical temperature of a purely thermal noise source. Noise

generators containing active devices are defined as having a noise temperature equal to the fictitious physical temperature of a passive device of the same available noise power at the frequency of calibration. Furthermore, the noise temperature is a property of the noise source only, and is not dependent on any characteristics of the load to which it may be connected. The noise power available from any source is therefore given by

$$P_{AVS} = kT_{NS}B \ , \qquad (3.7)$$

where k is Boltzmann's constant

and B is the system bandwidth.

Active noise sources usually have two states, ON and OFF. Only the ON state is calibrated because, in the OFF state, the source is passive and its noise temperature is assumed to be the same as the ambient temperature. Two states are required; Gupta [3.6] proved the impossibility of measuring noise parameters with an output power meter if only a single noise temperature is available.

Noise measurements at radio and microwave frequencies usually employ some type of receiver (RX) to amplify, convert to some fixed intermediate frequency (IF), and detect the noise power of interest. Figure 3.3 shows a minimal system composed of a noise source connected to a power measuring receiver. The vertical line between the boxes denotes a reference plane for reflection coefficient measurements.

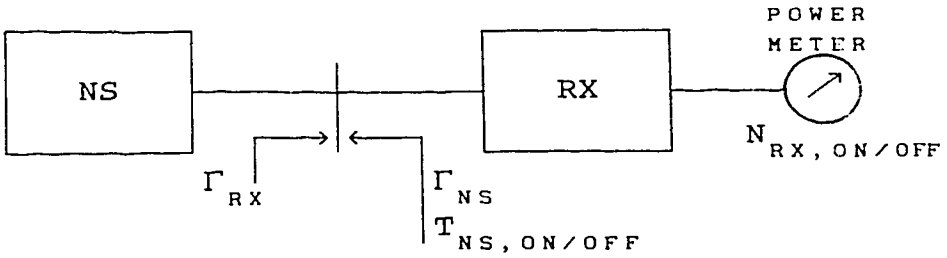

Figure 3.3: Apparatus for measurement of RX noise temperature.

The noise-temperature (N-T) diagram [3.7] is a graphical representation of the relationship between NS temperature and received noise power, using apparatus as shown in Figure 3.3. In the N-T diagram of Figure 3.4, N is the noise power indicated by the receiver and T_{NS} is the equivalent temperature of the noise source. The indicated power increases linearly with the noise source temperature, and if extrapolated to the case where $T_{NS} = 0$, the only noise produced is that of the receiver itself, N_o, since P_{AVS} of the source is zero. This provides an easy means of deducing the RX system noise temperature. This scheme can be used for the measurement of radiometer noise temperature. For such applications the NS is often some lossy material maintained at known physical temperatures T_1 and T_2. The noise power is coupled to the receiver by a low loss feed.

The equation represented by Figure 3.4 is given by

$$N = kT_{NS}BG_{RX} + N_o \quad , \tag{3.8}$$

where N is the noise power indicated by the RX,

T_{NS} is the noise temperature of the NS,

G_{RX} is the gain of the RX, here defined as

the ratio of the indicated noise power to the noise power absorbed by the RX, excluding any noise generated by the RX itself.

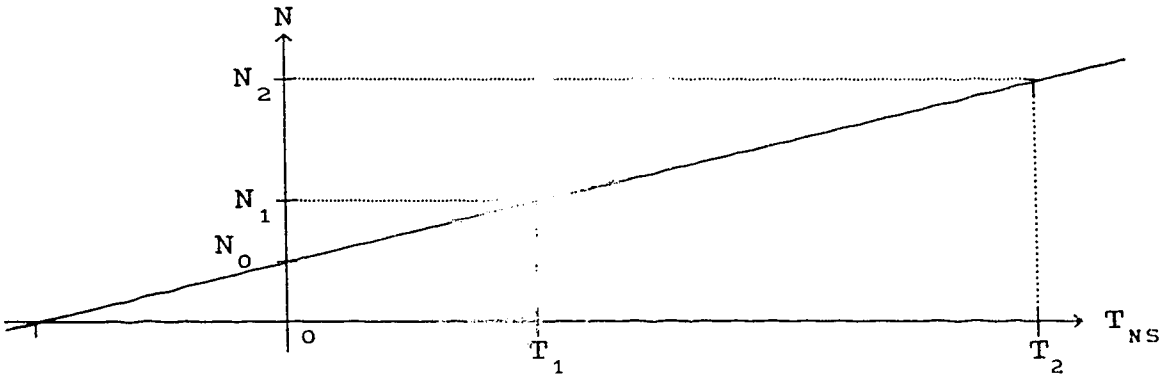

Figure 3.4: Noise-temperature diagram for the apparatus of Figure 3.3.

There are a few caveats to be observed when using N-T diagrams. The salient points are listed below:

1. System gain must not vary with T_{NS}. Since matching affects system gain, changes in source reflection coefficient between states must be prevented or corrected for.
2. Noise power transfer must be accounted for. The effects of mismatches must be calculated where necessary.
3. The value of receiver noise N_0 refers to the entire receiver system following the variable temperature noise source.
4. The receiver noise temperature is a function of the source reflection coefficient. The value of N_0

obtained is valid only for the value of Γ_{NS} used in the measurement.

The N-T diagram leads to an easy derivation of the Y-factor [3.7] technique for measurement of two-port noise figure and gain.

3.3 The Y-factor Method

The classic Y-factor method uses a receiver to measure the noise power in a given bandwidth. Usually this instrument will consist of a heterodyne receiver, with some fixed IF filter which determines the system bandwidth and bandpass shape. The noise power, N_{RX}, indicated by the receiver is then given by

$$N_{RX} = \int_{f=0}^{f=\infty} k\, T_{NS}(f)\, G_{RX}(f)\, df + N_{SYS}\ , \qquad (3.9)$$

where T_{NS} and G_{RX} are in general functions of frequency.

N_{RX} is therefore a function of both the noise power spectrum and the receiver bandpass characteristic. The value of T_{NS} is normally assumed constant over the measurement bandwidth. Rather than attempting to determine the effects of the function G(f), the Y-factor method uses a comparison measurement to circumvent the problem.

Measurements must be obtained with two equipment configurations to obtain a Y-factor measurement of the noise temperature of the DUT. The first step is often referred to

as a "calibration" step since it characterizes the test apparatus. Figure 3.3 again illustrates the connection of the noise source and receiver. Values of N_{RX} are obtained representing the total noise power ($N_{RX,OFF}$, $N_{RX,ON}$) for two noise source temperatures, $T_{NS,OFF}$ ("cold") and $T_{NS,ON}$ ("hot").

The receiver system noise contribution is assumed to be a constant value N_{SYS}, independent of the noise source temperature. The receiver gain bandwidth product determines the slope of the line, hereafter denoted ζ. Figure 3.5 illustrates the measurement graphically; N_{SYS} corresponds to the fictitious case where the noise source is at absolute zero temperature, and therefore contributes no noise. The horizontal axis intercept of the line occurs at a value of $-T_{SYS}$, which is the negative of the equivalent system noise temperature.

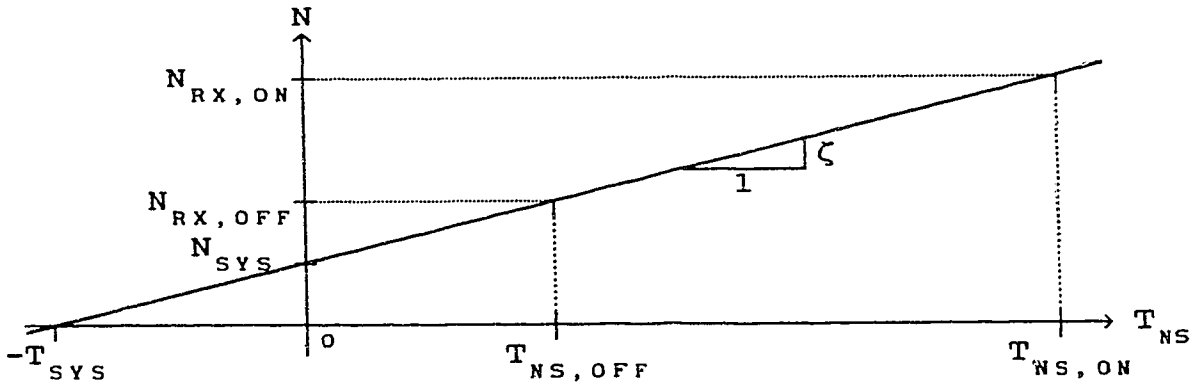

Figure 3.5: Graphical interpretation of the Y-factor calibration step.

The second step of the Y-factor technique is to insert the DUT between the noise source and the receiver as shown

in Figure 3.6. Two measurements are made, one at $T_{NS,OFF}$ and one at $T_{NS,ON}$, to determine $N'_{RX,OFF}$ and $N'_{RX,ON}$ respectively, thereby obtaining the necessary information to obtain the equation of the line shown in Figure 3.7.

T_{SYS} is computed using the Y-factor equation, which is easily found either algebraically or by using similar triangles in Figure 3.5:

$$T_{SYS} = \frac{T_{NS,ON} - YT_{NS,OFF}}{Y - 1} , \qquad (3.10)$$

$$\text{where} \quad Y = \frac{N_{RX,ON}}{N_{RX,OFF}} . \qquad (3.11)$$

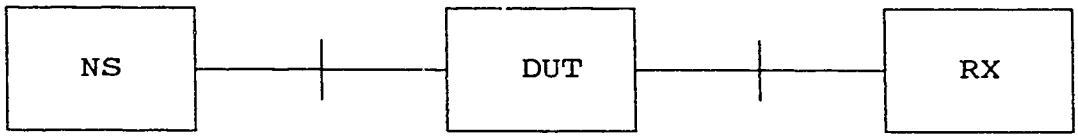

Figure 3.6 Apparatus for measurement of DUT noise temperature.

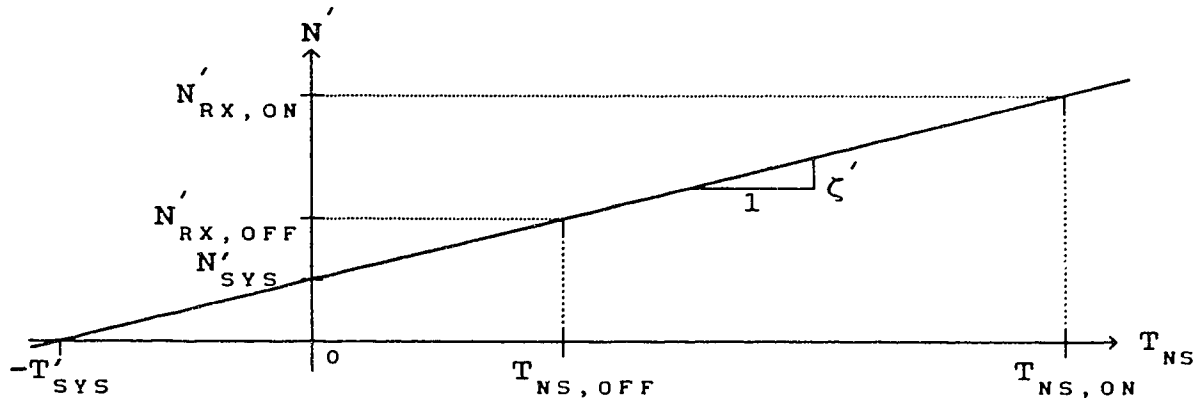

Figure 3.7: Graphical interpretation of the Y-factor measurement step.

The DUT operating power gain (equal to the available power gain for a matched system) is then determined from

$$G_{DUT} = \frac{\zeta'}{\zeta} = \frac{N'_{RX,ON} - N'_{RX,OFF}}{N_{RX,ON} - N_{RX,OFF}} \quad . \qquad (3.12)$$

and the total system noise temperature, T'_{SYS}, is obtained using equations similar to 3.10 and 3.11. A re-arranged version of the Friis equation (1.6) then gives the noise temperature of the DUT alone, T_{DUT}:

$$T_{DUT} = T'_{SYS} - \frac{T_{SYS}}{G_{DUT}} \quad . \qquad (3.13)$$

Although well suited to production testing of (nominally) matched components such as amplifiers, the classic Y-factor method has two disadvantages :

1. All components must be well matched for accurate results (the method is exact only for perfect matching)
2. Only a noise figure for the matched input condition is obtained. The full set of four noise parameters can not be determined directly by this method.

3.4 Noise Parameter Measurement by the Y-factor Method

Determining the noise parameters of the DUT requires the measurement of noise temperature at more than one value of noise source reflection coefficient. A tuner inserted between the noise source and the DUT as in Figure 3.8 provides a variable impedance to the DUT input. Tuning is

performed until the noise figure, determined by the Y-factor procedure, is a minimum. At this point the optimum reflection coefficient of the tuner output, Γ_{OPT}, can be measured with a suitable vector reflectometer. If the tuner is lossless, there is no effect on the noise temperature of the source seen by the DUT. This simple method does not compensate for the changing mismatch between a DUT which is not unilateral and the receiver. Inserting an isolator in front of the receiver input reduces this source of error to the noise contribution of the isolator itself.

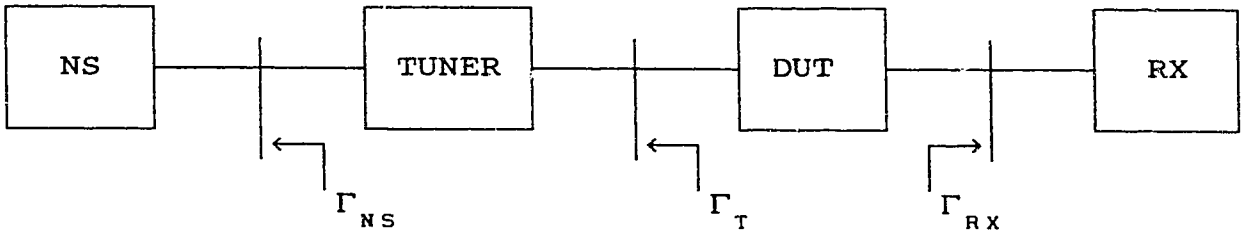

Figure 3.8: Noise parameter measurement apparatus (Y-factor method).

The major difficulty with this method is compensating for the loss of the tuner which alters the noise temperature of the composite noise generator (ie. tuner plus noise source). Generally, the tuner loss is a function of tuner settings, introducing a systematic error unless this loss is determined for each reflection coefficient of the noise generator. Correction is possible for room temperature measurements, where much a priori information is available about the noise apparatus (eg. S-parameters, physical temperature), but difficult, if not impractical, for

cryogenic measurements.

Cryogenic measurements impose an added constraint because a typical solid-state noise generator cannot be installed in the cryostat and connected directly to the cooled DUT, but must be outside and connected through a lossy line of unknown temperature gradient. This problem is addressed in Section 3.6.3.2 below.

Another source of error is change in the noise source reflection coefficient, Γ_{NS}, between the on and off states. Since the noise figure is a function of Γ_{NS}, the value of $F(\Gamma_{NS})$ becomes ambiguous if computed by the preceeding Y-factor method. Commercial manufacturers of noise sources attempt to minimize the reflection coefficient change by placing an attenuator after the noise diode, and supplying the unit as one calibrated package. The use of an attenuator, rather than an isolator, is required by the broadband nature of the commercial products. For narrow band applications, an external isolator can be added to eliminate Γ_{NS} changes, at the expense of having to re-calibrate the composite noise source. Hewlett-Packard calibrates HP346 noise sources using the noise power delivered to a 50 ohm load. Unless the source also has an impedance of 50 ohms, a small correction is required to obtain P_{AVS} of the noise source for such a re-calibration. Two calibration techniques are presented in section 3.6.

3.5 Mismatch Factors

Caruso and Sannino [3.8] introduced the useful concept

of the "mismatch factor" to compensate for junction mismatches. This factor, denoted μ, is defined as

$$\mu = \frac{P_L}{P_{AVS}} , \qquad (3.14)$$

where P_L is the power delivered to the load,
P_{AVS} is the power available from the source.

If the reflection coefficients of the load and source are known, as shown in Figure 3.3, the value of μ can be found from the equation

$$\mu = \frac{(1 - | \Gamma_{NS} |^2) (1 - | \Gamma_{RX} |^2)}{| 1 - \Gamma_{NS} \Gamma_{RX} |^2} . \qquad (3.15)$$

The mismatch factor is particularly useful in accounting for noise power transfer when writing equations for N-T diagrams in unmatched systems.

3.6 Tuner Loss Compensation

3.6.1 Method of Strid

Strid [3.9] presented a method of compensating for the tuner loss based on physical temperature, S-parameter, and reflection coefficient measurements. The method is applied for each state of the noise source, if Γ_{NS} is a function of noise source state. Referring to Figure 3.8, the value of Γ_T can be expressed as

$$\Gamma_T = S_{22} + \frac{S_{21}S_{12}\Gamma_{NS}}{1 - S_{11}\Gamma_{NS}} , \qquad (3.16)$$

where S_{ij} are the S-parameters of the tuner.

The available gain of the tuner $G_{A,T}$ is then

$$G_{A,T} = \frac{|S_{21}|^2 \ (1-|\Gamma_{NS}|^2)}{(1-|\Gamma_T|^2) \ |1-S_{11}\Gamma_{NS}|^2} . \qquad (3.17)$$

Once the physical temperature and available gain of the tuner (or any other two-port) are known, the effective noise temperature of the composite noise source referred to the tuner-DUT interface is given by

$$T_{COMP} = T_{NS}G_{A,T} + T_{T,PHYS}(1-G_{A,T}) , \qquad (3.18)$$

where T_{COMP} is the noise temperature of the composite NS,

$T_{T,PHYS}$ is the physical temperature of the tuner.

A major drawback of Strid's method for cryogenic application is the need to obtain S-parameters of the tuner at each position where noise figure is measured. Strid's experimental results also show a general trend of decreasing $G_{A,T}$ with increasing $|\Gamma_T|$. Such a systematic error, if uncorrected, would tend to result in underestimating the magnitude of Γ_{opt}.

3.6.2 Method of Martines and Sannino

Martines and Sannino [3.10] (hereinafter referred to as "MS") published a method whereby the tuner loss could be determined from noise power and reflection coefficient measurements only. Similar quantities are required for obtaining the noise parameters of the DUT by the Y-factor method previously described. This technique is therefore desirable since the noise measuring apparatus can also be used to determine the tuner loss compensation, without removal of the tuner to make S-parameter measurements as would be required using the method of Strid.

Figure 3.8 can be used again to represent the apparatus used by MS to estimate the tuner loss. Loss is defined here as the reciprocal of the available gain. The values of the three reflection coefficients Γ_{RX} , Γ_T and Γ_{NS} are required. Of these, only Γ_T varies as a function of tuner position; the remaining two reflection coefficients can be obtained once for the entire experiment. MS give the receiver noise figure as

$$F_R(\Gamma_T) = \frac{1}{\mu'} F_R(0) + \left(\frac{1}{\mu'} - 1 \right)\left(\frac{T_a}{T_0} - 1 \right) , \qquad (3.19)$$

where $$\mu' = \frac{1 - |\Gamma_T|^2}{|1 - \Gamma_{RX}\Gamma_T|^2}$$

and $F_R(\Gamma_T)$ is the noise figure of the RX

$F_R(0)$ is the value of F_r when $\Gamma_T = 0$

T_a is the (ambient) temperature of the tuner

T_0 is the reference temperature (290K).

For a matched noise source, the tuner loss can then be obtained using the relation

$$F_{RT}(0) = \frac{1}{G_{A,T}} F_R(\Gamma_s) \quad , \tag{3.20}$$

where $F_{RT}(0)$ is the noise figure of the RX-tuner cascade with $\Gamma_{NS} = 0$

$G_{A,T}$ is the available gain of the tuner.

While the method of MS is of interest, it fails to solve two problems important in cryogenic measurements:

1. The lossy transmission line leading into the cryostat has a variable temperature gradient, so the "effective" physical temperature of this cable is unknown.
2. The apparatus of MS requires seperate insertion of the tuner. This is difficult inside a cryostat. Replacement of the tuner by a cable (either manually or by relays) is feasible, but not compensated for by the method of MS.

Additional extensions to the method are provided by MS to cover those cases in which Γ_{NS} varies between the ON and OFF states. However, this correction limits the method to

determining the tuner loss; transistor noise parameters cannot be obtained due to the Γ_{NS} ambiguity. An isolator attached to the noise source can be used to overcome this difficulty.

3.6.3 The New Loss Compensation Method

A method introduced by MS [3.10] and outlined in the previous section shows how unavoidable losses may be corrected for, in the tuner network used as the noise source admittance transformer. As discussed above, application of their method to microwave transistor noise parameter measurements requires only noise figure measurements and tuner reflection coefficient measurements for specific tuner settings. However, the method of MS is limited to measurements in which the physical temperature of the tuner is known. For cryogenic noise parameter measurements with a switched noise source outside the cryostat, the cable connecting the noise source to the tuner inside the cryostat will have unavoidable losses, and will have a temperature gradient along its length. Furthermore, the temperature of the inner conductor will in general be different from the temperature of the outer conductor at each point along the cable. This thesis extends the method of MS to cryogenic measurements by taking into account the effects of the cable, using only noise power measurements and reflection coefficient measurements, and it also presents an alternative derivation of the method of MS.

3.6.3.1 Tuner Loss Compensation

This section describes the use of noise power - temperature diagrams to derive equations for the compensation of a two-port of known physical temperature. The available gain of the two-port is obtained from noise power and reflection coefficient measurements only, in a manner analogous to that of MS.

The noise power measurements, represented schematically in Figures 3.9 and 3.10, are performed sequentially. In Fig. 3.9(a), the noise source "NS" is connected directly to the receiver "RX", but in the configuration of Fig. 3.10(a), an arbitrary passive network, "X", is interposed between the noise source and the receiver. This network might be, for example, the tuning network used by MS. For one particular setting, the network has available gain $G_{A,X}$ and an output reflection coefficient $\Gamma_{X,ON/OFF}$ which may depend on the state of the noise source ("ON" or "OFF"). The passive network is assumed to be at ambient temperature, T_a, which is not, in general, 290 K.

It is first necessary to measure the reflection coefficients $\Gamma_{NS,ON}$, $\Gamma_{NS,OFF}$, Γ_{RX}, $\Gamma_{X,ON}$, and $\Gamma_{X,OFF}$. Then, using the configuration of Fig. 3.9(a), the noise powers $N_{NS,ON}$ and $N_{NS,OFF}$ indicated by the receiver are noted. Using the configuration of Fig. 3.9(b), the noise powers $N_{X,ON}$ and $N_{X,OFF}$ are recorded. The noise power - temperature diagrams corresponding to Fig. 3.9(a) and Fig. 3.10(a) are given in Fig 3.9(b) and Fig. 3.10(b),

respectively. The quantities N_{RX} and N_{X_0} are intercepts. The noise power available from the noise source is related to its noise temperature by the expression $kT_{NS,ON/OFF}B$, where B is the receiver noise bandwidth and k is Boltzmann's constant.

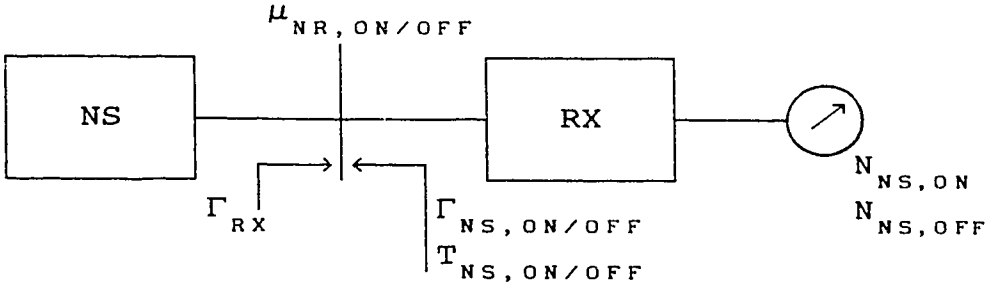

(a) Apparatus configuration for calibration in a mismatched system.

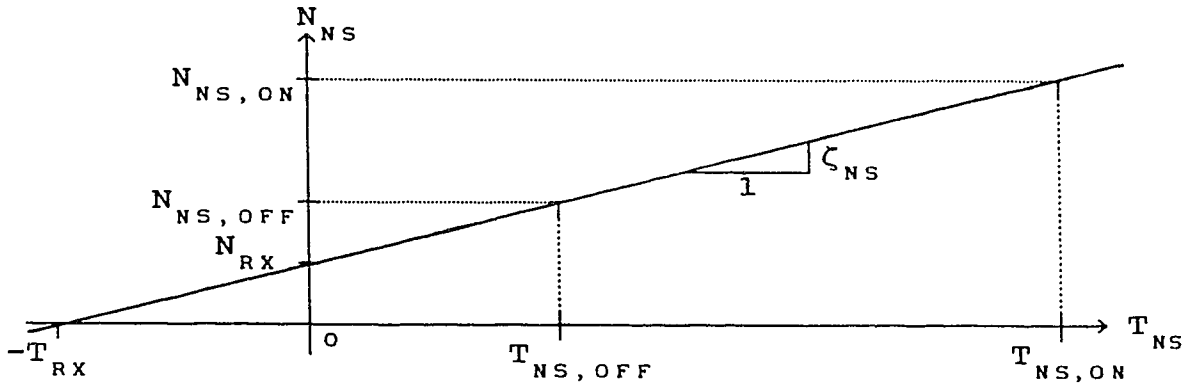

(b) N-T diagram for apparatus of (a) above.

Figure 3.9: Calibration of mismatched system.

In Figures 3.9(a) and 3.10(a) the mismatch factors indicated have the values

$$\mu_{NR,ON/OFF} = \frac{(1 - |\Gamma_{NS,ON/OFF}|^2)(1 - |\Gamma_{RX}|^2)}{|1 - \Gamma_{RX}\Gamma_{NS,ON/OFF}|^2} \qquad (3.21)$$

and

$$\mu_{XR,ON/OFF} = \frac{(1 - |\Gamma_{X,ON/OFF}|^2)(1 - |\Gamma_{RX}|^2)}{|1 - \Gamma_{RX}\Gamma_{X,ON/OFF}|^2} \quad . \tag{3.22}$$

As before, "ON" and "OFF" refer to the state of the noise source. It is not assumed that $\Gamma_{NS,ON} = \Gamma_{NS,OFF}$.

From Fig. 3.9(b), two equations can be written relating the noise power indicated by the receiver to the equivalent temperature of the noise source:

$$N_{NS,ON} = \mu_{NR,ON} k G_{RX} T_{NS,ON} B + N_{RX} \tag{3.23}$$

and

$$N_{NS,OFF} = \mu_{NR,OFF} k G_{RX} T_{NS,OFF} B + N_{RX} \quad . \tag{3.24}$$

In these equations, G_{RX} is the "receiver gain", which is defined (as in Section 3.1 above) as the ratio of the power indicated by the receiver, excluding the noise power N_{RX} produced within the receiver itself, to the power which is absorbed at the receiver input. It is assumed that N_{RX} does not depend on the state of the noise source. This condition can be approximated by incorporating an isolator at the receiver input. The available gain $G_{A,X}$ of the passive network, which is the quantity to be found, refers to a particular network setting.

Two equations can also be written from Fig. 3.10(b):

$$N_{X,ON} = \mu_{XR,ON} k G_{A,X,ON} G_{RX} T_{NS,ON} B + N_{X_o} \tag{3.25}$$

and

$$N_{X,OFF} = \mu_{XR,OFF} k G_{A,X,OFF} G_{RX} T_{NS,OFF} B + N_{X_O} . \qquad (3.26)$$

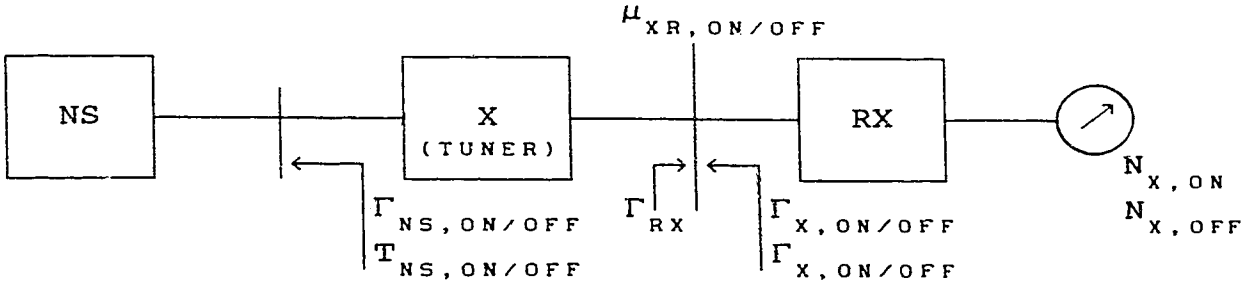

(a) Apparatus connection and measurements for network X (eg. a tuner) loss compensation.

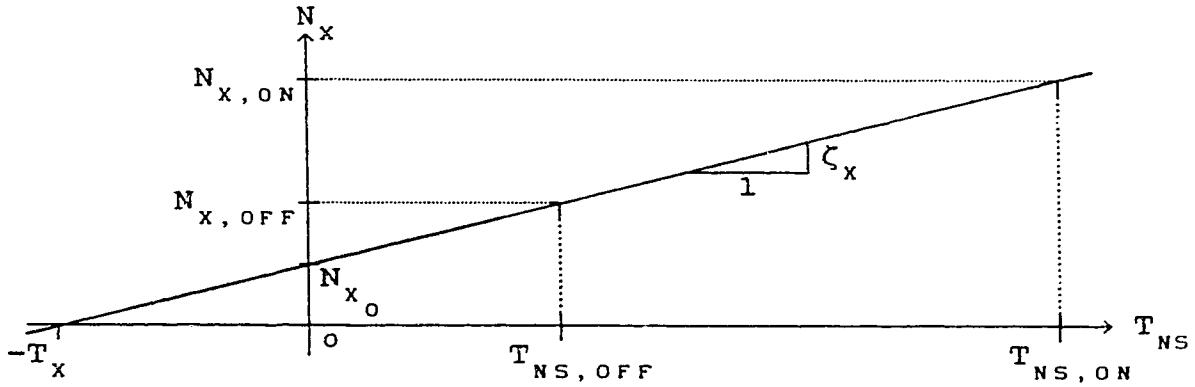

(b) N-T diagram for apparatus of (a) above.

Figure 3.10: Estimation of inserted network loss.

Here N_{X_O} represents the noise power produced within the receiver and the passive network, and is assumed not to depend on the state of the noise source.

Using (3.23) and (3.24), the slope of the noise power - temperature diagram in Fig. 3.9(b) can now be written:

$$\zeta_{NS} = \frac{N_{NS,ON} - N_{NS,OFF}}{T_{NS,ON} - T_{NS,OFF}}$$

$$= \frac{k G_{RX} B (\mu_{NR,ON} T_{NS,ON} - \mu_{NR,OFF} T_{NS,OFF})}{T_{NS,ON} - T_{NS,OFF}} . \qquad (3.27)$$

Using (3.25) and (3.26), the slope of the noise power - temperature diagram in Fig. 3.10(b) is likewise

$$\zeta_x = \frac{N_{X,ON} - N_{X,OFF}}{T_{NS,ON} - T_{NS,OFF}}$$

$$= \frac{kG_{RX}B(\mu_{XR,ON}G_{A,X,ON}T_{NS,ON} - \mu_{XR,OFF}G_{A,X,OFF}T_{NS,OFF})}{T_{NS,ON} - T_{NS,OFF}} \quad . \tag{3.28}$$

The ratio of these two slopes is:

$$\frac{\zeta_x}{\zeta_{NS}} = \frac{\mu_{XR,ON}G_{A,X,ON}T_{NS,ON} - \mu_{XR,OFF}G_{A,X,OFF}T_{NS,OFF}}{\mu_{NR,ON}T_{NS,ON} - \mu_{NR,OFF}T_{NS,OFF}} \quad . \tag{3.29}$$

It is now possible to evaluate the two values of the available gain of the network, as follows. Generally, if the S-parameters of the network were known, we could use equation 3.17 to write

$$G_{A,X}(\Gamma_{NS}) = \frac{|S_{21}|^2(1 - |\Gamma_{NS}|^2)}{|1 - S_{11}\Gamma_{NS}|^2 \ (1 - |\Gamma_X(\Gamma_{NS})|^2)} \quad . \tag{3.30}$$

For typical noise sources, however, Γ_{NS} is small in both the "ON" and "OFF" condition. For example, $|\Gamma_{NS}| \cong 0.02$ for both "ON" and "OFF", with worst-case values 2.5 times larger than this [3.11]. If, as is sometimes done, an attenuator is incorporated into the noise source, this value of Γ_{NS} becomes even closer to zero. For example, the HP346A noise source is specified to have a reflection coefficient

differential between states of no greater than 0.01. If necessary, an isolator can be attached to the noise generator and this composite source re-calibrated. Then, with little error,

$$G_{A,X}(\Gamma_{NS,ON/OFF}) \approx \frac{|S_{21}|^2}{(1-|\Gamma_{X,ON/OFF}|^2)} , \tag{3.31}$$

so that

$$\frac{\zeta_X}{\zeta_{NS}} = \frac{\dfrac{\mu_{XR,ON}T_{NS,ON}|S_{21}|^2}{(1-|\Gamma_{X,ON}|^2)} - \dfrac{\mu_{XR,OFF}T_{NS,OFF}|S_{21}|^2}{(1-|\Gamma_{X,OFF}|^2)}}{\mu_{NR,ON}T_{NS,ON} - \mu_{NR,OFF}T_{NS,OFF}} . \tag{3.32}$$

However, $\mu_{XR,ON/OFF}$ is given by (3.22). Then,

$$|S_{21}|^2 =$$

$$\left\{\frac{\zeta_X}{\zeta_{NS}}\right\} \frac{\mu_{NR,ON}T_{NS,ON} - \mu_{NR,OFF}T_{NS,OFF}}{(1-|\Gamma_{RX}|^2)\left\{\dfrac{T_{NS,ON}}{|1-\Gamma_{RX}\Gamma_{X,ON}|^2} - \dfrac{T_{NS,OFF}}{|1-\Gamma_{RX}\Gamma_{X,OFF}|^2}\right\}} . \tag{3.33}$$

But from (3.27) and (3.28),

$$\frac{\zeta_X}{\zeta_{NS}} = \frac{N_{X,ON} - N_{X,OFF}}{N_{NS,ON} - N_{NS,OFF}} , \tag{3.34}$$

i.e., this ratio is immediately calculable from the measurements. Hence $|S_{21}|^2$ can be found from (3.33) and the two values of the available gain of the network $G_{A,X,ON}$ and

$G_{A,X,OFF}$ can be calculated using (3.31). This achieves the desired result and is important in simplifying accurate noise measurements, since the experimental data recorded using the configuration of Fig. 3.9(a) need only be obtained once. Without removing the passive network to perform S-parameter measurements, the measurements of Fig. 3.10(a) then supply all the information required to compute the available gain of the passive network at any setting, and the equivalent noise temperature of the composite noise source represented by the passive network and noise source together. When measuring noise parameters, the value of Γ_X must be known in any case, since this is the generator reflection coefficient presented to the DUT.

Finally, it is of interest to use the available gain of the passive network and its physical temperature $T_{X,AMBIENT}$ to write the equivalent noise temperature of the composite noise source:

$$T_{X,ON/OFF} = G_{A,X,ON/OFF}T_{NS,ON/OFF} + (1-G_{A,X,ON/OFF})T_{X,AMBIENT}. \quad (3.35)$$

3.6.3.2 Cryogenic Measurements

In cryogenic measurements of noise parameters, additional difficulties are encountered with connection and calibration of apparatus. As in Fig. 3.11, the switched noise source (frequently a commercial solid-state device) usually remains outside the cryostat while the DUT must be placed inside. The tuner is also frequently placed inside

the cryostat (eg. Weinreb [3.12], Pospieszalski[3.13]). Two problems which arise as a result of this configuration are:

1. The available gain and effective noise temperature of the cable leading from the noise source to the tuner are unknown.
2. It is desirable to be able to "bypass" the tuner, e.g. with remotely controlled relays, so that the previous method of tuner loss compensation described in the previous section can be used.

Placing the tuner outside the cryostat exacerbates problem (1) above, since the available gain of the input cable then varies with the tuner setting.

The following describes a new method which combines the methods of MS and of Strid [3.9] to provide a calibration of the composite noise source comprising the cable and the switched noise source. The "end" of the cable need not be an actual connector, however; it can be a point inside a test fixture if desired. Finally, the use of the new method to compensate for the added tuner loss is described in this section.

Obtaining the cable noise properties from physical temperature considerations is difficult. In general, the effective noise temperature available at the cold end of the cable would be given by

$$T_{C,ON/OFF} = T_{NS,ON/OFF} G_{A,C} + \int_{X=0}^{X=L} T(x)\,(1-G_{A,C}(x))\,dx. \qquad (3.36)$$

The noise contributed by the cable itself is difficult to calculate, however, since the temperature distribution $T(x)$ along the length of the cable is not generally known, and furthermore the temperatures of the outer conductor, inner conductor, and dielectric at each point "x" along the length "L" of the cable are generally unequal and unknown. However, a solution using only the normally required cable reflection coefficient Γ_c plus noise power measurements is possible, as presented below.

In the following analysis it will be assumed that the noise measuring receiver, or at least its front-end amplifier, is located in the cryostat, so as to minimize the noise contributed by the receiver. A cooled receiver input isolator is added to minimize changes in receiver noise temperature due to changes in the reflection coefficient presented to the receiver. It is further assumed that the noise source also incorporates an isolator or attenuator, so that $\Gamma_{NS,ON} = \Gamma_{NS,OFF}$. The objective will be to find the noise temperatures available at the cold end of the cable, $T_{C,ON/OFF}$.

Figure 3.11 shows the connections required and the reflection coefficients and mismatch factors involved. It is assumed that the S-parameters of the cable are known, but the physical temperature is not required anywhere along or within the cable. The S-parameters would normally be required to de-embed the reflection coefficient measurements made inside the cryostat, so this requirement imposes little, if any, extra work upon the experimenter. Also

assumed known is the reflection coefficient Γ_C which the cable presents, as in Fig. 3.11(b), at the end inside the cryostat, when the exterior end is connected to the noise source. Fig. 3.12 shows the noise power - temperature diagram for the connections in Fig. 3.11(a) and (b).

The measurements indicated in Fig 3.11(a) and (b) give the values $N_{C,ON}$ and $N_{C,OFF}$ but cannot locate the line in Fig. 3.12, whose equation is

$$N_C = \mu_{CR} k G_{A,C} G_{RX} T_{NS} B + N_{C_o} = \zeta_C T_C + N_{C_o}, \qquad (3.37)$$

because $T_{C,ON}$ and $T_{C,OFF}$ are still uncertain. However, if it were possible to establish the intercept N_{C_O} and the slope ζ_C, the position of the line would be established and the values for $T_{C,ON}$ and $T_{C,OFF}$ could be found. From (3.37), knowledge of $G_{A,C}$ of the cable would in itself be insufficient without knowledge of the intercept N_{C_O} as well; the method of Strid alone is therefore insufficient.

In Fig. 3.11(a), the tuner is shown connected directly to a load of some admittance which is located inside the cryostat and whose physical temperature is the same as that of the tuner, say $T_{G,PHYS}$. At this point, the tuner is adjusted to present a reflection coefficient Γ_T which is the same as that presented by the cable, Γ_C, and the noise power $N_{C,PHYS}$ at the receiver output is measured. Since the load and tuner together represent a passive device of known temperature, $T_{G,PHYS}$, with the desired reflection

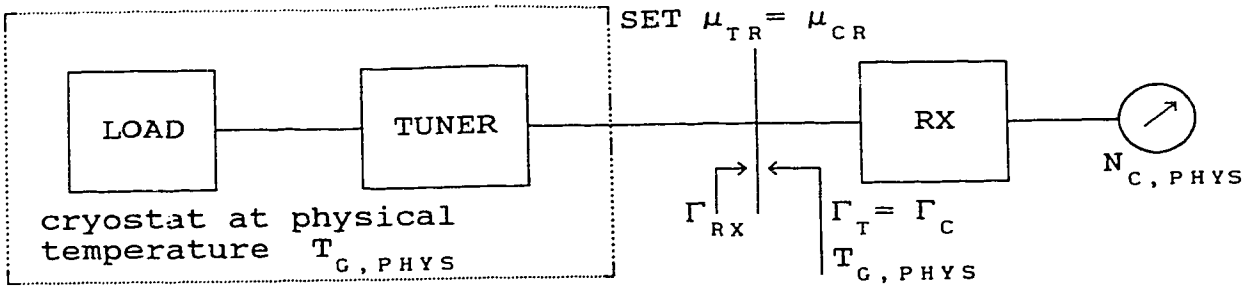

(a) Configuration for measurement of cooled load at a physical temperature of $T_{G,PHYS}$.

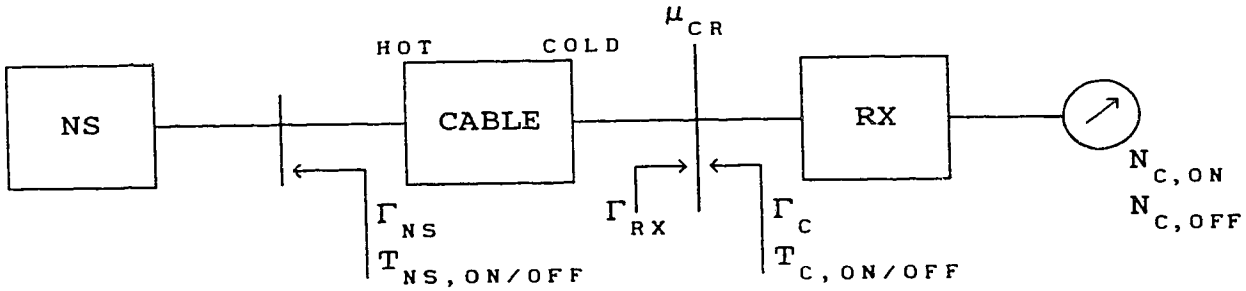

(b) Apparatus connection using a cable feed to the RX with an unknown temperature gradient.

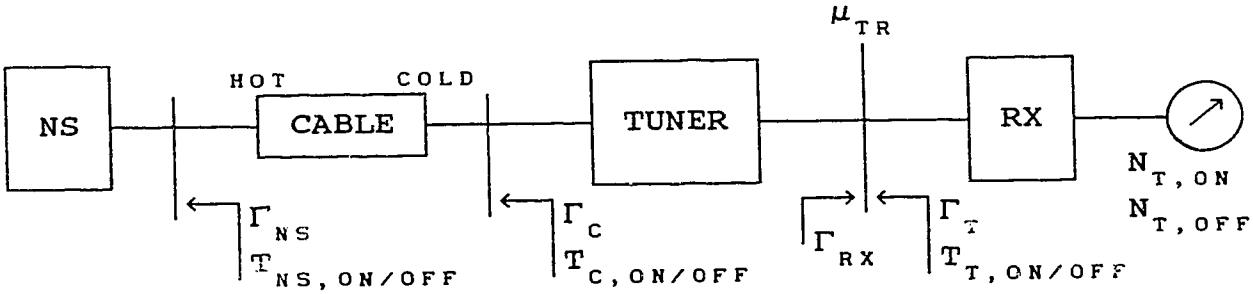

(c) Connection of equipment to measure the noise temperature of the cooled tuner output.

Figure 3.11: Calibration of the tuner noise temperature inside a cryostat.

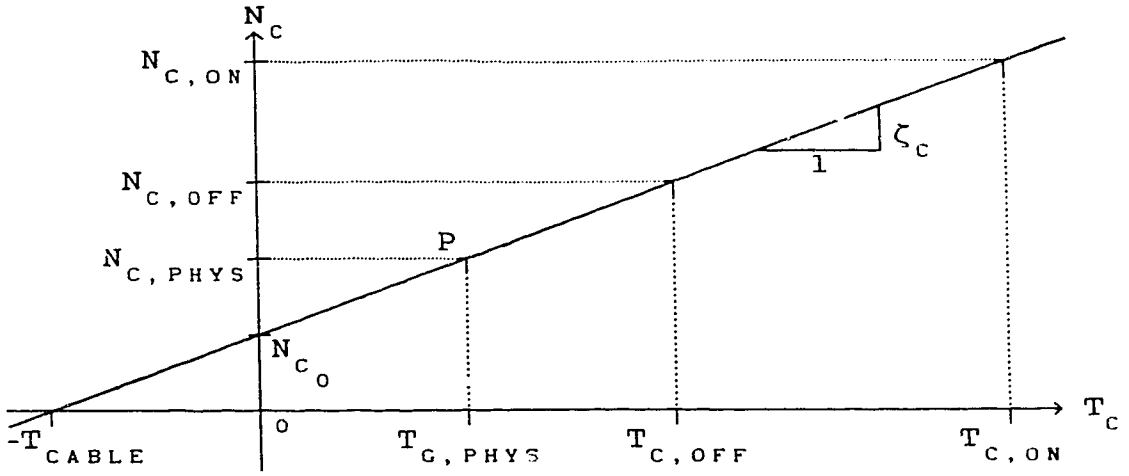

Figure 3.12: N-T diagram for the configuration of Fig. 3.11(a) and (b).

coefficient, Γ_C, then $N_{C,PHYS}$ must be the noise power value on the desired line, corresponding to the T_C value of $T_{G,PHYS}$. This gives the needed extra piece of information, and the point "P" can now be located on Fig. 3.12. Setting Γ_T equal to Γ_C provides the additional benefit that errors in the measurement of Γ_T do not affect this part of the calibration; the value of Γ_T is not required for the cable noise temperature calibration.

Using the S-parameters of the cable, the available gain $G_{A,C}$ of the cable can be calculated. The S-parameter de-embedding procedures discussed in chapter 2 yield the quantity $S_{12}S_{21}$ of the cable. Assuming reciprocity, $S_{21} = S_{12} = (S_{12}S_{21})^{1/2}$. Expressions for the equivalent noise temperature available at the cold end of the cable in Fig. 3.11(b) can now be written with the noise source ON and OFF:

$$T_{C,ON} = T_{NS,ON}G_{A,C} + (1-G_{A,C})T_{C,EFF} \qquad (3.38)$$

$$T_{C,OFF} = T_{NS,OFF} G_{A,C} + (1-G_{A,C}) T_{C,EFF} \quad . \tag{3.39}$$

In these equations, the effective noise temperature of the cable, $T_{C,EFF}$, remains unknown, but the receiver output noise power indicated with the noise source ON and OFF in Fig. 3.13(a) has been recorded as the two values $N_{C,ON}$ and $N_{C,OFF}$, respectively. If we now exploit the fact that we know $G_{A,C}$, the slope ζ_C of the line in Fig 3.12 is known and can be written as

$$\zeta_C = \frac{N_{C,ON} - N_{C,OFF}}{T_{C,ON} - T_{C,OFF}}$$

$$= \frac{N_{C,ON} - N_{C,OFF}}{G_{A,C}(T_{NS,ON} - T_{NS,OFF})} \quad . \tag{3.40}$$

Using point "P" in Fig. 3.12, it can be seen that the intercept N_{C_o} is given by

$$N_{C_o} = N_{C,PHYS} - \zeta_C T_{G,PHYS} \quad . \tag{3.41}$$

It is therefore possible to evaluate $T_{C,ON}$ and $T_{C,OFF}$:

$$T_{C,ON} = \frac{N_{C,ON} - N_{C_o}}{\zeta_C} \tag{3.42}$$

$$T_{C,OFF} = \frac{N_{C,OFF} - N_{C_o}}{\zeta_C} \quad . \tag{3.43}$$

These equations represent a calibration of the noise source at the cable - receiver interface inside the cryostat, corrected for the loss of the tuner and the loss

of the cable, without regard for the temperature distribution along the cable. The value for $T_{C,OFF}$, in particular, is important: simply estimating the temperature gradient along the cable, if it is a low-loss cable, would result in errors of little importance in $T_{C,ON}$, which is usually much larger than the noise temperature of the cooled transistor under test, but the same cannot be said for the errors which would be incurred in evaluating $T_{C,OFF}$. The method presented here provides a convenient means of noise source calibration inside the cryostat, without the need of special "thermal breaks" in the RF feedlines or simplifying assumptions about tuner and cable loss effects.

Although not required in the foregoing procedure, a value for the effective noise temperature of the cable can also be found. From (3.39), it is

$$T_{C,EFF} = \frac{T_{C,OFF} - T_{NS,OFF} G_{A,C}}{1 - G_{A,C}} \quad . \tag{3.44}$$

This value can be used as a check, since the value obtained for $T_{C,EFF}$ must be in reasonable agreement with the estimated physical temperature of the cable.

The apparatus is then reconnected as shown in Figure 3.11(c) for tuner loss compensation. The noise temperatures at the cable end are now known, and the method described in section 3.6.3.1 can be applied.

Fig. 3.13 shows the tuner in the cryostat connected to the cold end of the cable. The DUT, e.g. a transistor in a

test fixture, is shown connected between the tuner and the receiver. The method of MS outlined previously can be applied immediately to correct for tuner loss, substituting Γ_C for Γ_{NS} and $T_{C,ON/OFF}$ for $T_{NS,ON/OFF}$. The assumption in MS that the tuner is at the same physical temperature as the cold state of the noise source is of course not valid, and its physical temperature must be substituted in the equations of MS, or in the procedure of section 3.6.3.1. All other quantities marked in Fig. 3.13 are known, or will be ascertained by use of the MS method. Equations similar to (3.38) and (3.39) can be used to obtain $T_{T,ON/OFF}$.

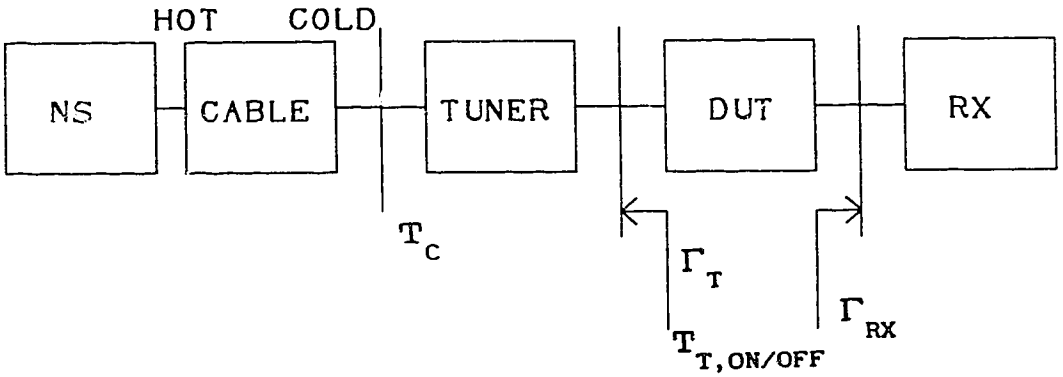

Figure 3.13: Configuration for the measurement of DUT noise figure using noise calibration at the tuner output (T_T).

3.6.3.3 Tuner Bypass Correction

In the previous sections, derivations were based on the assumption that two-port devices could be inserted at arbitrary locations denoted by reference planes. When the tuner is placed inside the cryostat with remotely actuated bypass relays, however, this assumption is not justified.

In cryogenic measurements, calibration and interconnection at specific reference planes is inconvenient. Insertion (eg. of a DUT) would require splitting the RF circuit and adjusting the shape of coax cables, etc. to accommodate the device. An easier solution is to use bypass lines connected by relays, but this does not constitute an insertion in the sense required by the foregoing derivations. For example, the additional bypass line introduces both loss and phase shift. This section discusses the issues of interconnection and shows how this difficulty can be remedied.

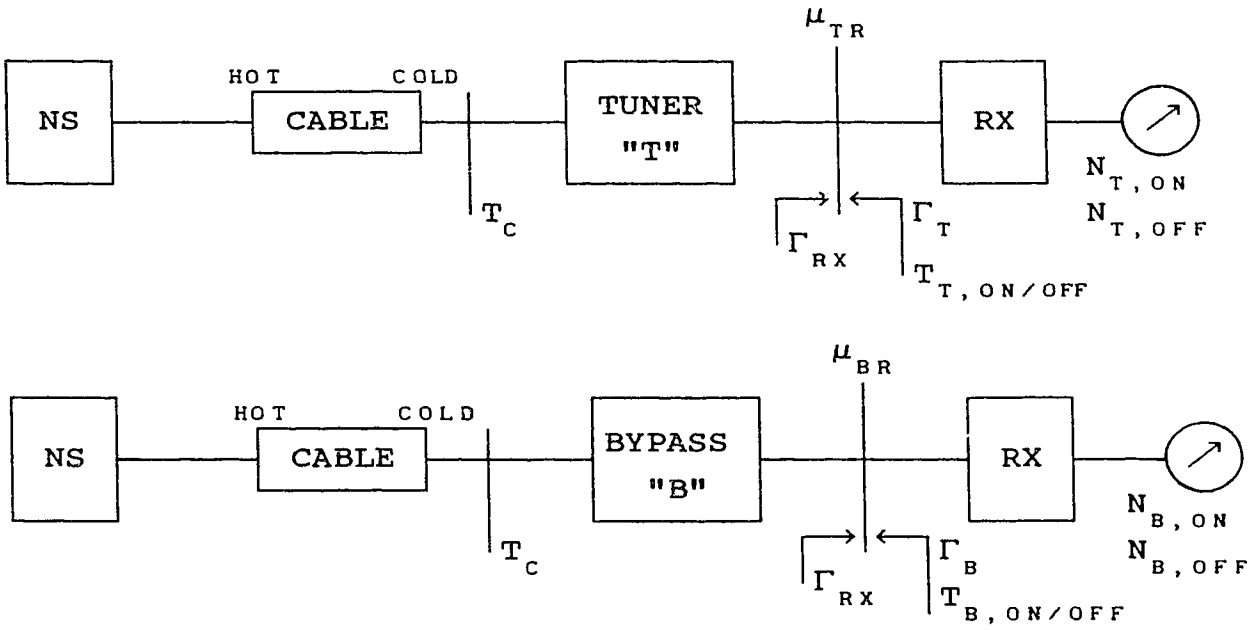

Figure 3.14: Replacement of the tuner with a two-port bypass network.

Fig 3.14 shows the replacement of the tuner "T" by a bypass "B". The reference plane at T_C is chosen so that the tuner and the bypass both have physical temperature T_{PHYS}, and so that no part of the cable two-port is involved in the

switching. When the equivalent noise temperatures T_T and T_B are obtained as described previously, the values of the products $G_{A,C}G_{A,T}$ and $G_{A,C}G_{A,B}$ are obtained, as are the values of the noise temperatures T_T and T_B. Using the same method of analysis as in section 3.6.3.1 it can be shown that

$$\frac{G_{A,T}}{G_{A,B}} = \frac{G_{A,C}G_{A,T}}{G_{A,C}G_{A,B}} = \frac{\mu_{BR}\zeta_T}{\mu_{TR}\zeta_B} , \tag{3.45}$$

where ζ_B and ζ_T are the slopes of the N-T diagrams corresponding to Figure 3.14(a) and (b), respectively, and

$$\mu_{TR} = \frac{(1-|\Gamma_T|^2)(1-|\Gamma_{RX}|^2)}{|1-\Gamma_T\Gamma_{RX}|^2} \tag{3.46}$$

and

$$\mu_{BR} = \frac{(1-|\Gamma_B|^2)(1-|\Gamma_{RX}|^2)}{|1-\Gamma_B\Gamma_{RX}|^2} . \tag{3.47}$$

The effective noise temperatures T_T and T_B then become

$$T_T = T_C G_{A,T} + (1-G_{A,T})T_{PHYS} \tag{3.48}$$

and

$$T_B = T_C G_{A,B} + (1-G_{A,B})T_{PHYS} . \tag{3.49}$$

Then from (3.48) and (3.49) we find that the noise temperature of the tuner is given by

$$T_T = \left(\frac{G_{A,T}}{G_{A,B}}\right)(T_B - T_{PHYS}) + T_{PHYS} . \tag{3.50}$$

The reference plane at T_C is required only for this derivation and need not have any physical counterpart. However, it does illustrate that no switching (eg. by relays) may be done in the section of line with a temperature gradient; to do so would invalidate the assumptions used to derive (3.50).

A single initial calibration, using the new method described, can be utilized to yield a value of T_B. The value of T_B is obviously independent of tuner setting, so T_B remains unchanged for all experiments. Comparison measurements between the noise power readings at the tuner and bypass position provide the ratio ζ_T/ζ_B required by (3.44). The mismatch factor μ_{BR} need only be determined once. An estimate of μ_{TR} is required for each tuner setting. However, with suitable arrangement of the apparatus, this information would have to be obtained anyway as the reflection cefficient seen by the DUT. The result of (3.44) can then be used in (3.49) to obtain the equivalent noise temperature seen by the DUT and will permit an accurate Y-factor measurement of the DUT noise figure to be made at a known source reflection coefficient.

3.6.3.4 Receiver Isolator Available Gain Correction

In the foregoing analysis, the noise contribution of the receiver, denoted T_{RX} (or N_{RX} for the noise power contribution), was assumed constant as a consequence of having an isolator at the receiver input. This assumption is invalid, except for the theoretical case of a lossless

and unilateral isolator. This error, as estimated from the simulations of Chapter 5, is approximately 3K for a HEMT and 15K for a passive DUT, for measurements in the vicinity of $\Gamma_{opt.}$

T_{RX} can be expressed in terms of contributions from the isolator and receiver as:

$$T_{RX} = T_{ISO} + \frac{T'_{RX}}{G_{A,ISO}} \tag{3.51}$$

where T_{RX} = the total receiver noise temperature, referred to the isolator input,

T'_{RX} = the noise temperature of the receiver, excluding the isolator, referred to the isolator output,

T_{ISO} = the isolator noise temperature, referred to its input,

$G_{A,ISO}$ = the available gain of the isolator.

The value of T_{ISO} and $G_{A,ISO}$ will vary with the output reflection coefficient of the preceding network; however, T'_{RX} will not change if the isolator is unilateral. The effect of T'_{RX} will therefore vary as a consequence of the isolator available gain changes.

Although the effect of T_{ISO} may not be easy to correct for in cryogenic measurements where $G_{A,ISO}$ cannot be obtained, the correction may be possible in other

experiments. If the physical temperature and available gain of the isolator are known, then the noise contribution of the isolator would simply be:

$$T_{ISO} = (1-G_{A,ISO})T_{PHYS,ISO} \quad . \tag{3.52}$$

MS have derived the required expressions for an isolator with $S_{12} = 0$, and known available gain. The cryogenic apparatus, described in Chapter 4, does not permit measurement of the isolator available gain. Furthermore, the device is not likely to behave perfectly unilaterally, and some small variation in T'_{RX} must be expected.

The following method does not correctly compensate for certain receiver noise effects. Specifically, it does not correct for changes in T_{ISO} and T'_{RX} due to changes in the output reflection coefficient of the DUT. However, it is possible to obtain a correction for the effects of the isolator available gain. For the case of a perfect isolator (unilateral and lossless), the method is exact.

The available gain of the isolator is defined as

$$G_{A,ISO} = \frac{P_{AVN}}{P_{AVS}} \tag{3.53}$$

where P_{AVN} is the power available from the network preceding the isolator

and P_{AVS} is the power available at the output of the isolator.

A new property of the isolator, denoted G'_{ISO} can be defined as

$$G'_{ISO} = \frac{P_{AVN}}{P_{IN}} \tag{3.54}$$

where P_{IN} = the power absorbed by the isolator from the network

The value of G'_{ISO} is a function only of the isolator, and not of the networks in which it may be embedded. The relationship between G'_{ISO} and $G_{A,ISO}$ can then be expressed as

$$G_{A,ISO} = \frac{P_{IN}}{P_{AVS}} \frac{P_{AVN}}{P_{IN}} = \mu G'_{ISO} \tag{3.55}$$

where μ is the mismatch factor at the isolator input.

If changes in T_{ISO} and T'_{RX} are ignored, then for two measurements of receiver noise temperature with different impedances seen by the isolator, the following two equations apply:

$$T_{RX_1} = T_{ISO} + \frac{T'_{RX}}{\mu_1 G'_{ISO}} \tag{3.56}$$

and

$$T_{RX_2} = T_{ISO} + \frac{T'_{RX}}{\mu_2 G'_{ISO}} . \tag{3.57}$$

From equation 3.56 above,

$$\frac{\mu_1}{\mu_2} T_{RX_1} = \frac{\mu_1}{\mu_2} T_{ISO} + \frac{T'_{RX}}{\mu_2 G'_{ISO}} \qquad (3.58)$$

and therefore

$$\frac{T'_{RX}}{\mu_2 G'_{ISO}} = \frac{\mu_1}{\mu_2} \left(T_{RX_1} - T_{ISO} \right) . \qquad (3.59)$$

Substituting 3.59 into 3.57 gives

$$\begin{aligned} T_{RX_2} &= T_{ISO} + \frac{\mu_1}{\mu_2} \left(T_{RX_1} - T_{ISO} \right) \\ &= \frac{\mu_1}{\mu_2} T_{RX_1} + \left(1 - \frac{\mu_1}{\mu_2} \right) T_{ISO} . \end{aligned} \qquad (3.60)$$

For a low-loss isolator cooled to a low physical temperature, T_{ISO} should be small and the new value of receiver noise temperature can be estimated as

$$T_{RX_1} \approx \frac{\mu_1}{\mu_2} T_{RX_2} . \qquad (3.61)$$

This technique was used in the simulations of Chapter 5 and was found to enhance accuracy greatly. Changes in isolator available gain are accounted for, although the isolator noise contribution changes cannot be corrected. For the special case of $T_{ISO} = 0$, the method is exact.

3.7 Effects of Feedback and Cascade Networks on Noise Parameters

Design of noise parameter measurement apparatus requires knowledge of the effects of networks in which the DUT will be embedded. Feedback and/or cascade networks may be added to a two-port (often a transistor) either as part of an intended circuit or as unintentional parasitic elements. Understanding the behaviour of noise properties under such conditions is, therefore, required for analysis. Fig. 3.15 illustrates the various connections of an arbitrary network (X) to the network under consideration (N). For example, the effect of source lead inductance on a transistor amplifier are of particular interest to amplifier designers.

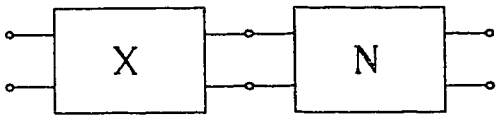

(a) Input network connection.

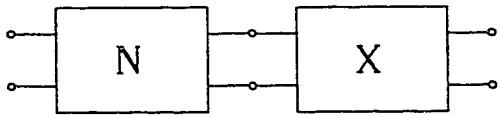

(b) Output network connection.

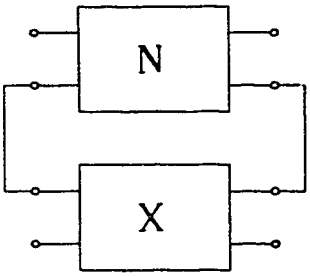

(c) Series feedback connection.

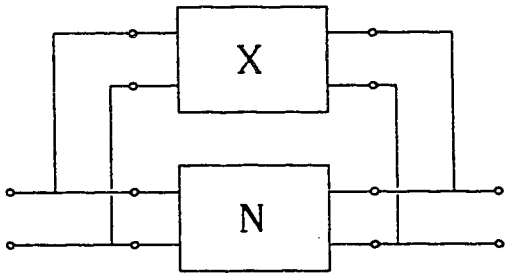

(d) Parallel feedback connection.

Figure 3.15: Various two-port connections.

Several researchers have undertaken to analyze the problem of using noisy networks in the configuration shown in Figure 3.15, and a brief overview of this literature follows.

The concept of noise measure and some associated theorems were introduced by Haus and Adler [3.14]. Lange [3.3] used the noise figure equation (3.3) and Y-parameter analysis to show that certain noise parameters would remain invariant to transformation by a lossless input network as shown in Figure 3.15(a). The resulting equation ,

$$F(Y_S) = F_{OPT} + \frac{N|Y_S - Y_{OPT}|^2}{Re\{Y_{OPT}\}\, Re\{Y_S\}} \qquad (3.62)$$

where $F(Y_S)$ is the noise figure,

N is a constant,

Y_S is the source admittance,

Y_{OPT} is the source admittance yielding the minimum noise figure,

has two constants, F_{OPT} and N, which are invariant to transformation by a lossless input network. Y_{OPT} is not invariant, but is changed in the same manner as the network input impedance.

A general solution to the input network, series and parallel feedback problem was published by Hartmann and Strutt [3.15]. The solutions provided do not account for noisy elements used in the external networks. Although Hartmann and Strutt stated that this can be accommodated by

linear superposition of the noise sources, no further details were provided.

Several papers have been published specifically concerning the effect of feedback on noise properties. These effects are of particular interest to amplifier designers attempting to optimize low-noise performance. Feedback and cascade networks also affect the measurement of noise parameters, and must be considered in the design of the experimental apparatus. Engberg [3.16] used T to π network conversions to deduce equations for the use of feedback to permit simultaneous input match and noise match; however, only lossless feedback elements were considered. Vendelin [3.4] employed the results of Hartmann and Strutt [3.14] to show the effect of lossless series and parallel feedback on a typical FET at microwave freqencies.

Iverson [3.17] investigated noisy series feedback, although his results are suspect. The author concluded that the calculation of the correlation coefficient between two voltage generators was overlooked. Additionally, Niclas [3.18] stated that his results do not agree with those of Iverson.

Niclas [3.18] used Y-parameters and a noise generator representation which allow for lossy parallel and series feedback. The solution was in terms of noise generators.

Haus and Adler [3.14] derived a new figure of merit for two-ports (particularly low noise amplifiers) called the noise measure, M, given by

$$M = \frac{F - 1}{1 - 1/G_a} , \qquad (3.63)$$

where M is the noise measure,

F is the noise figure,

G_a is the available gain.

One advantage of noise measure in quantifying amplifier performance is the inclusion of gain in the equation. Haus and Adler demonstrated that in a multi-stage amplifier, the stage with lowest noise measure, not noise figure, should be used as the input stage to minimize the overall noise measure.

The network effects described in this section are useful for evaluating the effects of non-ideal fixtures. Feedback and lossy networks can also be intentionally introduced to enhance DUT stability. However, the methods described above must then be used to de-embed the intrinsic DUT parameters.

Chapter 4

Measurement Apparatus

4.1 Introduction

This chapter begins by describing the arrangement of the apparatus inside the cryostat, explaining how the problems of both S-parameter and noise temperature calibration were solved. An overview of the systems external to the cryostat is then provided. This includes the S-parameter measurement system, and the noise figure meter, complete with the heterodyning scheme. The calibration standards constructed are also discussed.

The measurement system requires a variable impedance noise source, and this was realized using a mechanical tuner with a stepper motor drive. Details of both the tuner and the motor controller card are provided. Chapters 5 and 6 describe the results obtained using the apparatus, and suggest further refinements.

4.2 Cryogenic Equipment Configuration

This section describes in detail the apparatus which is contained inside the cryostat vacuum chamber. External equipment is shown only as functional blocks, to be explained fully in section 4.3.

Figure 4.1 shows a schematic representation of the apparatus contained in the cryostat. All equipment shown is attached to the cold plate. The heat shield is used only for heat sinking of the cables to external connections to

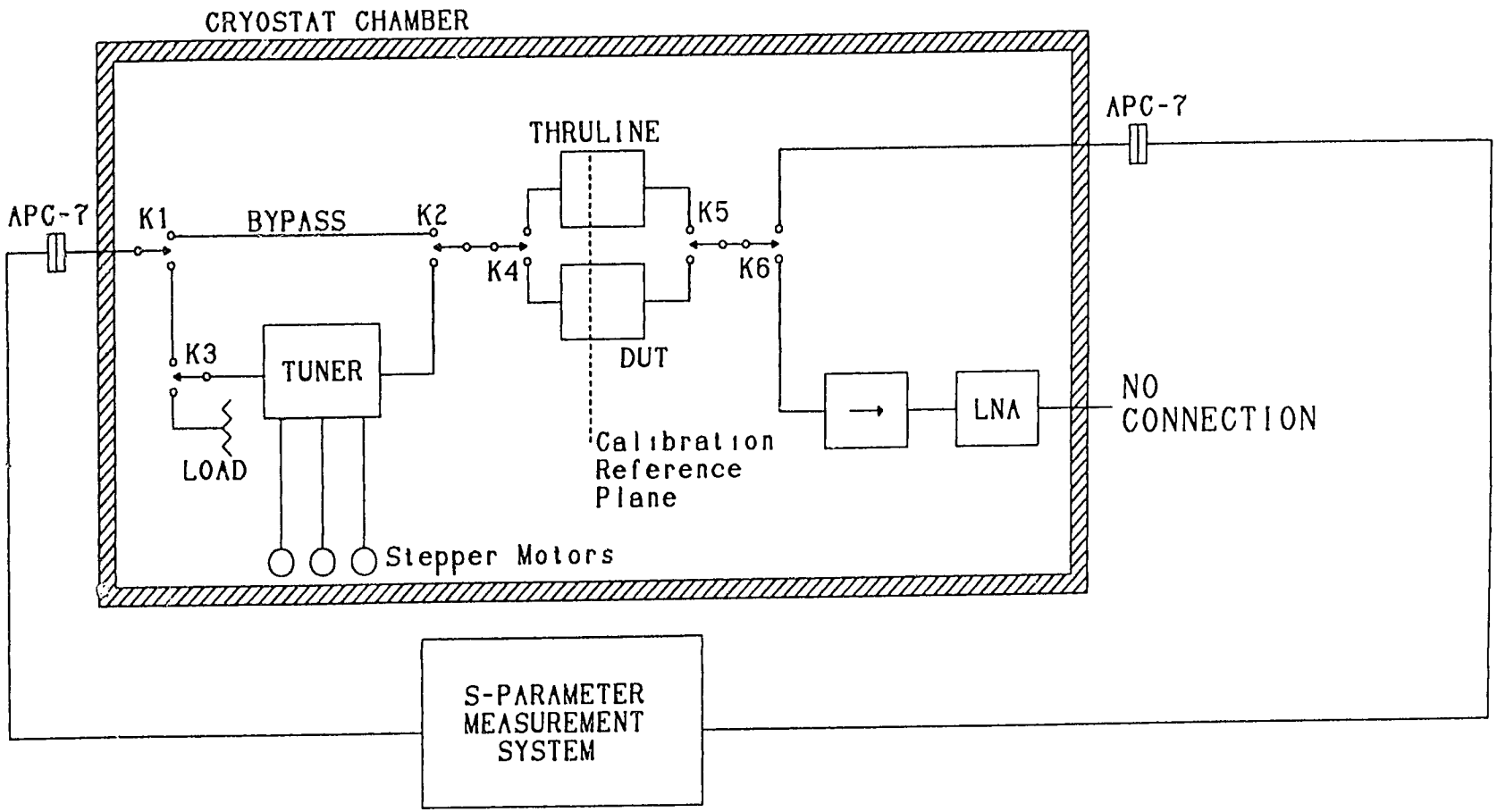

Figure 4.1: Schematic of the measurement apparatus interior to the cryostat. Exterior components for S-parameter measurement shown simplified.

reduce the thermal loading on the cold stage. Not shown are three temperature sensors, two on the cold stage and one on the heat shield, used for monitoring the performance of the cryogenic system and to obtain physical temperatures required by the noise parameter calibration scheme.

4.2.1 S-parameter Measurement

S-parameter measurements are made with relays K1 and K2 switched to the bypass line and K6 switched to the S-parameter test set (port 2). The position of K3 is irrelevant. The arrangement of K4, K5, the thruline fixture and the DUT fixture is critical to both S-parameter calibration and measurements of reflection coefficients dicussed later.

All relays in the cryostat are SMA coaxial latching types with both path lengths approximately equal. A test measurement using two SMA shorts revealed a phase difference of about 2° at 2.0 GHz. Test fixtures are made as nearly identical as possible, the only intentional variation being the stripline conductor geometry (eg. open, thruline, etc.).

The DUT and/or thruline fixtures are replaced by calibration fixtures. These consist of three offset open circuits and one thruline constructed in stripline as explained in a later section. S-parameter measurements are made from outside the cryostat through the noise source and reflection coefficient ports as shown in Figure 4.1. Obviously, the relays must be set to select the appropriate fixture and to bypass the tuner. The data is obtained after

the cryostat has cooled the equipment and thermal equilibrium has been reached. First tier calibration is accomplished using the existing "SPARAMS" program (OSLT method); this calibration is to the APC-7 interface shown in Figure 4.1. When an active device (eg. a transistor) is being measured, bias is supplied via networks internal to the HP8746A S-parameter test set.

DUT S-parameter measurement is done in a test fixture, and no fixture de-embedding or modelling is required as these effects are intrinsically removed by the second tier calibration. Bias, if required, is supplied through the measurement circuit from bias networks in the HP8746B S-parameter test set. Any effects of the bias networks are therefore removed as part of the first tier calibration.

The 3ST method described in chapter 2 is then used to obtain an eight error vector model for de-embedding the DUT. A full twelve error vector model is unnecessary because negligible feedthrough occurs in the cryogenic apparatus and because switching is performed only in the S-parameter test set. Switching effects are therefore already compensated for by the first tier calibration.

Theoretical values of the standards are found by calculations described later. The 3ST method is a two-port calibration scheme, so two reference planes can be defined inside the test fixture. This is useful for measurements of a two-port, such as a transistor or composite network, where it is convenient to consider the DUT as existing between the reference planes. For noise parameter measurements, the two

calibration planes are brought together at the plane to which Γ_{opt} is to be referenced. This permits easy calculation of the mismatch factors at the reference plane.

The second tier calibration information is also used to correct reflection coefficient measurements required when collecting noise parameter data. Using single port measurements, the reflection coefficient of the receiver (K6 set to isolator position) is measured and corrected to the reference plane shown. Similarly, the values of reflection coefficients of both bypass and tuner can be measured as required for noise source calibration and tuner loss compensation.

4.2.2 Noise Parameter Measurement

The block diagram of Figure 4.2 illustrates the cryogenic equipment connected to the external apparatus for noise parameter measurements. The reflectometer is one port of the S-parameter test system, and both tiers of calibration are reuseable for noise measurements. Suitable selection of the reference plane permits the value of Γ_T to be measured directly by the reflectometer, although de-embedding using the error vectors is needed. This permits direct measurement of the value of Γ_{opt} when a DUT noise temperature minimum has been reached by iteration.

When the DUT is an active device, new arrangements must be made to provide power as the S-parameter test set bias can no longer be used. Bias to the input of the DUT is supplied via a bias connection in the cryogenic tuner.

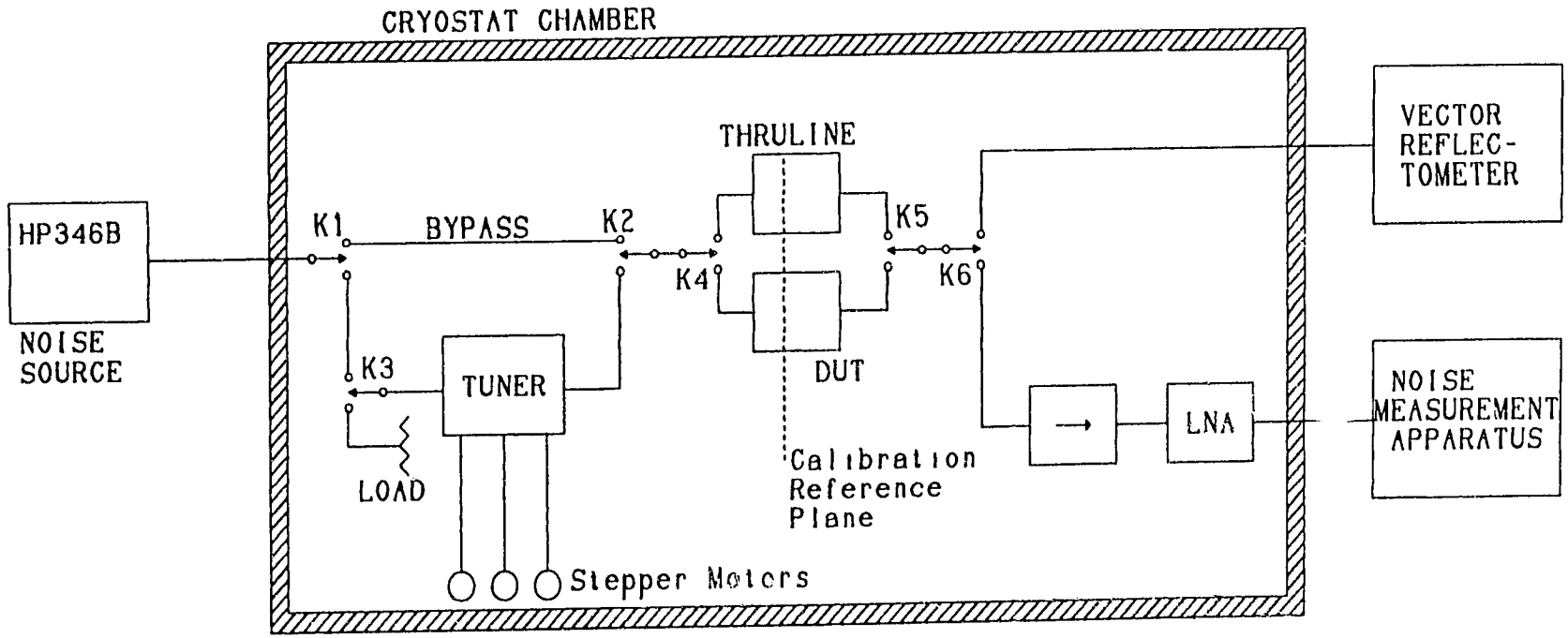

Figure 4.2: Schematic of the measurement apparatus interior to the cryostat. Exterior components for noise measurement shown simplified.

Bias blocking is also provided by the tuner to the opposite port. DUT output bias is supplied through the cryogenic isolator, specifically constructed to have DC continuity between the center conductors of the three ports while having no DC connection to ground. The removable cryogenic load used on the isolator is basically a coaxial structure with a lossy dielectric filling arranged to properly attenuate the microwave energy. The center conductor was left protruding from the end of the load, and a bias wire may be attached here. The LNA has an input capacitor which provides the required bias blocking.

The two-state noise source is connected from outside the cryostat because the HP346B used is not suitable for cryogenic operation. A Trak model 60A3001 isolator is placed at the output of the noise source to reduce changes in Γ_{NS}. Relays K1 and K2 provide a bypass around the tuner, and relay K3 applies a resistive load to the tuner input. This arrangement permits the use of the new calibration method described in section 3.6.3.

Remote operation of the cooled tuner is possible via a stepper motor drive system installed inside the vacuum housing of the cryostat. Details of both the tuner and the stepper drive arrangement follow in a later section.

The output of the DUT fixture can be switched to a Pamtech model CTE1193K isolator. This unit was procured specifically for this project, and is designed for cryogenic operation. It reduces the change in receiver noise contribution to the changes in noise temperature of the

isolator itself, although compensation for the variable available gain is still required. This error is most significant when measuring a DUT with low gain (eg. a passive DUT) and becomes less signifcant with increasing gain and/or unilateral characteristics of the DUT.

A cryogenic LNA provides gain to reduce the receiver noise temperature. The amplifier was fabricated following a design by Sando [4.1]. Room temperature measurements indicate a gain in excess of 20 dB and a noise temperature of 190K.

4.3 Measurement Apparatus External to the Cryostat

4.3.1 S-parameter Measurement Subsystem

The S-parameter subsystem used is an HP8410 system, modified to permit automatic measurement and error correction. A block diagram of the equipment and its interconnection is shown in Figure 4.3. When used with the noise measurement system, the DUT connections are made to APC-7 connectors at the cryostat ports.

The HP8746B S-parameter test set allows remote control of its internal RF attenuator settings, and this feature is used by the HP3421A data acquisition/control unit (DAC). IF attenuators in the HP8410A are manually operated in an unmodified system. A remotely controlled digital attenuator has been fitted to permit the DAC to control this function. The S-parameter data is displayed on a polar display, and the vertical and horizontal outputs have been low pass filtered before connection to the A/D inputs of the DAC.

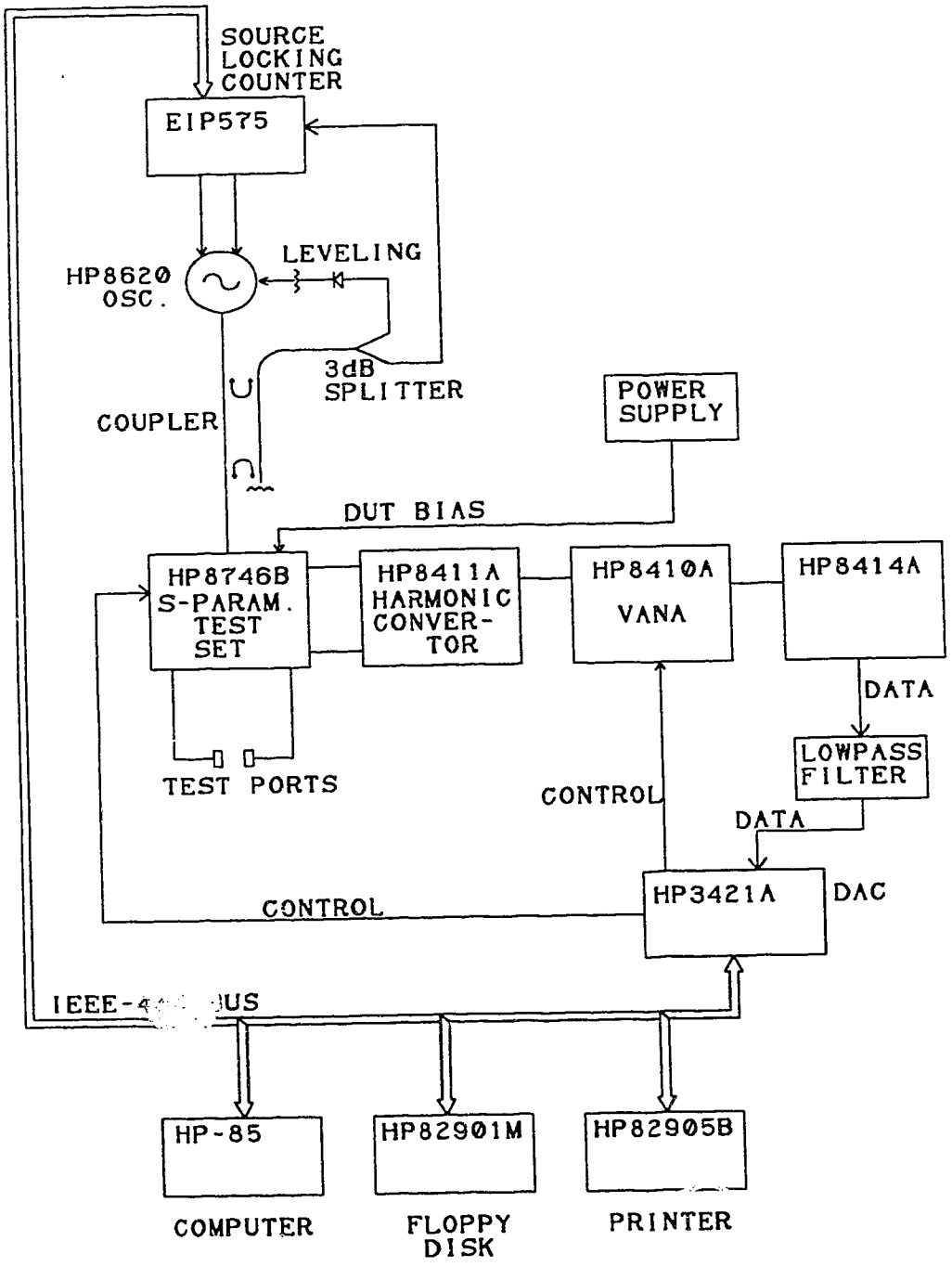

Figure 4.3: S-parameter measurement system.

Bias for an active DUT is connected from an external bias supply through the internal bias networks of the HP8746B, appearing on the center conductors of the APC-7 test connectors.

The measurement frequency is generated by an HP8620A oscillator, phase locked to an EIP-575 source locking microwave counter. The gain of the mixers in the HP8411A may vary if the RF power applied to the HP8746A changes. To minimize such instrument errors, a crystal detector is used to supply a leveling signal to the oscillator.

An HP-85 computer controls the entire system. A dual floppy disk drive is used for program and data storage. The current software uses the OSLT method of calibration to obtain a twelve error vector model for error removal. The software was recently modified to allow one-port measurements, with a significant improvement in speed over measuring the full four S-parameters. The IEEE-488 bus system used with the HP-85 is seperate from the HP-86 bus system used for the moise measurement system.

4.3.2 Noise Figure Measurement Subsystem

The noise figure measurement system provides accurate noise power measurements. The heart of the system is a HP8970A noise figure meter,as shown in Figure 4.4. The instrument cannot measure above 1.5 GHz, so an external heterodyning scheme is needed for 4.0 GHz experiments.

The 4.0 GHz noise signal from the cryogenic LNA is low-pass filtered by a filter with a cutoff frequency of

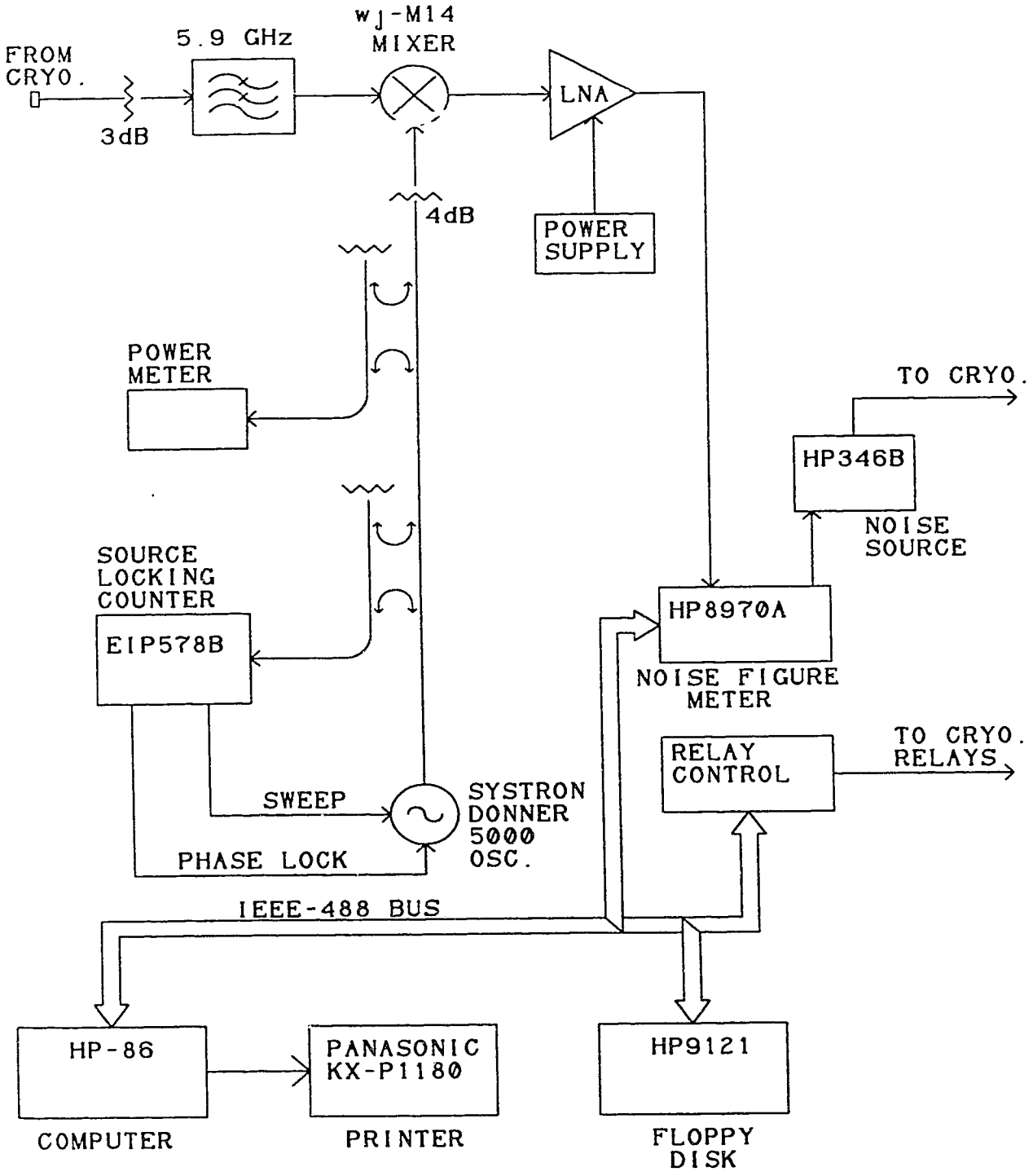

Figure 4.4: Noise parameter measurement system.

5.9 GHz. With a local oscillator frequency of 5.25 GHz, the image at 6.5 GHz is above the filter cutoff frequency. The 3 dB attenuator before the filter stabilizes the cryogenic LNA, which was otherwise unstable in some cases. A Watkins-Johnson type M14 mixer is used to downconvert the signal to the HP8970A input frequency. A 1.4 GHz LNA is used to amplify the signal entering the noise figure meter; without the LNA it is found that this instrument operates at its most sensitive internal attenuator settings.

The local oscillator frequency must be kept stable, and this is accomplished using an EIP-578B source locking counter to phase lock the oscillator. A directional coupler provides feedback to the counter, and 4 dB of attenuation is used to reduce the drive level to the mixer to about +7 dBm.

Power to the HP346B noise source is provided from the noise figure meter. The state of the source is determined by the bus commands from the HP-86 control computer. the computer also operates the relays inside the cryostat via the relay controller card.

The noise measurement software written by the author implements the new noise calibration method described in chapter 3. This includes reflection coefficient de-embedding using the second-tier error vectors. Mismatch factors, noise temperature equivalents, etc. are computed based on the reflection coefficient data which is manually entered and noise power measurements which are obtained automatically from the noise figure meter. Additionally, provision is made for manual setting of the relays in the

cryostat for S-parameter measurements or test purposes.

4.3.3 Motor Drive Subsystem

Adjustment of the cryogenic tuner is performed by remote operation of the drive stepper motors. The motors are mounted inside the cryostat vacuum housing, but electrical drive and control circuits remain outside. Each of the three motors has an associated controller card and drive module; details of these are provided in section 4.6. A commercial, general purpose supply powers the driver modules.

The motor control cards were constructed with features permitting field feedback of position, limiting of mechanism travel, and remote control via a IEEE-488 bus. These facilities were intended to allow automated searching for the minimum noise tuning, though this has not yet been achieved (see chapters 5 and 6).

4.4 Calibration and Test Fixtures

The calibration procedures described previously require repeatable and accurate standards. A set of such standards, suitable for cryogenic operation, was built in stripline. A successful fixture design already in use was modified slightly, to obtain the final design. Figure 4.5 shows an isometric view of the assembled basic fixture. Complete construction drawings are provided in Figure 4.6.

Stripline construction is realized using Duroid 5870 material with the appropriate circuit patterns etched and

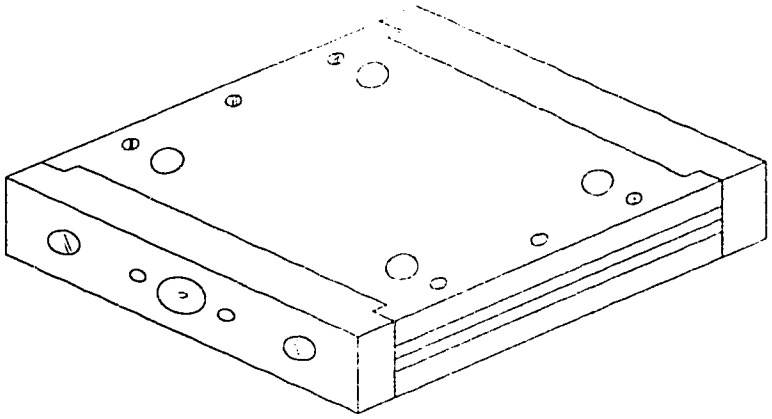

Figure 4.5: Isometric drawing of assembled test fixture.

gold plated. The ground plane copper foil is removed entirely; the top and bottom fixture parts are used as ground planes to eliminate ground contact problems.

The end plates are beveled to ensure that contact occurs between the end plate and the top and bottom plates without introducing unwanted parasitic elements. Similarly, there is a raised ring on the outer surface of the end plate to ensure proper contact with the ground conductor of the SMA connector.

No solder is used in the fixtures. The connector tab makes contact with the center conductor under pressure from the top and bottom plates. The fastener arrangement used to assemble the fixture permits pressure to be exerted both between top and bottom plates and between this assembly and the end plates.

The various fixtures are identical except for the conductor pattern on the Duroid. The four different patterns are shown in Figure 4.7. Duroid type 5870 microwave laminate, of thickness 0.0625 inches and with a

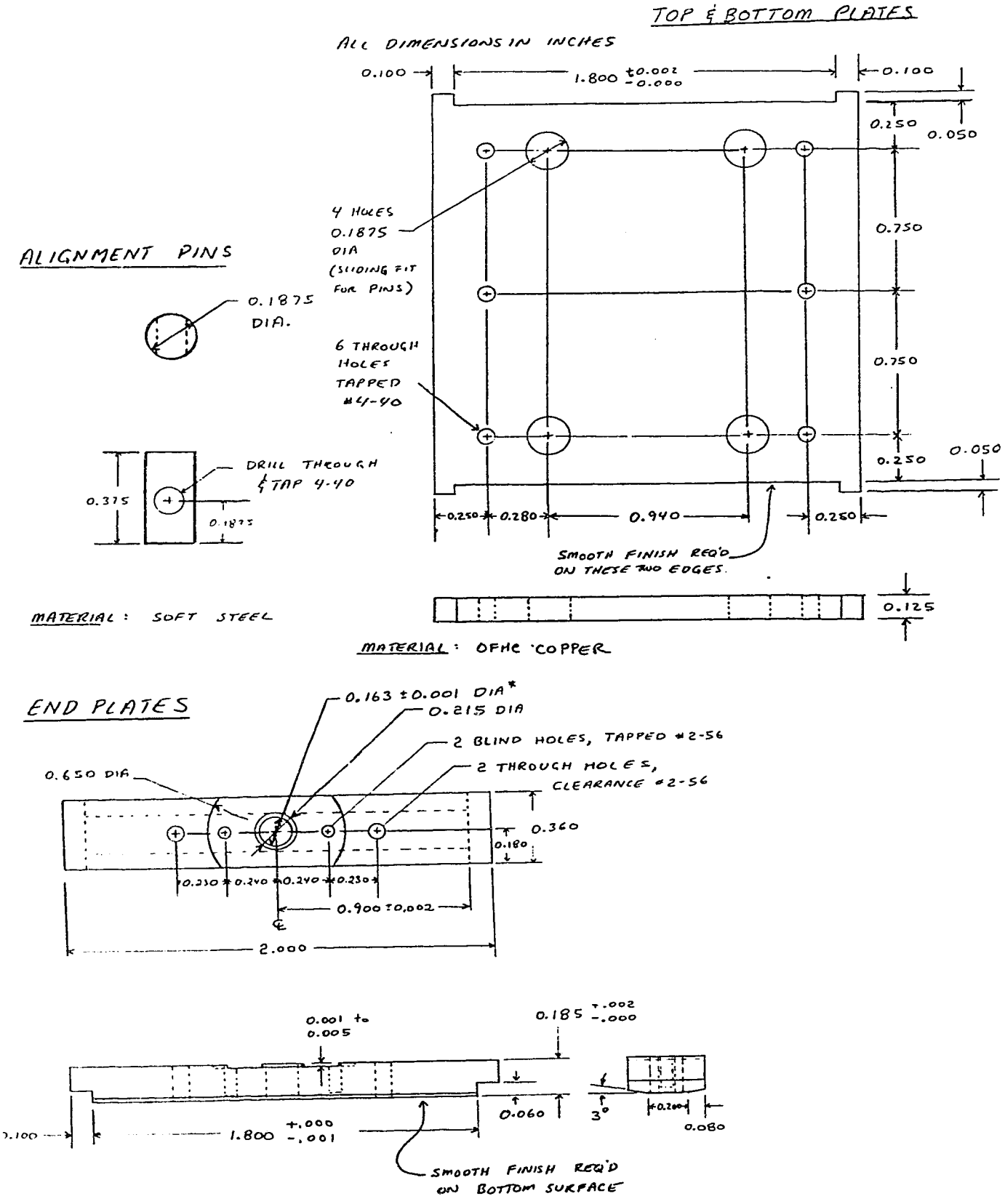

Figure 4.6: Detailed drawings of test fixture components.

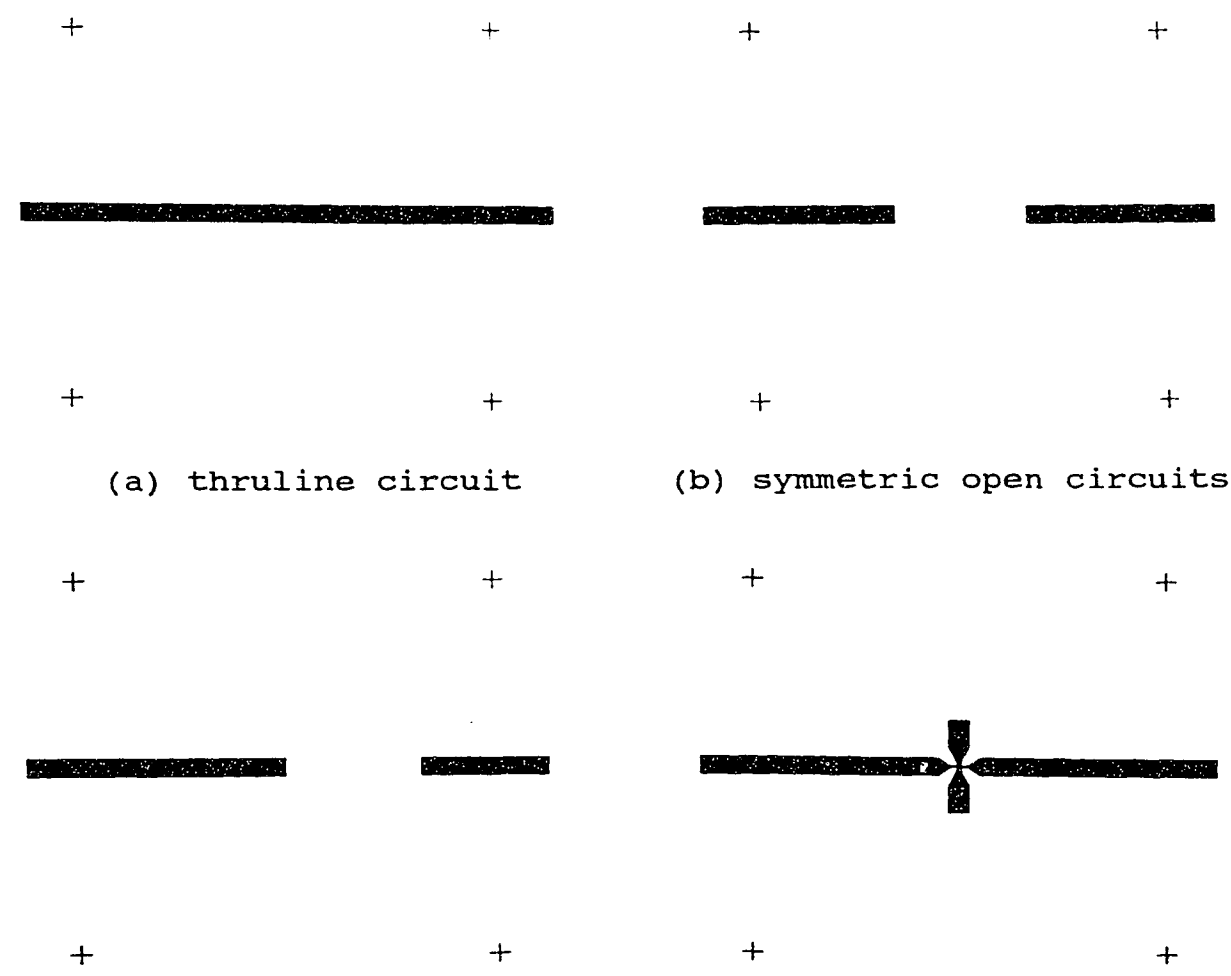

Figure 4.7: Stripline conductor patterns. Note the reproduction process used for this thesis causes the false appearance of a short circuit in (d) above.

dielectric constant of 2.33, is used. The conductor width is 0.100 inches, which corresponds to a characteristic impedance of 50 ohms in this material. The two offset open fixtures correspond to Figures 4.7(b) and (c). The difference in length is selected to be 60° at 4.0 GHz; only

two fixtures are used since the asymmetric unit can be reversed to serve as two standards for both ports.

A fourth fixture provides a mounting region for a chip or packaged transistor. The conductor pattern, shown in Figure 4.7(d), is similar to a commercial mounting package. A packaged device can also be accommodated by carefully placing it above the center of the pattern, and ensuring that no shorts occur. In either case a recess is drilled into the top dielectric piece to clear the transistor. A passive DUT can be made by bridging the gap with a resistor, and placing conductive tuning strips where necessary to achieve the desired S-parameters.

Source lead connections to ground consist of two gold plated blocks with shimstock protruding from one end (see Figure 4.8). The blocks are slightly smaller than the groundplane spacing, so that the final contact can be made by corrugated shimstock (also gold plated) which provide a spring contact suitable for cryogenic use.

The theoretical reflection coefficient value of each open circuit is calculated by a FORTRAN subroutine.

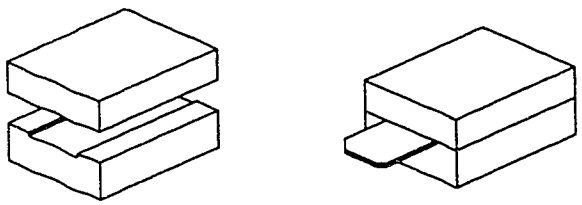

Figure 4.8: Source lead shorting blocks

Fringing capacitance causes the open circuit to be effectively extended past the physical end of the stripline by an amount $\Delta\ell$ [4.2]:

$$\Delta\ell = \frac{1}{\beta}\left\{\frac{\delta + 2w}{4\delta + 2w}\tan(\beta\delta)\right\} \qquad (4.1)$$

where $\beta = \frac{2\pi}{\lambda}$,

λ = wavelength in stripline,

$\delta = \frac{b \ln 2}{\pi}$,

b = ground plane spacing,

w = width of stripline conductor.

This offset is calculated, and the effective distance between the reference plane and the open circuit is computed. The theoretical reflection coefficient is then calculated using the relation:

$$\Gamma = \cos\left(\frac{4\pi\ell}{\lambda}\right) - j\sin\left(\frac{4\pi\ell}{\lambda}\right) \qquad (4.2)$$

where ℓ is the computed distance from the reference plane to the effective open circuit.

This procedure permits calculation by subroutine of the standard's reflection coefficient Γ using the stripline dimensional data, the reference plane location and the frequency.

4.5 Cryogenic Tuner

A cryogenic, remotely controlled tuner provides a variable input impedance to the DUT. The complexity of placing the tuner inside the cryostat was justified by two considerations. First, and most important, it permits the use of the new noise temperature calibration scheme

described in section 3.6. Second, a tuner with a shorter cable length to the DUT exhibits less phase shift with frequency at the DUT input. This characteristic is desirable to help increase DUT stability when potentially unstable devices are tested.

The tuner is built to meet the following design criteria:

1. It must operate properly in a cryogenic environment.
2. It must be passive for noise calibration purposes.
3. It must present a thermal load which the cryostat can accommodate.
4. It should include a DC block and bias supply connection.
5. Its physical size must permit both tuner and other apparatus to be placed in the cryostat.

Emphasis was placed on ensuring that the tuner would operate properly inside the cryostat. A tuner which cannot be adjusted once cooled is of little value, regardless of its other merits. Moving contacts are undesirable, so the design instead uses moving dielectrics. A non-contacting short is a possible alternative, but was not used since an adequate design was obtained without such added complexity.

Figure 4.9 shows the basic tuner configuration. Teflon cylinders move over the stub center conductors to alter the electrical length from the open circuit to the main center conductor. In this manner, tuning is achieved without electrical contacts. A three stub design was chosen, with 3/8 wavelength stub spacing. The stub spacing was based

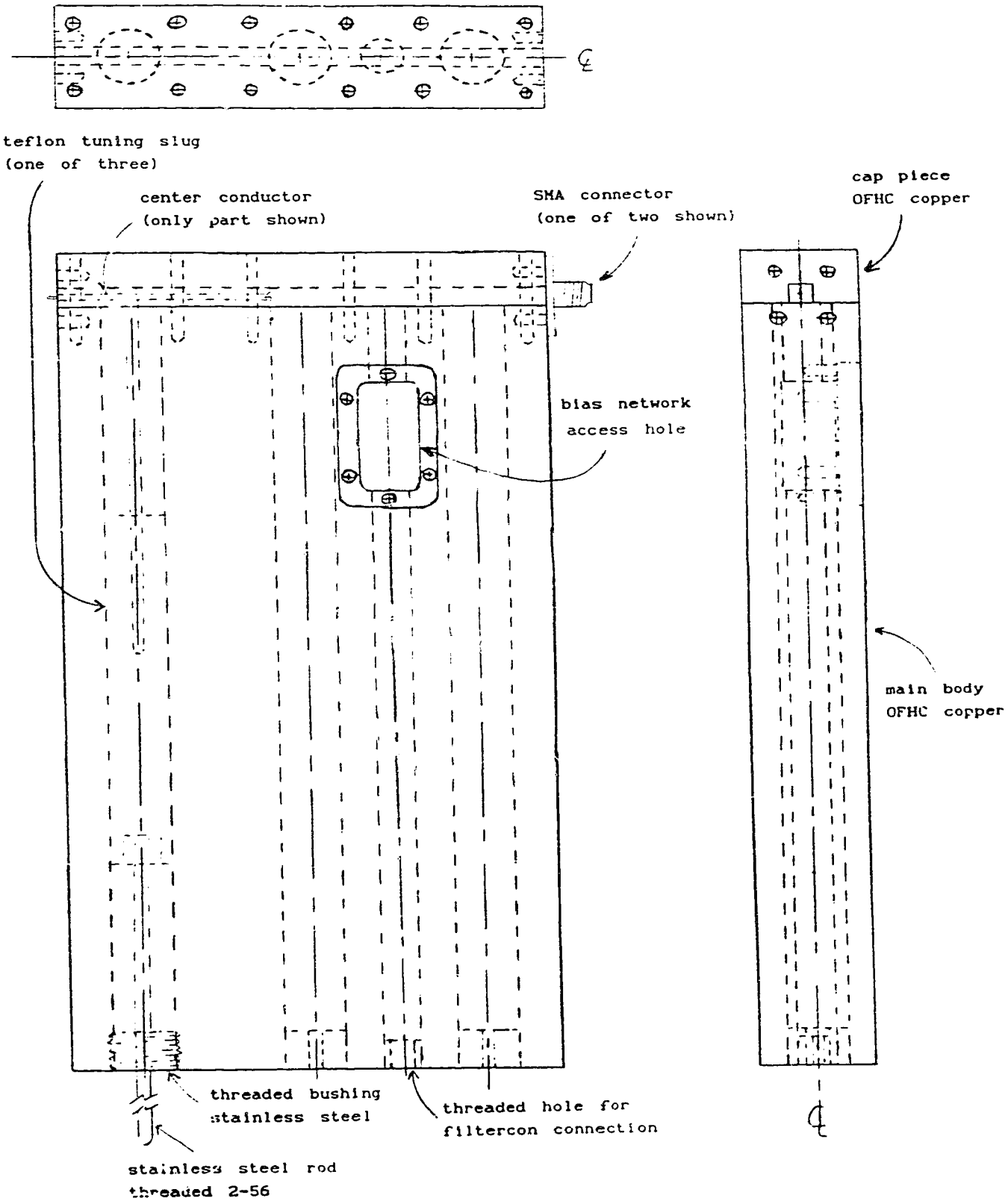

Figure 4.9: Cryogenic tuner mechanical drawing (approximately full size)

upon the minimum practical spacing of the stepper motor drive shafts. A stub length (and the teflon slug length) of 64 mm was found to provide adequate tuning range, while remaining sufficiently small to be placed inside the cryostat.

The main coaxial line, to which the three tuning stubs attach, has 50 ohm impedance to match the transmission lines in the remainder of the test system. This line is implemented in square slab-line, with characteristic impedance given by [4.3]

$$Z_0 = \frac{1}{\sqrt{\varepsilon_R}} 59.952 \ln\left(\frac{1.0787\ b}{d}\right) \quad \text{ohms} \qquad (4.3)$$

where b and d are dimensions as shown in Figure 4.10, and ε_R is the dielectric constant of the medium (in this case, air or vacuum) inside the slab-line.

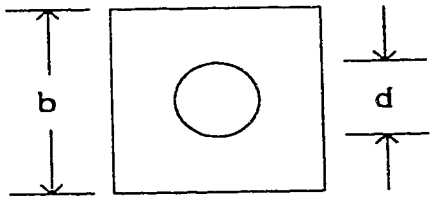

Figure 4.10: Square slab-line geometry

The tuning stubs use a circular coaxial configuration, with characteristic impedance of [4.4]

$$Z_0 = \frac{1}{\sqrt{\varepsilon_R}} 59.952 \ln\left(\frac{b}{d}\right) \quad \text{ohms,} \qquad (4.4)$$

where b is the inside diameter of the outer conductor and d is the outside diameter of the inner conductor. The

impedance of the stubs was selected to be 110 ohms with air (or vacuum) dielectric. This larger value permits the teflon tuning slugs to be made larger (10 mm diameter) and therefore more robust. The attachment of a bigger slug to the threaded stainless steel drive rod is also easier.

Before proceeding with the mechanical construction details, the electrical performance of the tuner was estimated. The effects of parasitics and losses were ignored, so the results are not completely accurate. Stubs are assumed to be 64 mm long, with 28 mm spacing between stubs and 12 mm line length at each end to the connectors.

The estimated tuning range of this arrangement was computed graphically on a Smith Chart. Figure 4.11 shows the output admittance range obtained when a matched load is placed at the tuner input. This rough calculation was repeated using a FORTRAN program written by the author. The program assumes 64 mm stub lengths and computes the tuner output reflection coefficient for each position of each of the three stubs in 8 mm increments. Parasitic effects and losses are ignored. The data points thus obtained are plotted in Figure 4.12. The result shows an acceptable spread of points and there is reasonable agreement with the previous Smith Chart estimate.

This tuning range was considered acceptable, although it did not cover the entire Smith Chart. Increases in physical size or mechanical complexity would likely be required to achieve greater tuning range.

The tuner body (see Figure 4.9) is constructed of two

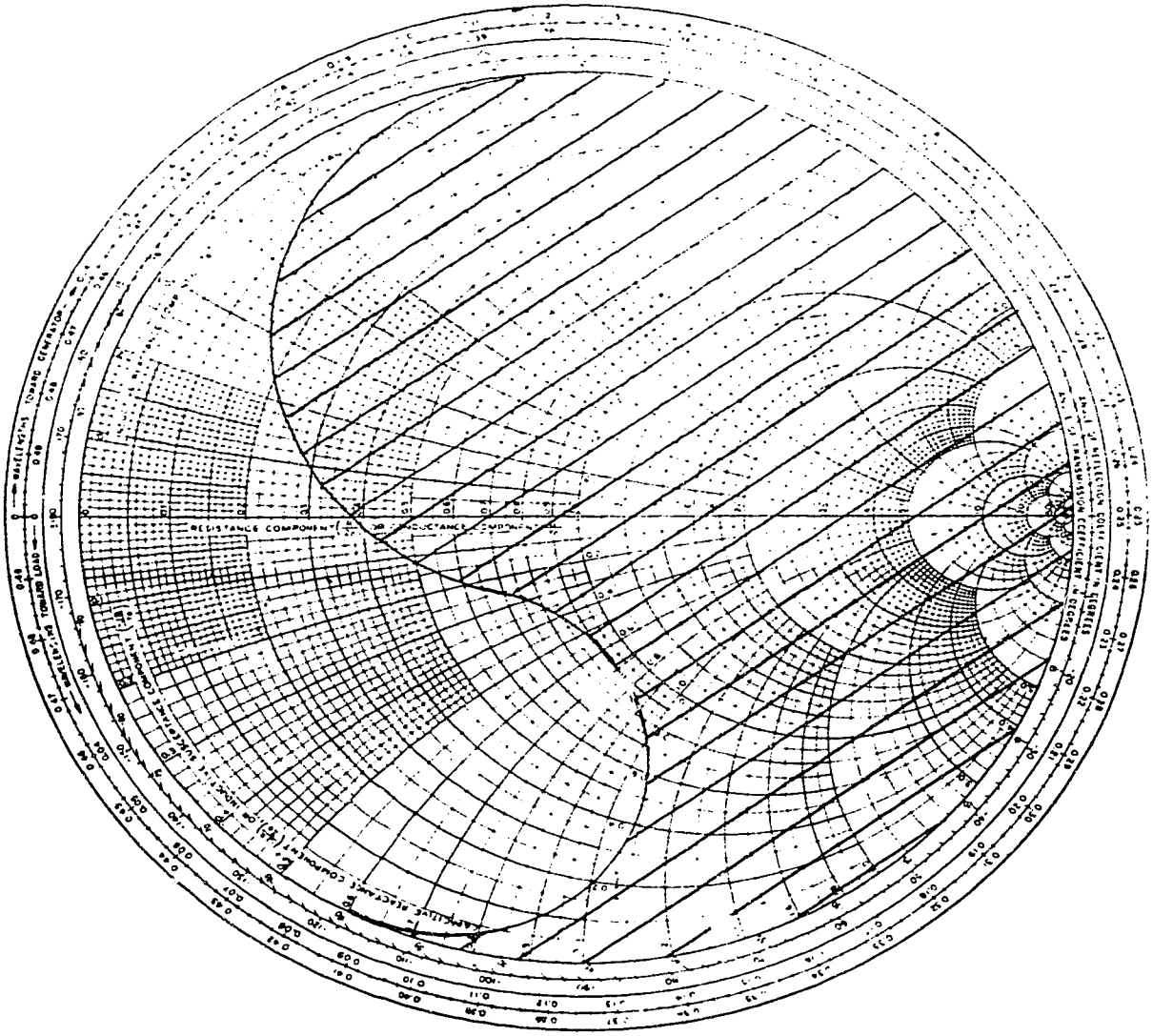

Figure 4.11: Smith Chart calculation of the tuner range.

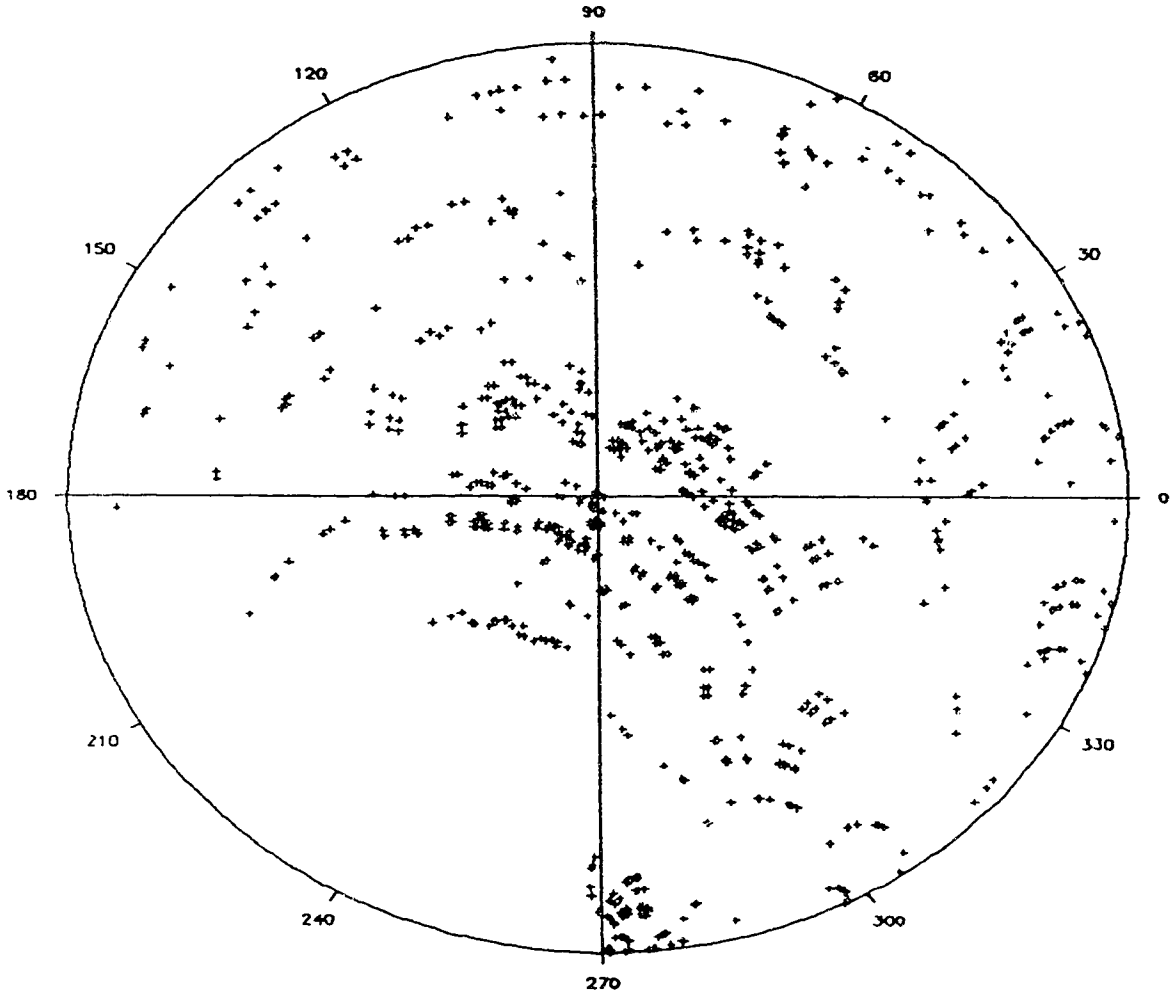

Figure 4.12: Tuner range estimated by numerical computation.

pieces of oxygen free high conductivity (OFHC) copper. The main section consists of a single copper block, with three 10 mm holes reamed to final size for a smooth finish. The cap piece is made with a square channel which forms the outer conductor of the square slab-line.

A fourth hole drilled between two of the stubs accommodates a bias network. A machined cavity permits soldering a bypass capacitor to ground, at a distance of one quarter wavelength (at 4.0 GHz) from the main center conductor. The bypass capacitor value chosen provides series resonance with its parasitic inductance, thereby producing a low impedance to ground. An additional bypass network consisting of a series inductance (wire with a single turn around a ferrite bead) and a shunt capacitor follows. Final connection of the bias wire is to a "filtercon" terminal between two of the tuning rods. This location is desirable, since this side of the tuner must be unobstructed for the motor drive connections.

Linear motion of the teflon tuning slugs is accomplished by rotating the entire slug/drive rod assembly. The threaded drive rod passes through a tapped bushing at the tuner body entrance, and this converts the rotary motion to translational motion of the tuning slug. Both the bushing and the drive rod are made of stainless steel to minimize differential expansion between the male and female threads, which might cause excess friction or seizing of the mechanism. Stainless steel was selected for both strength and low thermal conductivity, to reduce the heat load due to

thermal conduction along the rods.

Some form of sliding rotary coupling was then needed between the drive rods and the fixed stepper motors. The motor shafts were rigidly connected to lengths of square brass tubing, with the original intention of attaching a matching square fitting on the tuner drive rod. As an "interim" measure during testing, two 2-56 nuts were placed on the end of each drive rod and jammed together. Two opposing vertices of the hexagonal nuts were filed off until the nuts would slide inside the square tubing, but still transmit the required rotary motion. This "temporary" solution never failed, and is retained in its initial form.

The stepper motors are mounted on an aluminum plate which is fastened to the outside cryostat wall. A suitable opening in the 77K heat shield is needed to clear the drive assemblies. Control of the motors from outside the cryostat uses a motor controller card, described in the following section.

Experimental experience with the tuner has been favourable. No mechanical problems have been encountered with the tuner or its drive mechanism. Tuner range is less than predicted, and this appears to be caused by losses and/or parasitics not considered in the original range estimate.

4.6 Stepper Motor Controller

This section describes a stepper motor controller card built to satisfy the requirements of remote adjustment as

described previously. Although built to operate a three stub tuner, the design has been kept sufficiently general that other uses are possible. Both manual and remote operation (via IEEE-488 interface) are possible, and provisions have been made for field position feedback and "limit switch" restriction of mechanical travel. A section explaining the basics of stepper motor operation has been included. This provides a minimum of information required to explain the operation of the driver card. Finally, the design and operational details of the controller card are presented.

4.6.1 Stepper Motor Fundamentals

Stepper motors are a type of electromechanical machine in which, as the name suggests, motion occurs in discrete increments, or "steps". A number of variations exist; this discussion does not attempt to provide more than a limited insight into these devices. Additional information is available in numerous references; reference [4.5] is a good starting point.

This section is intended to provide the user with the minimum knowledge required to understand the principles of operation and electrical drive requirements of various types of stepper motors. The controller card will only operate two-phase permanent magnet motors. The user should ensure compatibility of the motor, drive circuit, and controller card.

4.6.1.1 Variable Reluctance Motors

The variable reluctance (VR) motor consists of a rotor mounted within a stator on which the motor windings are supported. Salient pole construction is employed for both the rotor and stator, as shown in Figure 4.13. No windings are required on the rotor, thereby eliminating the need for any type of brush gear. Windings on the stator are connected between opposite poles. Operation of the motor is described below.

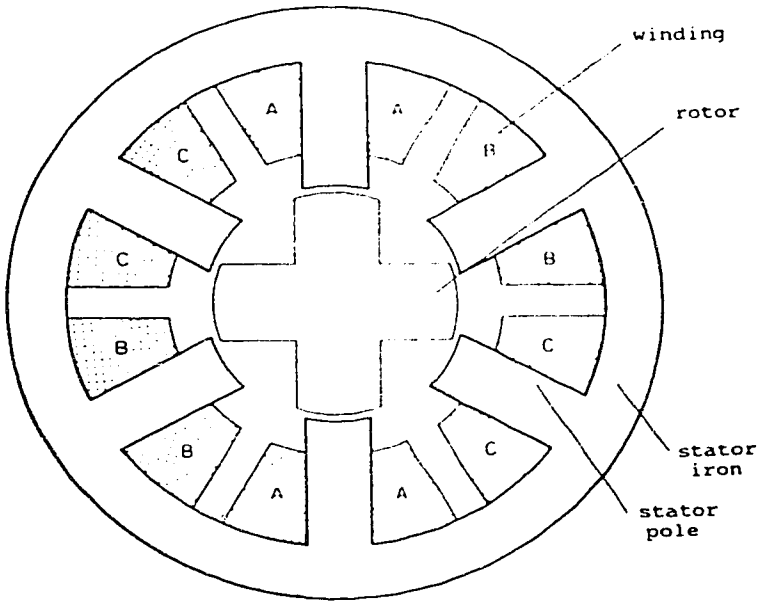

Figure 4.13: A three phase variable reluctance motor (Modified from Acarnley [4.5])

The rotor will attempt to align one set of poles with an energized stator winding, thereby minimizing the magnetic circuit reluctance. This principle is used to lock the rotor in a fixed position. The intrinsic ability to produce a torque acting to keep the rotor stationary contrasts

greatly with other types of AC or DC machines, where a servo-feedback mechanism is required to achieve this effect.

Typical operation of a 3 phase VR motor is shown in Figure 4.14. Windings A, B, and C are each energized in sequence, and the rotor moves counterclockwise in increments to maintain a minimum reluctance position. This is the opposite of induction motors, where the rotor motion follows the phase sequence. Reversing the direction of motor rotation is accomplished by reversing the phase sequence of the drive circuit. Motor speed is proportional to the rate (frequency) of the phase changes. However, the output torque of the motor is limited, and loss of synchronization with the driving supply is possible. Accelerating torque, rotor inertia, load inertia and other factors place limits on variable speed (and direction) drives. Loads having a torsional resonance near the stepping frequency are prone to excitation by the pulsating torque, and require careful design. The dynamics of stepper motor control are complex, and are not discussed further here.

Stepper motors with small angular step size (eg. 1.8°) are achieved using multiple teeth on each pole face. Figure 4.15 illustrates such a machine. A "stack" type of construction can be used, where each phase has a stator section complete with windings; these sections are then stacked together to form the complete motor stator.

Variable reluctance motors are available with varying numbers of poles and electrical drive requirements. Three, four and six phase VR motors are available. Drive and

control circuits must be designed to match the particular type of motor utilized.

4.6.1.2 Permanent Magnet Motors

The permanent magnet (PM) stepper motor is in many respects similar to the VR motor described previously. As the name suggests, however, the rotor structure is now fabricated using a permanent magnet. The magnet of the rotor structure will align with the magnetic field produced by the stator winding current, thereby achieving the desired incremental rotor motion. Unlike the VR motor, the rotor is influenced by the direction of the current flow through the stator winding; consequently bidirectional drive circuits are required for PM motors.

Figure 4.16 depicts the operation of a typical 2 phase PM motor. Although only two phases are used, the drive circuit must now be able to reverse the direction of the phase current. Since this type of motor was used, details of the drive circuits constructed are discussed in the circuit description section.

4.6.2 Stepper Control Card Circuit

4.6.2.1 Controller Design Description

Any project usually requires that some engineering decisions and compromises be made. This section details the objectives and design of the controller card.

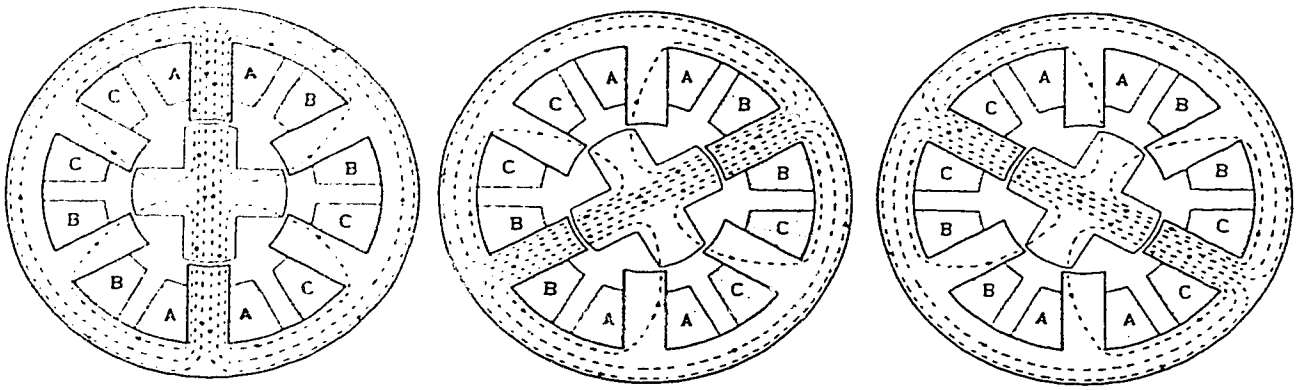

Figure 4.14: Operation of a three phase VR motor (Modified from Acarnley [4.5])

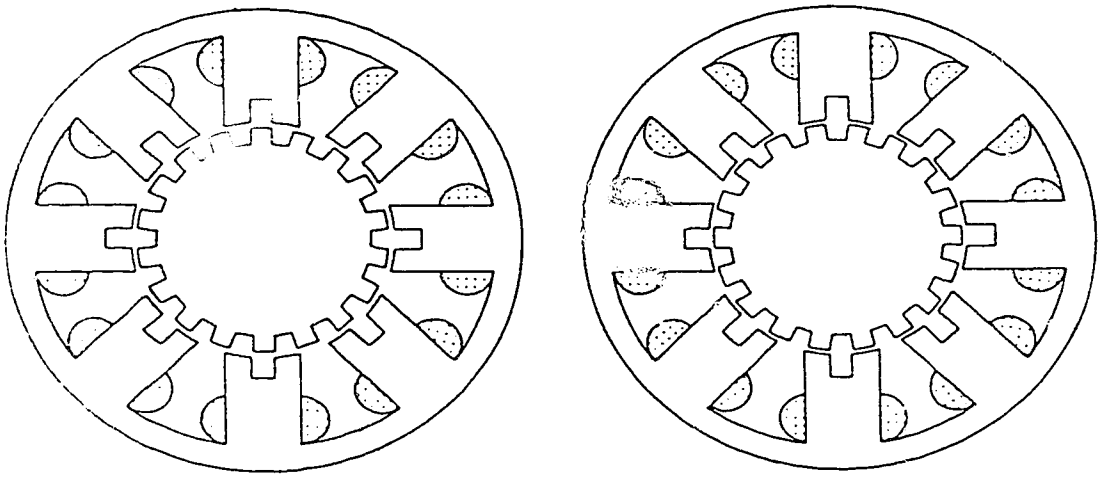

Figure 4.15: A hybrid motor with small angular step size. Both stacks of a two stack motor are shown. (Modified from Acarnley [4.5])

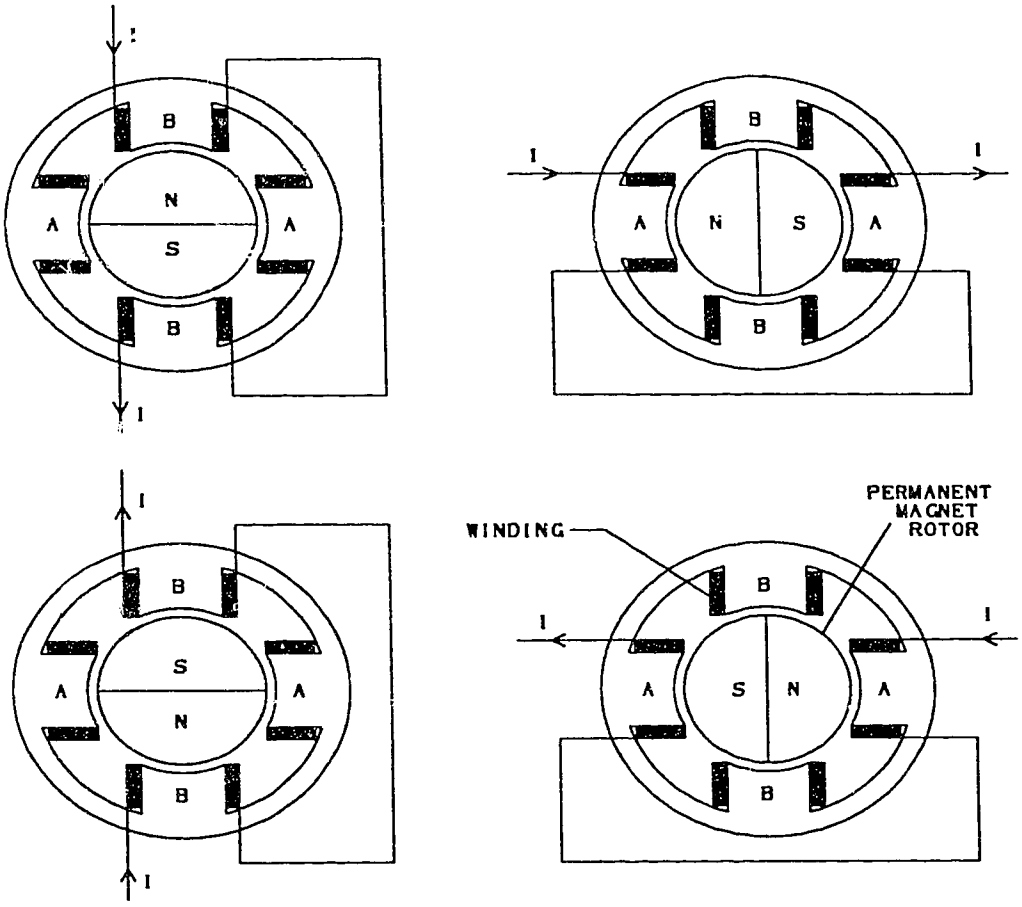

Figure 4.16: Operation of a permanent magnet stepper motor showing use of bidirectional winding current drive.

The controller card fulfills the following requirements.

1. It drives small, inexpensive 2 phase PM stepper motors.
2. It uses existing IEEE-488 cards to provide computer control of the motor, thereby reducing cost and complexity.
3. Manual control is provided via front-panel switches.
4. Position feedback from an index hole (or similar feedback feature) is possible.
5. It accepts inputs from "limit switches" to restrict the range of mechanical travel.
6. The motor can be run continuously at a fixed speed, or single stepped, in either direction.

The controller was designed to meet the above criteria as simply and inexpensively as possible. The radio astronomy group has previously constructed VME bus cabinets with compatible IEEE-488 interface cards (ref. [4.6]). The controller cards plug into these cabinets, using the IEEE-488 cards to provide the necessary interface to a system control computer (eg. HP-86). Driver circuits for the stepper motor are not provided as part of the controller card in order to provide the flexibility to use different stepper motors by changing the driver circuit, and to eliminate heat dissipation (mostly from forcing resistors) from the VME bus cabinet. The internal power supply would also be adequate for only very small motors.

4.6.2.2 Functional Description

Most of the controller is implemented on a 100 x 160 mm "europac" card. Two smaller boards are also used: one is a piggybacked counter board to provide the output for an LED display, and the second is a board to support the LED display itself. Each controller card interfaces to one motor only; however, multiple cards (8 maximum) can be used with the same IEEE-488 module. The IEEE-488 interface modules are existing units, which are described in reference [4.6].

Figure 4.17 illustrates a block diagram of the controller board. Inputs from the IEEE-488 board provide a motor selection address and STEP, RUN and DIRECTION control lines. A front panel switch selects either remote or manual operation; these functions are mutually exclusive. Motor rotation is selected with the DIRECTION control, the RUN control runs the motor continually, and the STEP control advances the motor one complete step for each command. Only one card (and therefore one motor) can be selected for operation by the IEEE-488 module. Manual operation is independent of this instrument bus, and this single motor restriction does not apply. No IEEE-488 card is required if only manual control is desired.

The synchronizing circuit ensures that step and run commands are synchronized to the free running clock, and integral step driving is ensured. One exception to this is if the direction is reversed while running, it is then possible to generate partial clock pulses to the motor

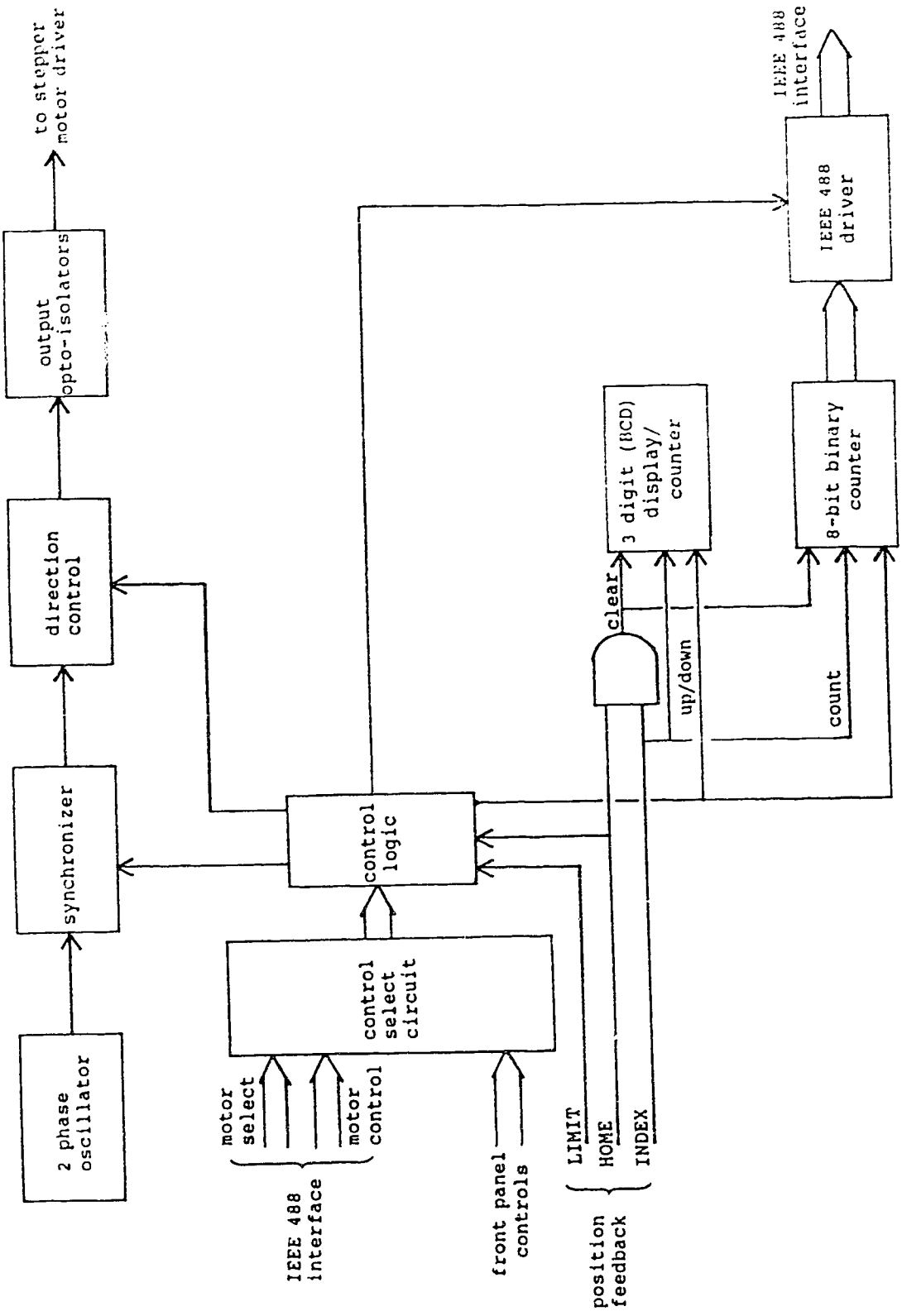

Figure 4.17: Block diagram of the stepper motor controller card.

driver. Therefore, the motor should be stopped before the direction is changed. Failing to observe this precaution should not damage the motor or driver circuit, when load inertia is small.

Two counters provide an indication of the mechanism position by counting the number of index hole pulses received from some sensor, for example, a rotating disk with an index hole. Separate counter circuits were used for an LED display on the controller card, and a binary counter which can be read by the control computer using the interface card.

The BCD counters and LED drivers are mounted on a piggyback card to provide local indication of the position counter. A greater range is available (0-999) than with the IEEE bus counter (0-255).

Another important design consideration was the range of the counters. The immediate application to a 3-stub tuner required about 135 turns (ie. counts), and this resulted in the selection of an 8-bit counter (3 decades for local indication). The added hardware complexity of implementing a multiple byte bus transfer did not seem justified. If the motor is controlled only by the computer, "wrap around" beyond the 255 count limit should be accommodated in software by the user.

The controller card also accepts "limit switch" inputs, denoted HOME and LIMIT. The HOME signal acts as a reference position for the mechanism, and the count is reset to zero in this position. The LIMIT signal would normally be used

to restrict the range of travel, to prevent damage to the mechanism. Both the HOME and LIMIT signals can be programmed (via jumpers) to inhibit further motion when either limit is reached. The initial configuration of the patch region (J12) is given in Appendix II, and a table of integrated circuit functions is provided in Appendix III. Appendix IV contains a summary of the available IEEE-488 instructions for remote operation of the card.

4.6.2.3 Detailed Circuit Description

Circuit details are discussed in this section to expand upon the previous functional description. The schematic diagram, Figure 4.18, is referenced throughout this section. Circuit board component and jumper locations are given in Figure 4.19.

A 555 oscillator produces the clock pulses for the motor drive section. U4 (a dual JK flip flop) forms a two bit walking ring counter [4.7] which generates the basic two phase motor driving signal, with the signals 90 degrees out of phase, and with a 50% duty cycle. The 555 oscillator is free running and continuously clocks the walking ring counter.

U3, a dual D-type flip flop acts as a one-and-only-one synchronizer [4.8]. An asynchronous high-to-low transition on pin 4 permits the next complete motor step cycle to be gated through U5a and U5b NAND gates. The remainder of U5 and U6 is used to select the direction of motor rotation by interchanging lines during their low state, so that the

switching does not produce undesired motor movement. Opto-couplers U13 through U16 make the two-phase drive signals ϕ_1 and ϕ_2 and their complements $\bar{\phi}_1$ and $\bar{\phi}_2$ available to the external stepper driver transistors. This allows for easy biasing of the driver transistors, while simultaneously isolating the VME cabinet electronics from the motor power supplies.

U18 is a data selector used to switch between the remote and manual control signals. A schmitt trigger and a low-pass R-C network debounce the manual step pushbutton to prevent retriggering the synchronizer. In manual mode, the SEL (select) line permitting the motor to run is held at +5V by U18 to permit operation from the front panel switches even when the card is not enabled by the IEEE-488 select lines.

Jumpers J1 through J3 (see Appendix V) set the controller card address, which is decoded by U10a, b, d and U9c, to yield the card select line denoted SEL. This signal is used to enable the tri-state outputs so that the position counter can be read via the IEEE bus, even when the card is in manual mode. The SEL signal (inverted by U10c) is switched by U18, and used to permit motor operation when the card is selected and in remote mode. U2 is used to inhibit operation when the switched select line is low. The resistor-capacitor network between U2c and U2a produces a short pulse to trigger a single step from the synchronizer when the output of U2c makes a high to low transition. U9a inhibits triggering of the one-and-only-one circuit if

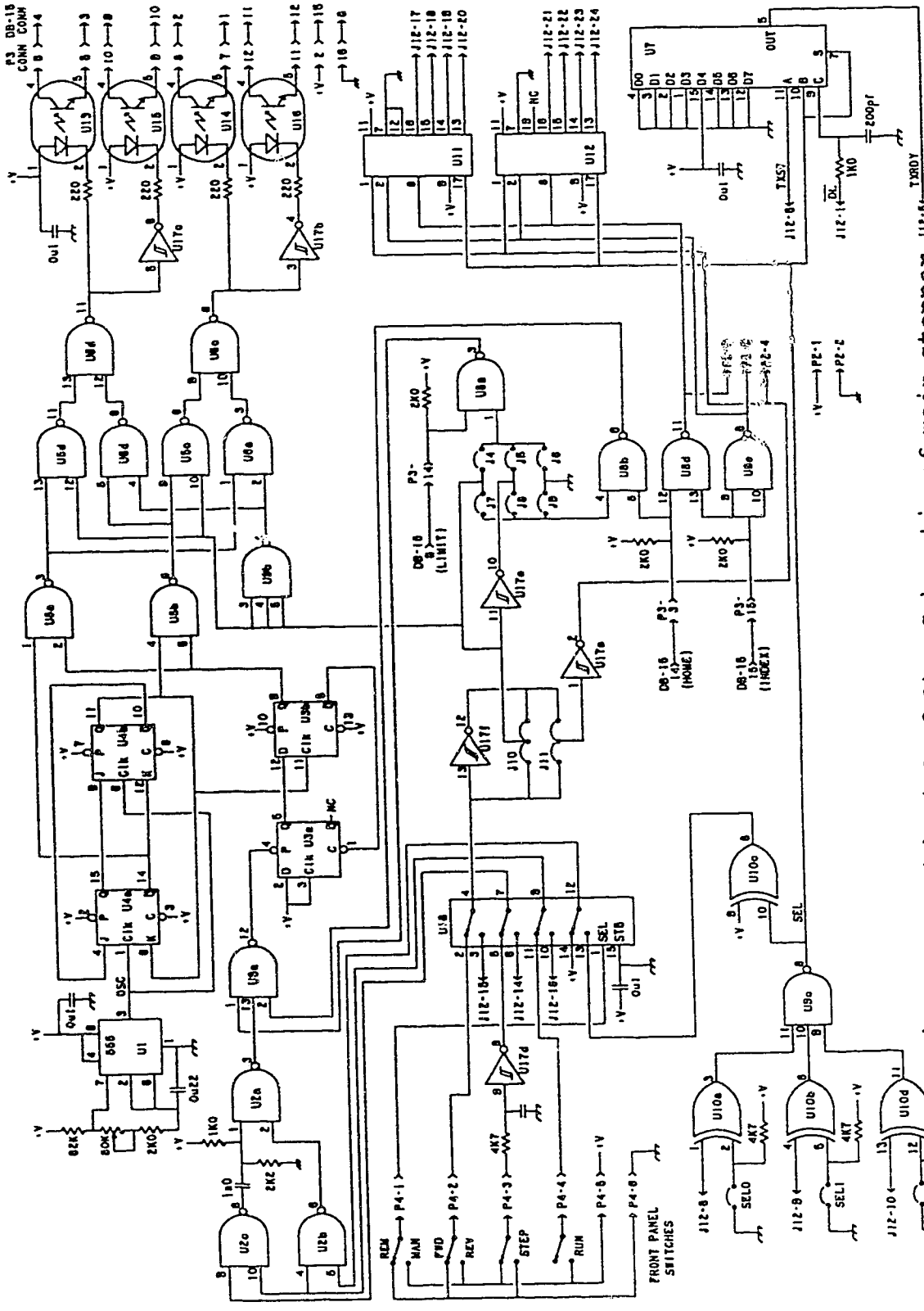

Figure 4.18 (sheet 1 of 2): Schematic of main stepper motor controller board.

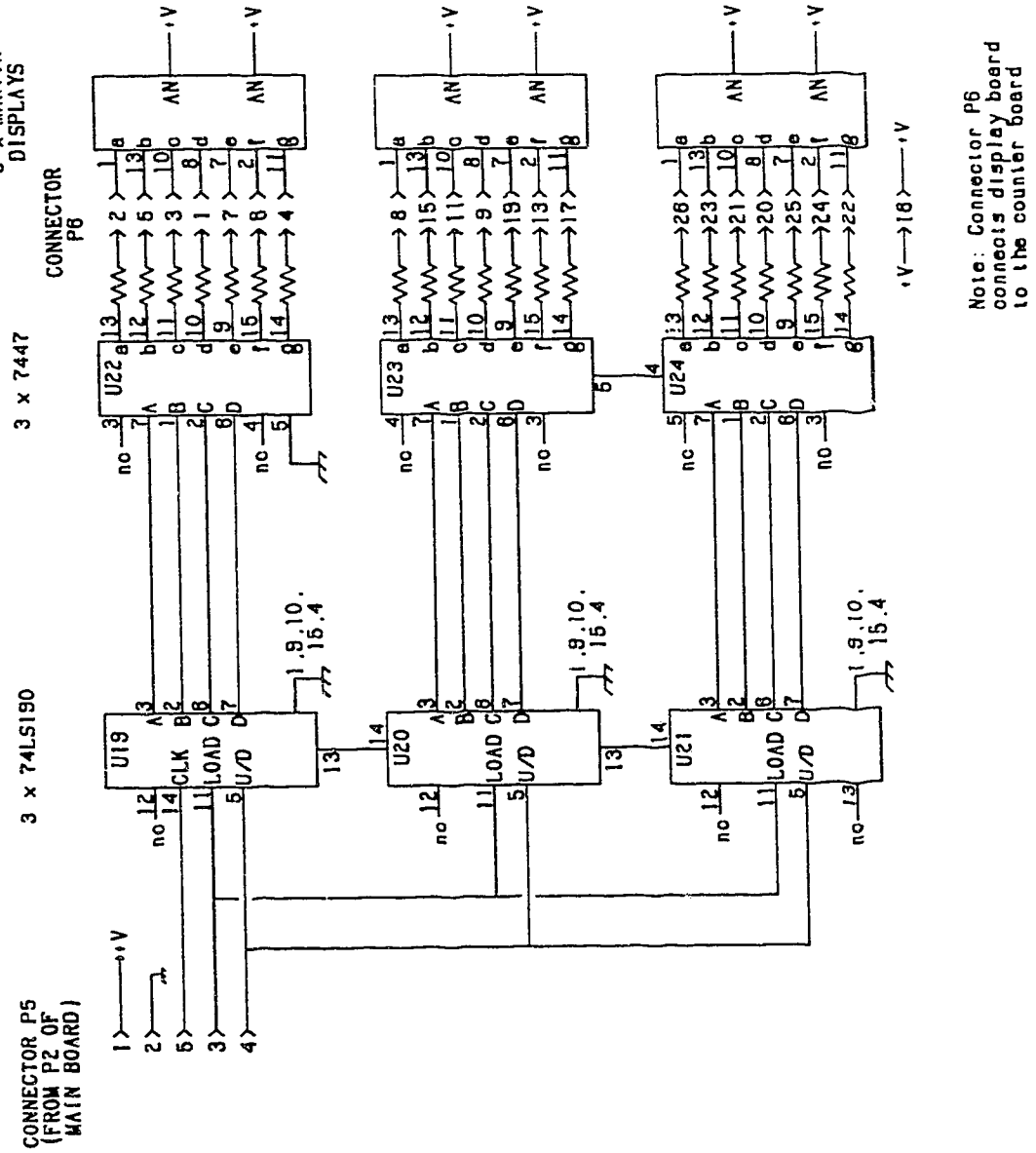

Figure 4.18(sheet 2 of 2): Schematic of piggyback counter board and 7-segment display board.

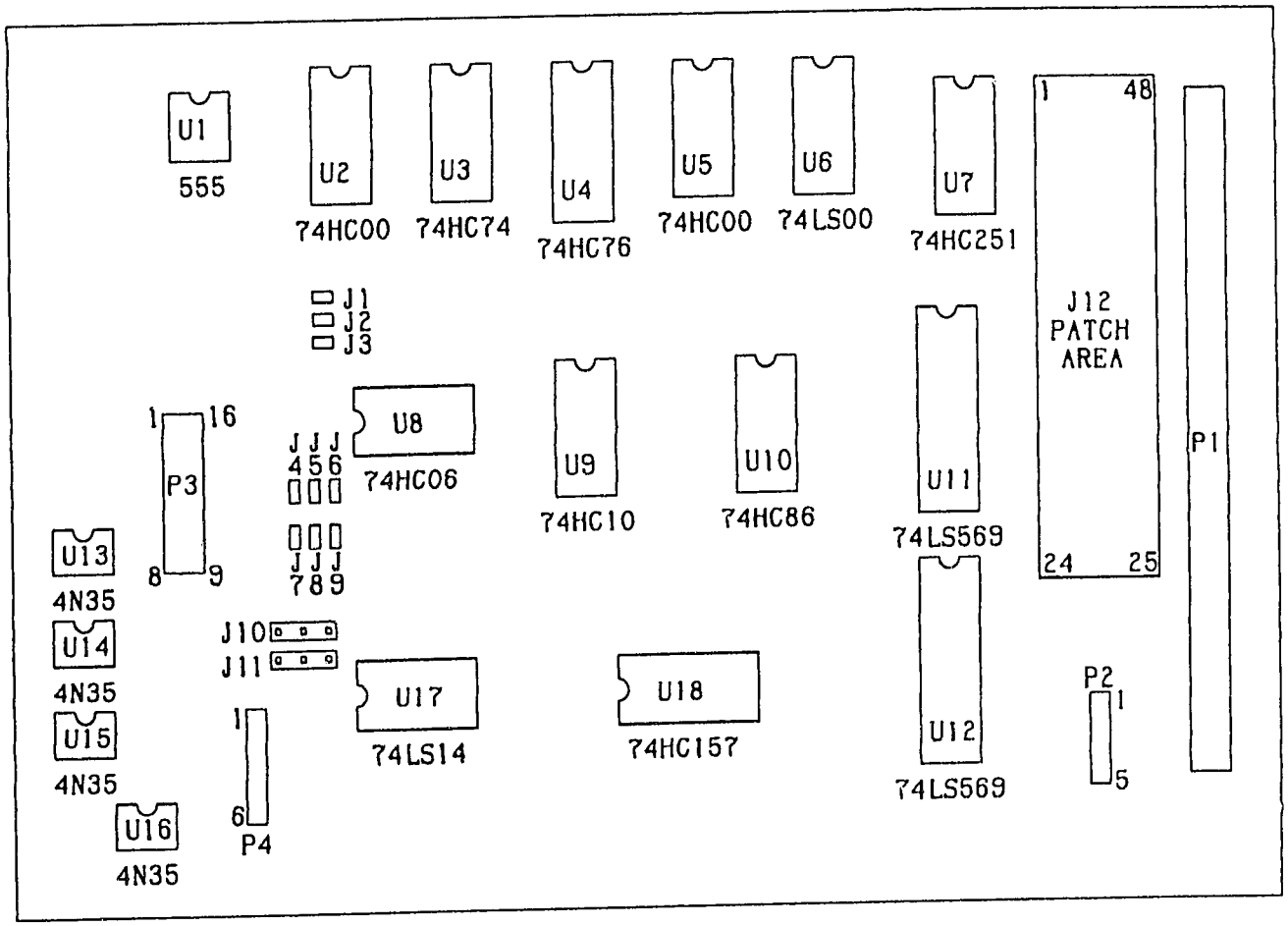

Note: Connector P1 uses standard VME bus notation.

Figure 4.19: Stepper motor controller board component and jumper location.

either travel limit is reached.

Two jumpers are provided for directional control. J10 (jumper left or right section only) selects the motor rotation to match the "forward" and "reverse" position on the front panel. This is more convenient than having to exchange the motor phasing. Jumpers J11 supply a similar function for the position counters - this determines which motor rotation direction corresponds to incrementing the counters. The counters are cleared when both HOME and INDEX are high, regardless of the up/down selection mode. These functions are provided by U8.

Two counter circuits are provided, one for a visual display, the other to be read on command from the IEEE-488 card. Both counters operate from the same signals; the only reason for using two counter circuits is to avoid the complexities of binary to BCD conversion for local readout, or multi-byte transfers on the IEEE-488 bus. Using two counters, one BCD and one binary, simplified the design and reduced the number of components. The count is the number of index line pulses received. The motor direction determines whether the counters are incrementing or decrementing; the count is therefore an indication of the position of the stepper motor mechanism. When both the home and index signals are present (high), the counters are cleared to zero. Output of the 8-bit binary counters is tri-state logic, to allow multiple cards to pass information to a single IEEE card.

The binary counter is comprised of two four-bit,

tristate output IC's, U11 and U12, cascaded together. Outputs are wired to the patch area J12 for connection to the Europac backplane, a practice consistent with other rack modules built for the lab system [4.6]. However, the binary counter outputs are normal (high=1) while the IEEE-488 bus is inverted (high=0). Thus each bit is received inverted by the computer system. This is a minor inconvenience which necessitates a software correction; a statement "N = 255 - N" is sufficient, where N is the value to be corrected. Alternatively, additional hardware could have been used to invert the data, but this was not considered warranted.

The TTL counters used are very fast and, despite the hysteresis provided by the schmitt trigger, multiple counts can easily occur if the input signals are noisy. For example, the opto couplers used to sense position were found to "bounce", probably due to mechanical vibration. Some form of external circuit to produce clean count signals should therefore be used to ensure accurate counting.

Optical isolators are used to provide the output interface to the motor driver circuit. This allows for simple biasing of the driver transistors, and prevents motor voltages and noise from entering the circuit connected to the IEEE-488 bus.

Three signal lines are provided for external feedback of position information. Two lines are intended for use as overtravel limits, one designated the "HOME" position, the other a "LIMIT" position. The remaining line is an "INDEX" line, intended for use with an index hole giving feedback of

actual motion. For example, a disk with a single hole can be attached to the motor shaft and a transmissive type optical detector will then give a pulse once per revolution of the shaft. The index pulses are used to drive the counter circuits, as described previously. The overtravel limits stop the motor after the current step is complete; additional commands will not cause the motor to step further in the same direction. When the direction of travel is changed, the motor is again permitted to step away from the limit (otherwise the motor would be permanently stuck once the limit was reached). A three position jumper block (J4 through J9 in Figure 4.19) is provided for the two limits so that the directions of limit can be selected, or defeated entirely if such interlocking is not required. Jumpering both limits for the same direction is permissible; in this case either limit will stop the motor.

Minimal "handshaking" is performed with the IEEE-488 card, and is accomplished entirely with U7. Transfer of a byte of data to the 488 card requires that the TXRDY line be used; however, this same signal must be used by all the stepper motor cards, therefore a 74HC251 was chosen for U7 to obtain a tristate output (TXRDY is active high, therefore an open collector approach is not useful). U7 is an eight input data selector, used in this circuit as a combinational logic generator using the three inputs DC, SEL, and TXST. An RC network is used on the DC line to allow the address decoders (SEL0, SEL1 and SEL2) and all tristate drivers to stabilize before the bus read is permitted (when TXRDY goes

high).

4.6.2.3 Drive Circuits

Basic driver circuits are presented in this section. The controller card does not include such circuits to avoid excessive heat dissipation inside the VME rack. Additionally, the opto-isolated outputs can be used to drive motors of differing drive requirements by changing the simple external drive circuits, and also to protect the VME bus and IEEE-488 devices from the motor power supply voltages. Motor grounding can therefore be kept separate from the bus system, a prudent practice which helps prevent ground loops and associated problems.

Figure 4.20 illustrates a simplified drive circuit for PM stepper motors. Q1 and Q4 are turned on with Q2 and Q3 off to drive current through the motor winding and forcing resistor. Reversing the states of the four transistors drives current through the motor winding in the opposite direction. Two such circuits are required for each two-winding motor. Diodes D1 through D4 are freewheeling diodes, which provide a current path for the inductive transients from the winding; this also protects the transistors by limiting the reverse voltage. The forcing resistor decreases the L/R time constant of the winding circuit to allow faster switching. Selection of this resistance is critical for optimal high speed operation, although the applications envisaged here do not require such considerations.

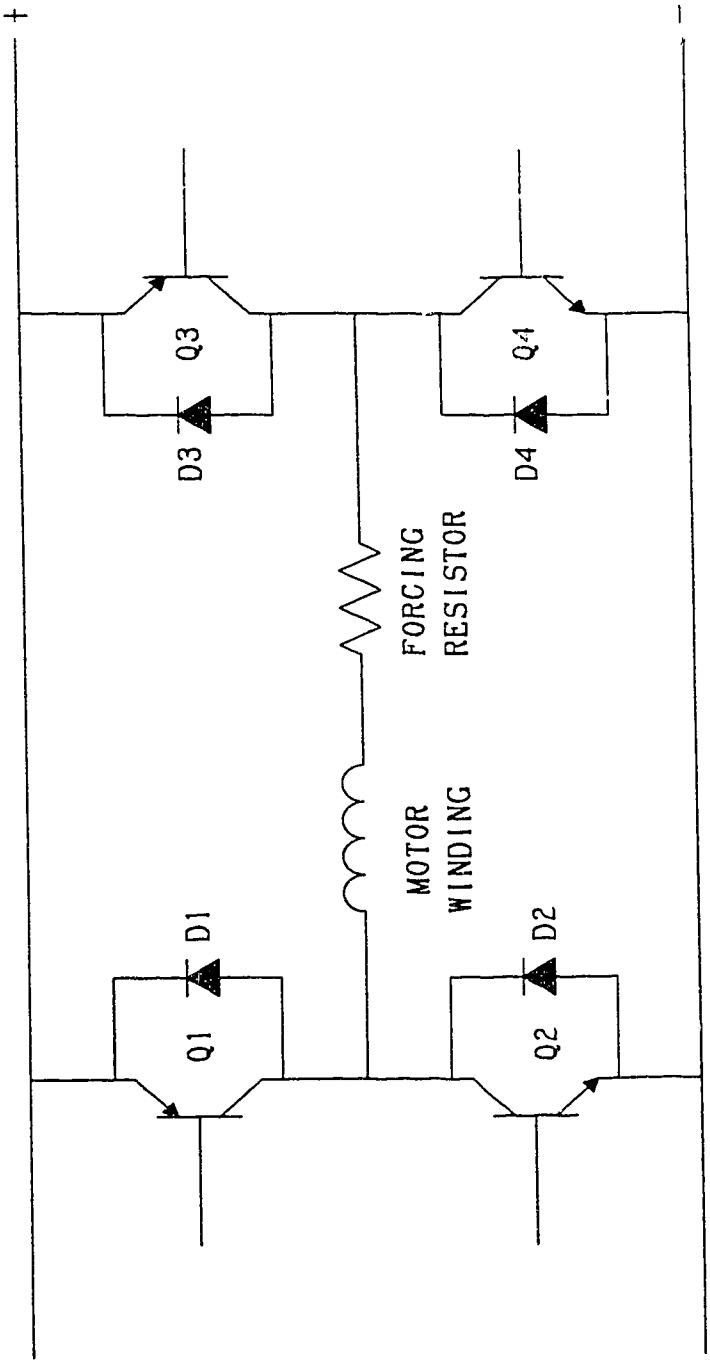

Figure 4 20: Simplified PM motor driving circuit

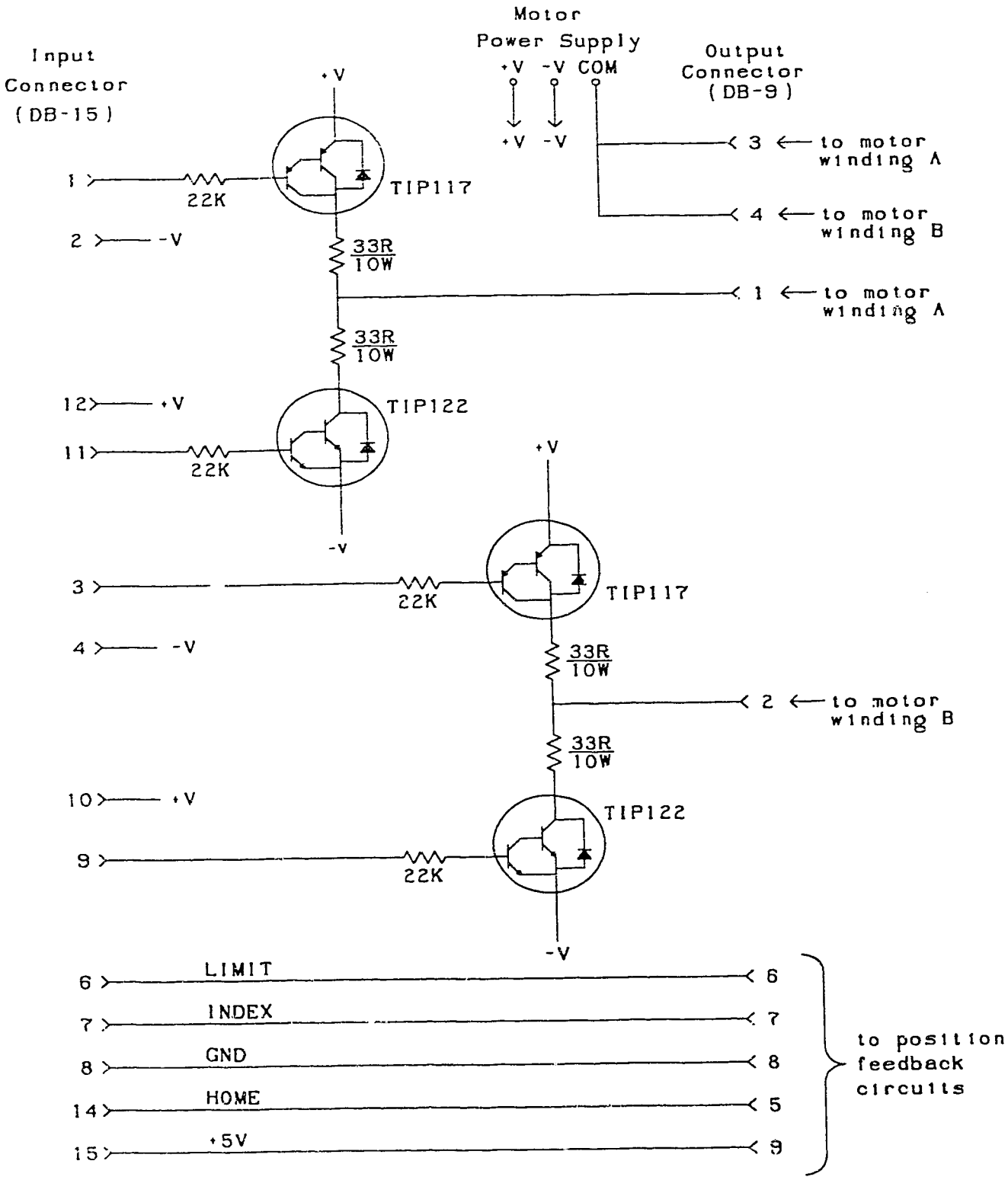

Figure 4.21: Motor Drive Circuit
(as built)

A schematic of the circuit used with the controller card is shown in Figure 4.21. The opto couplers provide electrical isolation from the logic circuits, and provi simple method of driving the power transistors. Note the TIP117 and TIP122 complementary power darlingtons incorporate internal freewheeling diodes. An important change from the "textbook" circuit of Figure 4.20 is the use of two forcing resistors per motor winding. Using two resistors would reduce the transistor current to acceptable values if both transistors were turned on simultaneously (ie. during clock overlap). The two resistor option was selected, since the controller card was not designed to preclude overlaps originating from TTL gate delays. Additionally, the resistors were selected with sufficiently large values that the transistor ratings could not be exceeded, even if the motor windings were shorted or both transistors remained in the "on" state. Signals used for the counters and travel limits are provided at the DB-9 connector for connection to external devices. Typical connections are shown in Figure 4.21.

Chapter 5

Experimental Results

5.1 Noise Measurement Simulation

5.1.1 Numerical Simulation Program

Operation of the measurement system was modelled to verify the method of Chapter 3. A simulation program was written in FORTRAN, consisting of two major parts: a set of subroutines to calculate what the noise power measured by the receiver would be, and subroutines to use these noise power readings to estimate the DUT noise temperature and available gain using the procedure described in Chapter 3. A small driver program was used to read the apparatus parameters from a data file, and perform cable calibration and tuner loss compensation as required. Four different tuner loss correction strategies were simulated using different versions of the driver program. The functions of the various subroutines are described briefly below.

The four noise power subroutines each compute the indicated receiver noise power for a different apparatus configuration. Figure 5.1 shows a block diagram of the modelled apparatus. The parameters used for the simulation can be changed by altering the appropriate values in the data file. The four measurements possible are:

1. Cold load and tuner connected to the isolator, giving a single noise power reading (other measurements yield two values) for cable calibration.
2. Noise source connected via cable and bypass to the

isolator, yielding two noise power values also needed for the input cable calibration.

3. Noise source connected via cable and tuner to the isolator, to obtain data for the tuner loss compensation.
4. Noise source connected via cable, tuner and DUT to the isolator, to simulate readings necessary to estimate the DUT available gain and noise temperature.

Noise and scattering parameters are used to compute the available gain and noise power of the DUT and isolator. Variable tuner loss is modelled by assigning values of tuner available gain which increase linearly from $\Gamma_T = 0$ to $\Gamma_T = 0.95$. For some simulations this gain is set to unity to represent a lossless tuner, although the bypass remains lossy.

The driver program calls subroutines which perform the various stages of measurement and simulate the cable calibration and tuner loss compensation. Three subroutines provide the following measurement functions:

1. A calibration routine which performs an input cable calibration using the new method.
2. A tuner loss compensation subroutine which computes the tuner loss, and calculates the equivalent "on" and "off" noise temperatures available at the tuner output.
3. A DUT measurement program which estimates the DUT available gain and noise temperature.

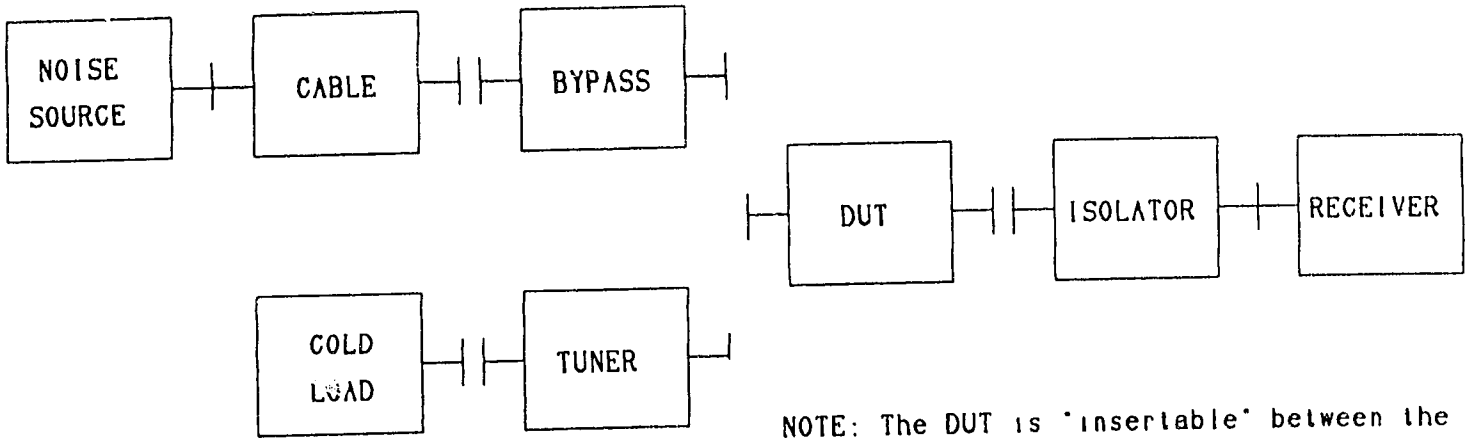

Figure 5.1: The apparatus as modelled in the simulation.

A cable calibration is always used to compensate for the noise properties of the input cable. Tuner loss compensation is used in various ways to illustrate its effect. The actual DUT gain and noise temperature used by the noise power subroutines are also available to the driver program for calculation of measurement errors. The data plotted in Figure 5.2 through 5.11 were obtained using this simulation.

5.1.2 Simulation Results

This section describes the results of the simulation performed by modelling the apparatus of Figure 5.1. A passive circuit was constructed with the intention of achieving a high value of S_{11} and moderate loss in a device which would be measured after cooling. This circuit is described in section 5.3.2 below. Its S-parameters were measured with the experimental apparatus and de-embedded using previously obtained error vectors. The values were:

$$s_{11} = 0.870 \angle -163.2^{\circ}$$

$$s_{12} = 0.321 \angle -77.5^{\circ}$$

$$s_{21} = 0.323 \angle -71.9^{\circ}$$

$$s_{22} = 0.811 \angle -176.88^{\circ}$$

The corresponding noise parameters were computed assuming a physical temperature of 13K and found to be:

$$T_N = 14.5 \text{ K}$$

$$T_{min} = 9.10 \text{ K}$$

$$\Gamma_{opt} = 0.766 \angle 167.4^{\circ}$$

Plots were produced illustrating the results of

simulating measurements of the passive DUT. In all cases, the tuner reflection coefficient, Γ_T, is increased from zero (Smith Chart origin) to a magnitude of 0.95 in the direction which traverses Γ_{opt}.

Figure 5.2 shows the simplest case, in which there is no tuner loss and no noise produced by the receiver input isolator. The available gain of the isolator, however, does vary as a function of the output reflection coefficient of the DUT, as described in section 3.6.3.4. Both the available gain and the noise temperature of the DUT are found to be computed correctly, and the results are exact. For most plots presented here, a plot of the systematic measurement error will accompany the plot of gain and noise temperature. In this instance the error for both is zero, and this graph is omitted.

Figure 5.3 shows the effect of tuner loss only on measurement accuracy when no tuner loss compensation is used. Both the DUT gain and noise temperature are now in error, and the apparent value of Γ_{opt} has decreased in magnitude. The measurement error is quite high in the vicinity of Γ_{opt}; in addition, the magnitude of Γ_{opt} will be underestimated due to the effect of increasing tuner loss.

Performing a single tuner loss compensation (at Γ_T = 0), as shown in Figure 5.4, results in reducing the error slightly. A reduction is obtained in the error of T_{DUT} from about 75% to 60%, near the noise temperature minimum. The effect of ignoring the increase in tuner loss is clearly shown in Figure 5.4.

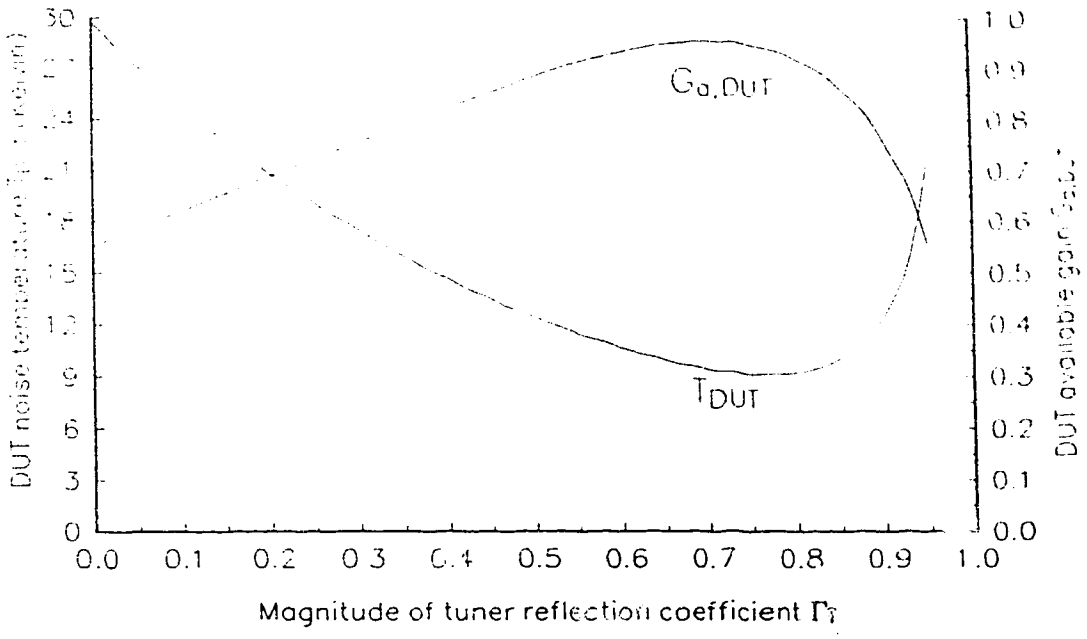

Figure 5.2: Simulated measurement of T_{DUT} and $G_{A,DUT}$ with no tuner loss or isolator noise.

If a new tuner loss correction is made at each data point, DUT gain and noise temperature errors are reduced to zero and results identical to Figure 5.2 are obtained. The tuner loss compensation and cable calibration derived in Chapter 3 produce correct results, despite the variable tuner loss.

Each tuner loss estimate requires additional relay switching and measurements when actual experiments are performed. Such effort can be reduced by compensating for loss only occasionally. Accuracy of the final noise parameters is unaffected, provided sufficient corrections are performed to ensure the actual value of $\Gamma_{opt.}$ is reached. Figure 5.5 shows a hypothetical measurement in which three loss measurements are performed.

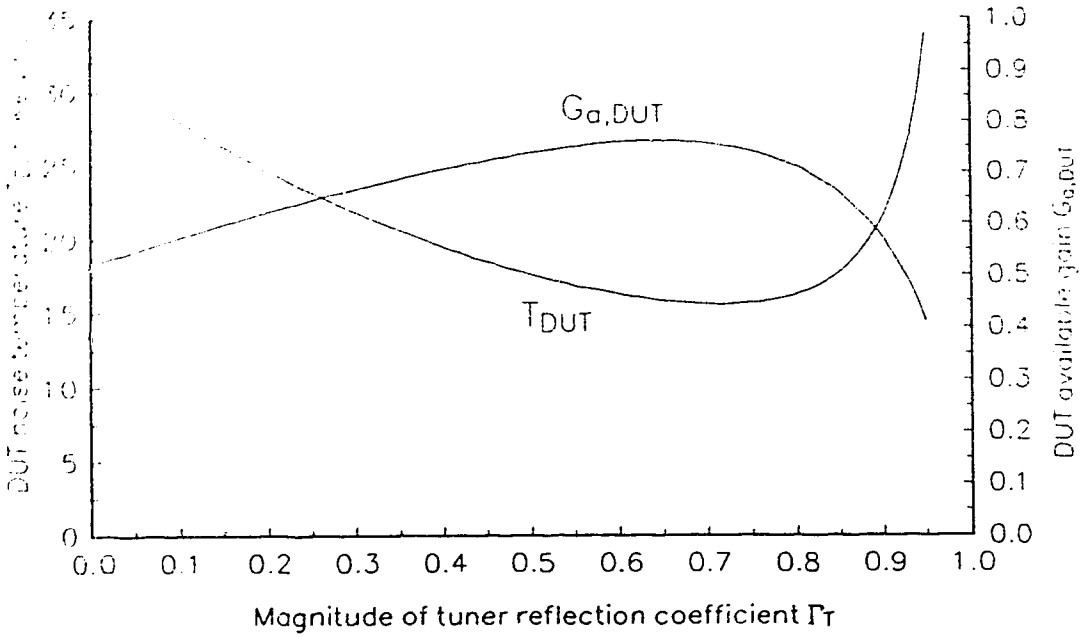

(a) Measurement of T_{DUT} and $G_{A,DUT}$

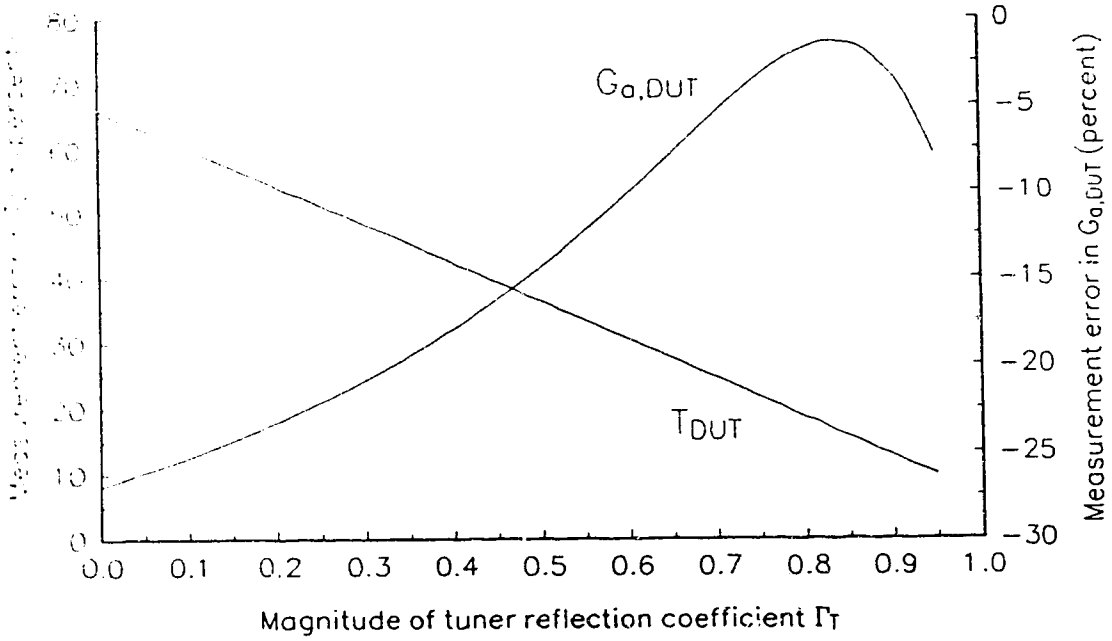

(b) Measurement error in 5.3(a).

Figure 5.3: Simulation with lossy tuner and noiseless isolator; no tuner loss compensation.

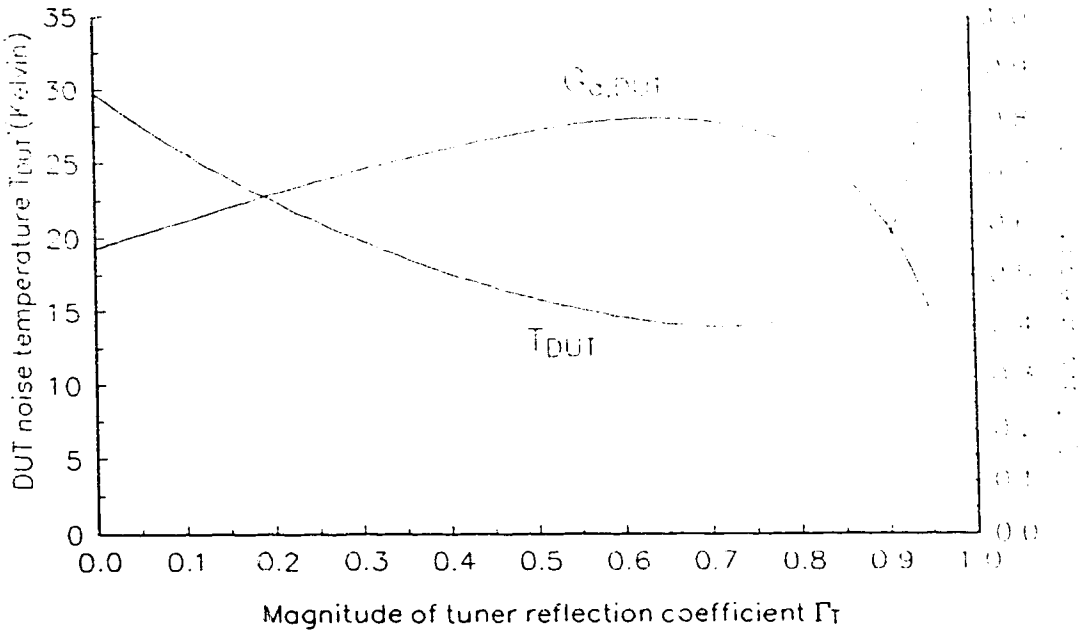

(a) Measurement of T_{DUT} and $G_{A,DUT}$

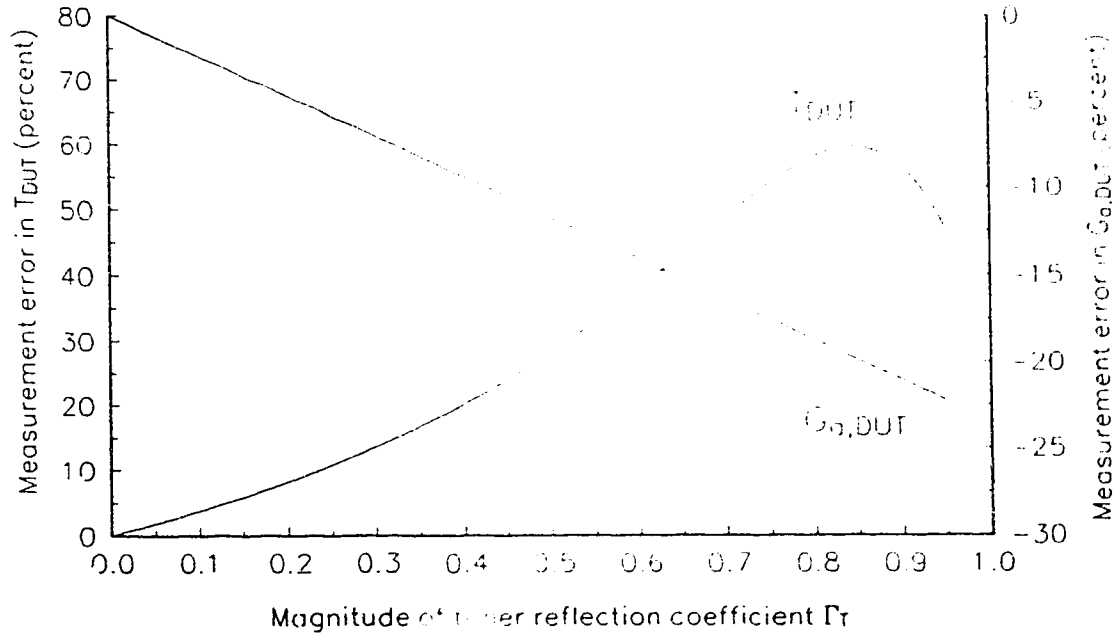

(b) Measurement error in 5.4(a).

Figure 5.4: Simulation with lossy tuner and noiseless isolator; single tuner loss compensation at $\Gamma = 0$.

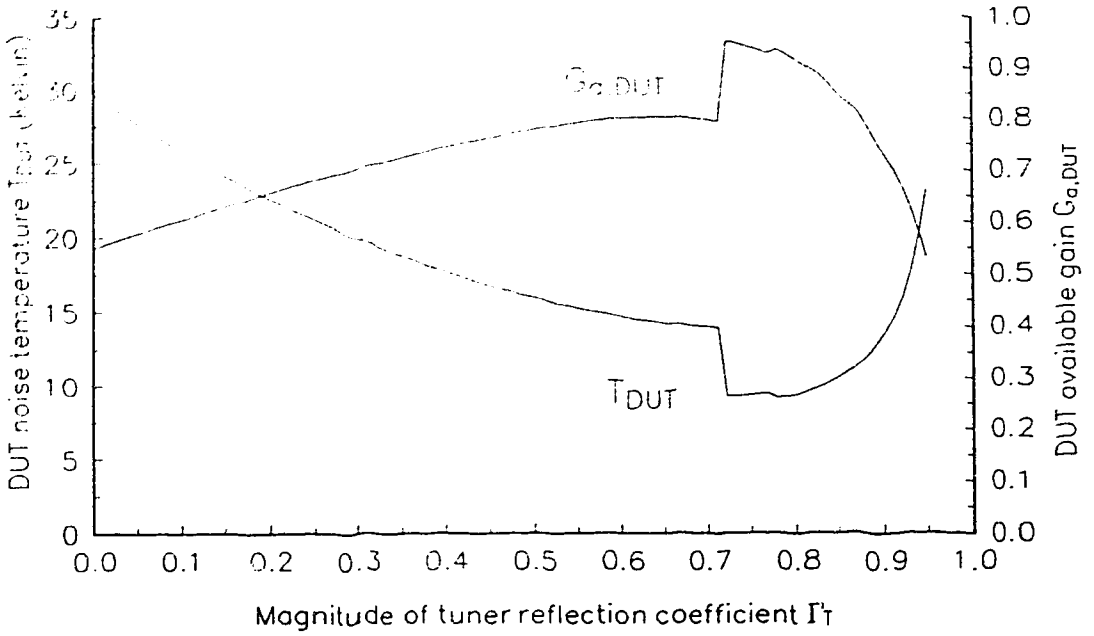

(a) Measurement of T_{DUT} and $G_{A,DUT}$

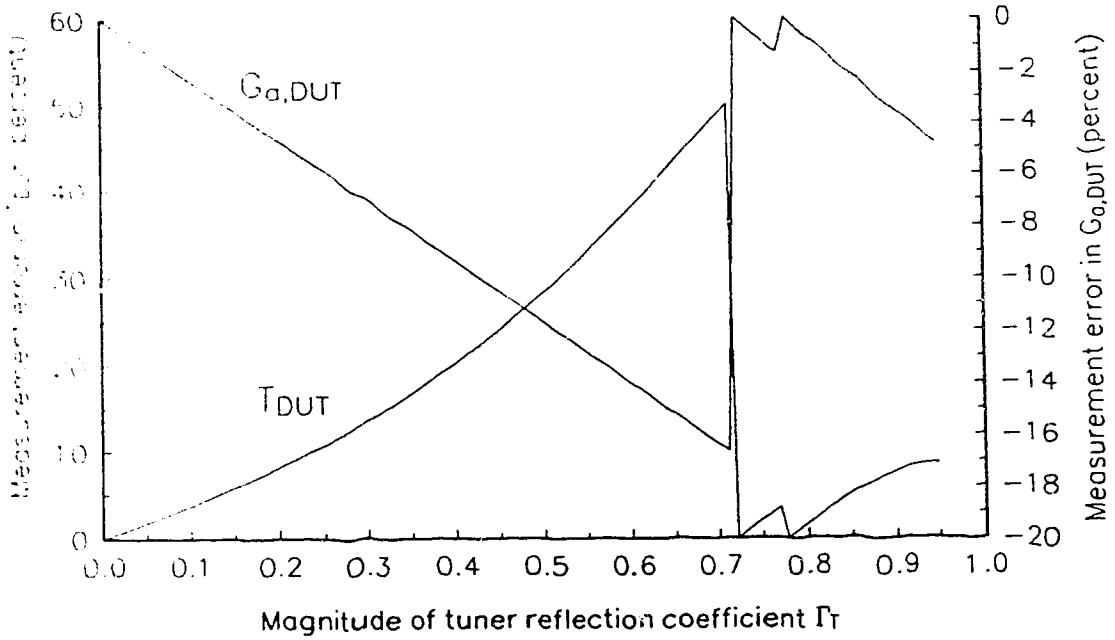

(b) Measurement error in 5.5(a).

Figure 5.5: Simulation with lossy tuner and noiseless isolator; three loss compensations performed.

The simulations discussed so far have all assumed a lossy but noiseless isolator. This condition was achieved by setting T_N and T_{min} of the isolator model to zero. The available gain of the isolator is a function of the output reflection coefficient of the DUT, which in turn depends on Γ_T. The available gain of the isolator thereby varies with tuner setting, but this effect is properly corrected.

When the simulated isolator is permitted to assume reasonable noise properties (corresponding to a physical temperature of 13K), the noise contribution due to the isolator introduces error, as shown in Figure 5.6. This error cannot be removed without further enhancements to the algorithm. Only the DUT noise temperature is affected; the gain is still determined with no error. The manufacturer's specified maximum value of isolator loss (0.2 dB) is used, so the errors calculated represent a worst-case contribution.

Figur illustrates the combined effects of a lossy tuner and a noisy isolator. No tuner loss correction is performed, and large errors in T_{DUT} are apparent. A single correction at $\Gamma_T = 0$ produces the results of Figure 5.8. Errors are still large despite modest improvement, primarily due to the low DUT available gain which exacerbates the effect of isolator noise. A simulation using tuner loss compensation for every measurement was also performed; as expected, the results are identical to those of Figure 5.6. Using only three corrections (as for Figure 5.5) yields the results shown in Figure 5.9.

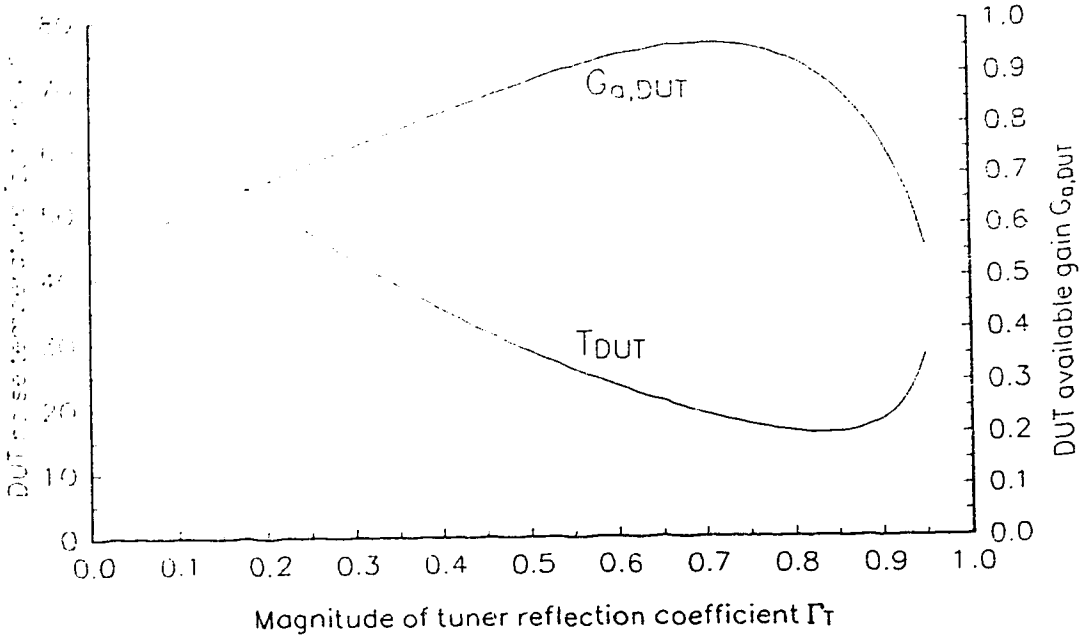

(a) Measurement of T_{DUT} and $G_{A,DUT}$

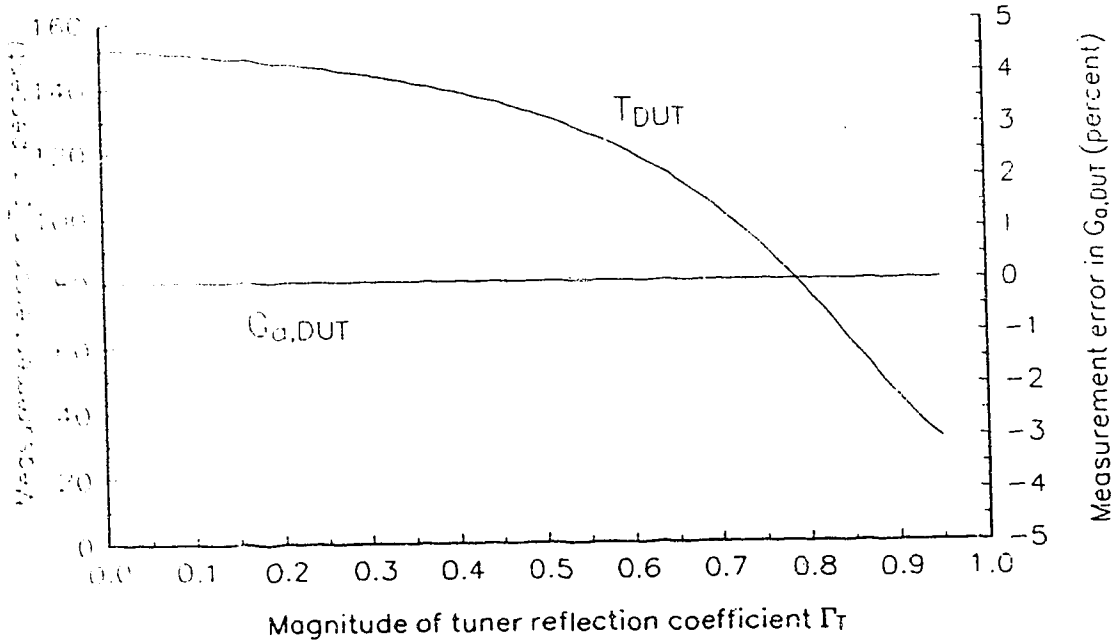

(b) Measurement error in 5.6(a).

Figure 5.6: Simulation with lossless tuner and noisy isolator; single tuner loss compensation.

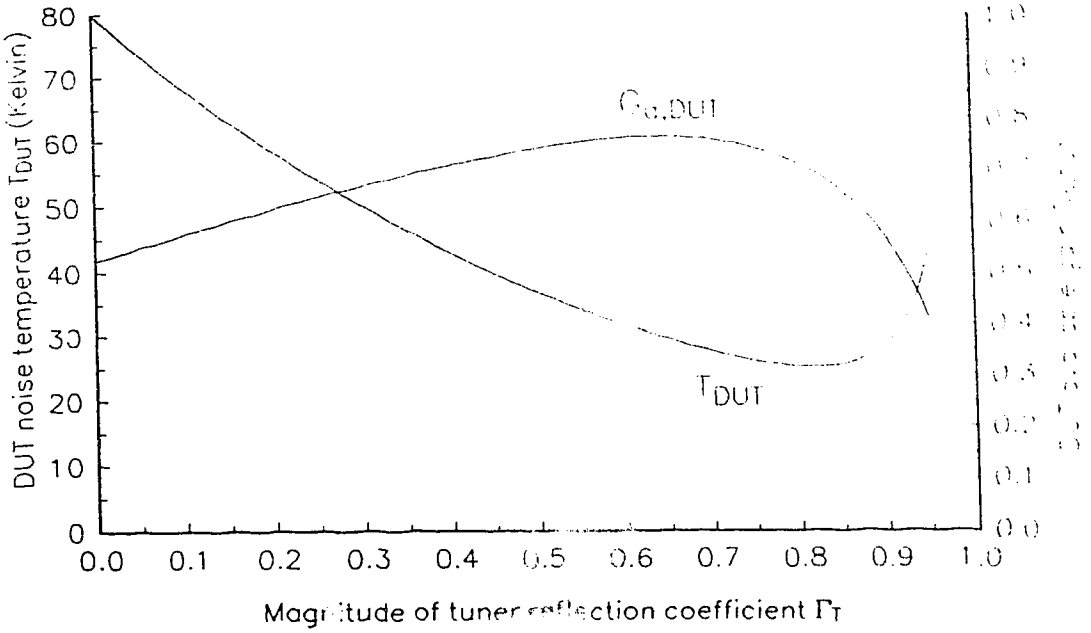

(a) Measurement of T_{DUT} and $G_{A,DUT}$

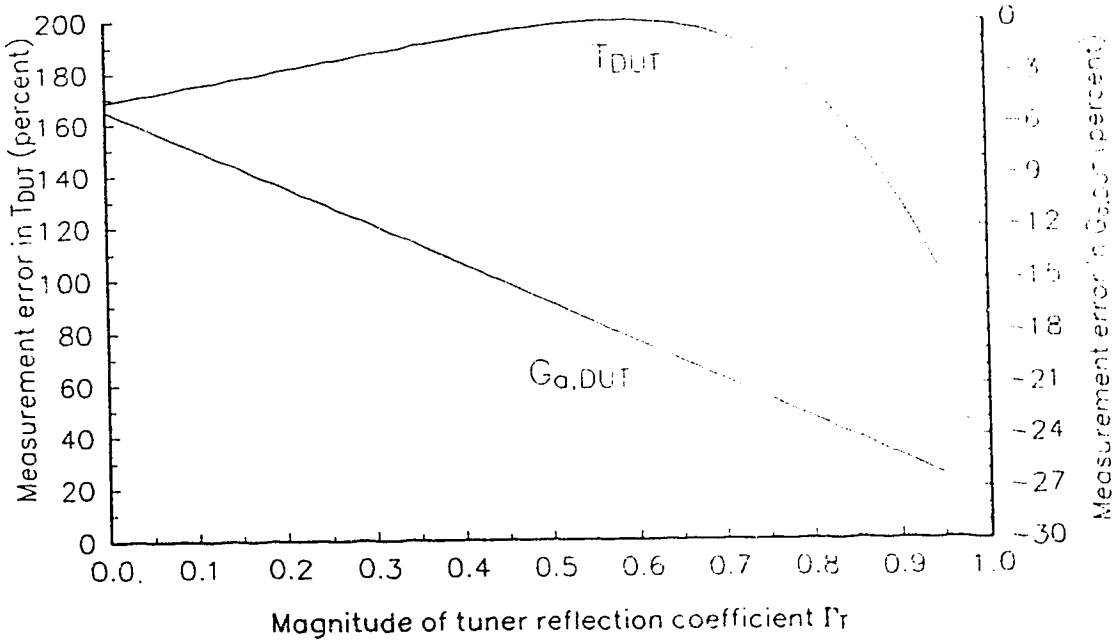

(b) Measurement error in 5.7(a).

Figure 5.7: Simulation with lossy tuner and noisy isolator; no tuner loss compensation.

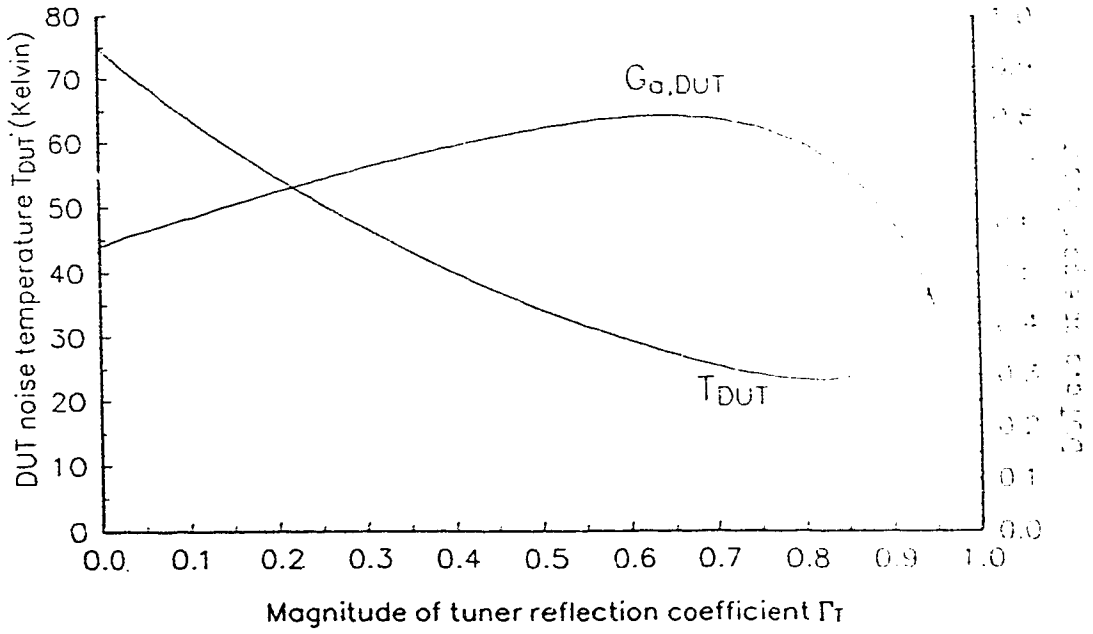

(a) Measurement of T_{DUT} and $G_{A,DUT}$

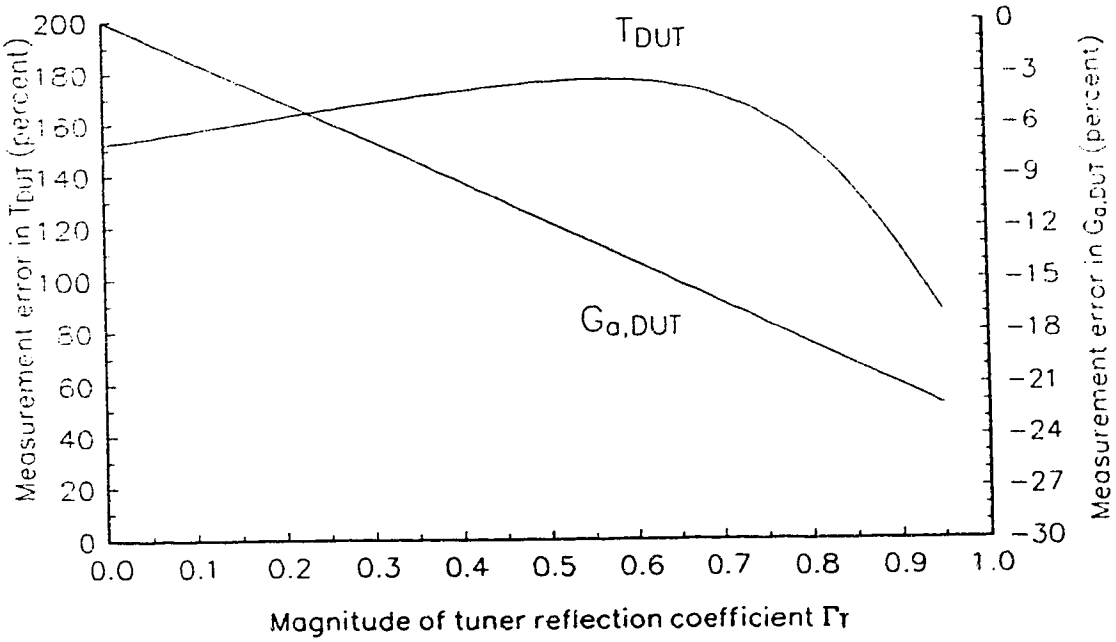

(b) Measurement error in 5.8(a).

Figure 5.8: Simulation with lossy tuner and noisy isolator single tuner loss compensation at $\Gamma = 0$.

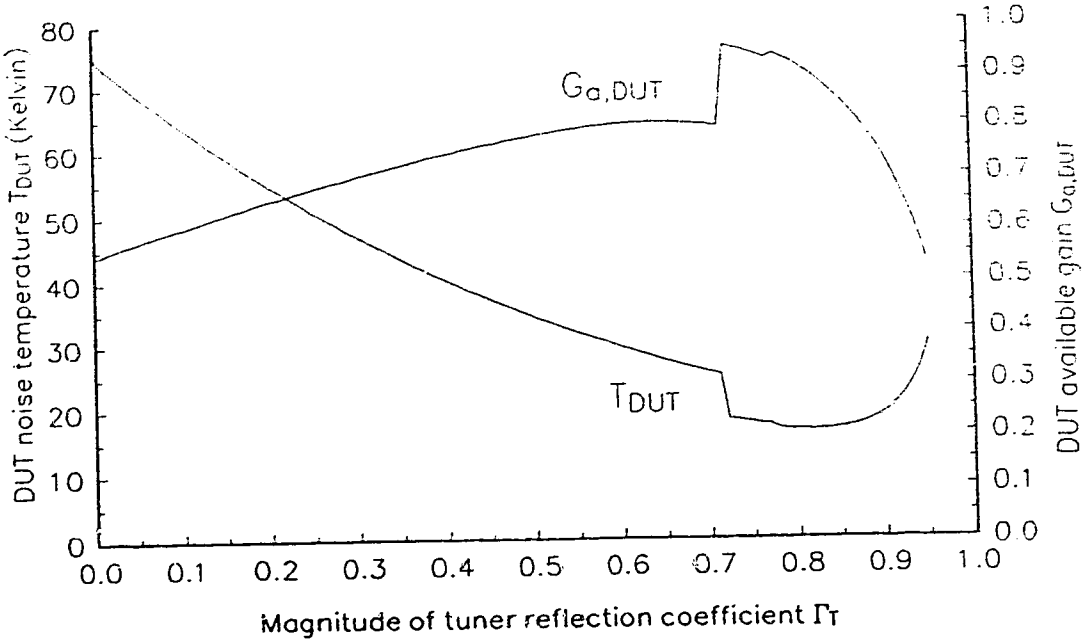

(a) Measurement of T_{DUT} and $G_{A,DUT}$

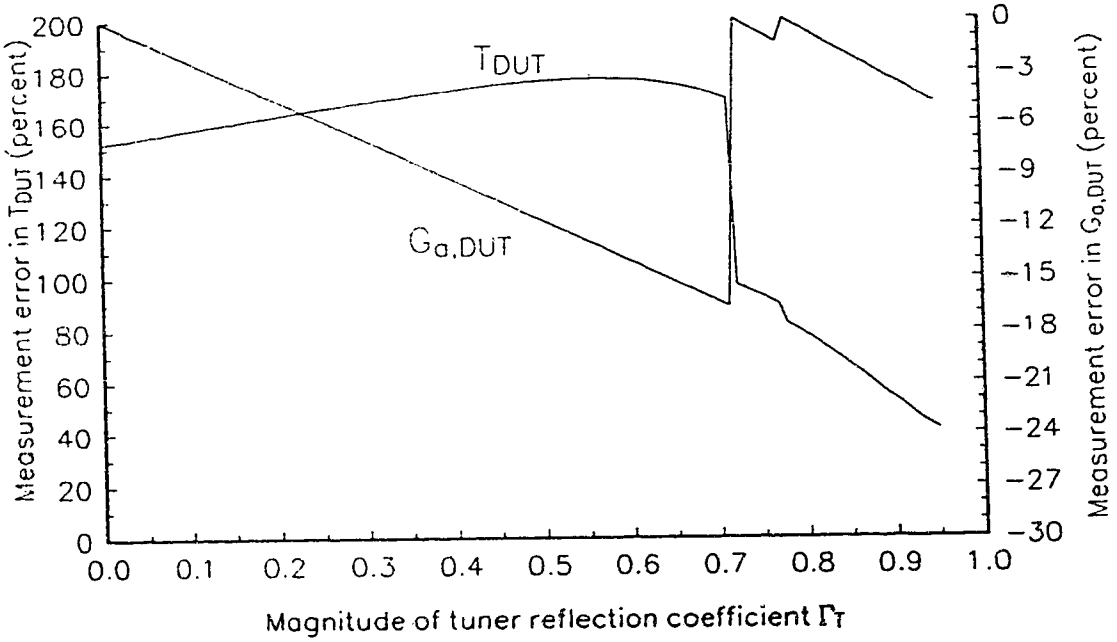

(b) Measurement error in 5.9(a).

Figure 5.9: Simulation with lossy tuner and noisy isolator; tuner loss compensation at three points.

Low DUT gain increases the effect of the isolator noise contribution. In order to obtain estimates of these effects for a FET, some of the previous simulations were repeated using transistor DUT data. The simulation program requires both noise parameters and S-parameters of the DUT as input data, and finding such data proved difficult. Pospieszalski [5.1] claims the measurement of S-parameters at cryogenic temperatures is much more difficult than the measurement of noise parameters. However, he explains that a room temperature model was used for his cryogenic data, because the S-parameters are believed not to change much with temperature. For purposes of illustration, the author therefore selected a set of room temperature S-parameters, obtained at 8.4 GHz by linear interpolation of the manufacturer's data for a type FSC10A GaAsFET. Cryogenic noise parameter data for the packaged FET from [5.1] was selected to complete the required data. Although all experiments relating to this thesis were performed at 4.0 GHz, the 8.4 GHz data can be used because frequency is not used as a parameter for the simulation. The FET parameters used are:

$$S_{11} = 0.590 \angle -142.0^{\circ}$$

$$S_{12} = 0.107 \angle -9.6^{\circ}$$

$$S_{21} = 1.936 \angle 35.2^{\circ}$$

$$S_{22} = 0.447 \angle 119.4^{\circ}$$

$$T_N = 23.6 \text{ K}$$

$$T_{min} = 10.2 \text{ K}$$

$$\Gamma_{opt} = 0.89 \angle 113.0^{\circ}$$

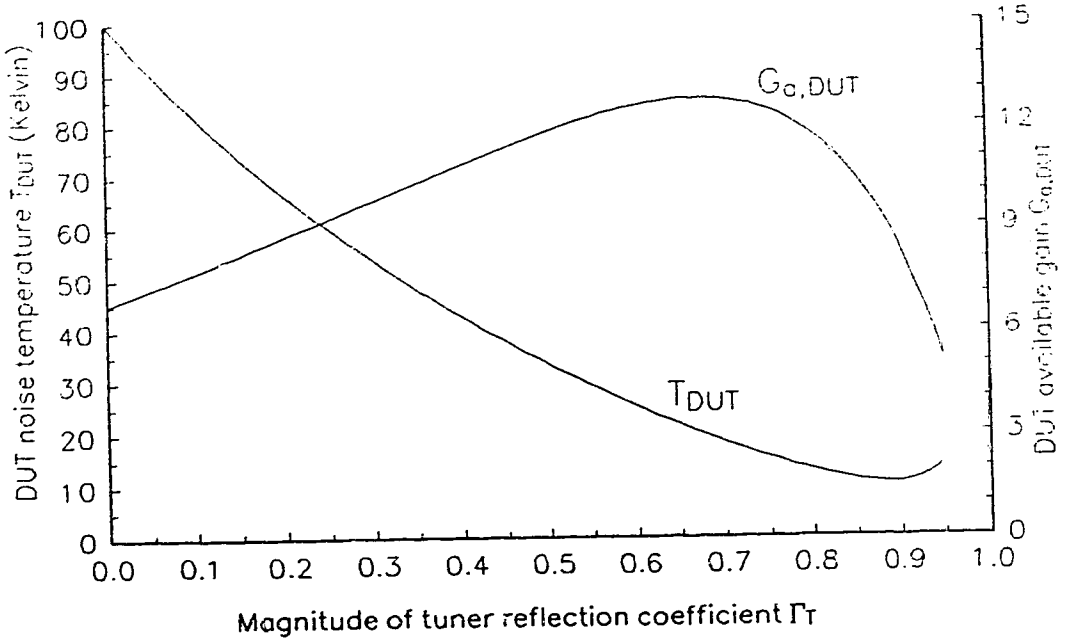

Figure 5.10: Simulation of HEMT measurement with noiseless isolator; and full tuner loss compensation.

Figure 5.10 shows the DUT noise and gain when the isolator is modelled as noiseless. No error plot is included since the systematic error is zero. For comparison, Figure 5.11 illustrates the effect of a noisy isolator. The magnitude of Γ_{opt} is underestimated slightly, but probably with sufficient accuracy for amplifier design data. A significant reduction in T_{DUT} error (compared to that of a passive DUT) is obtained due to the higher gain of the DUT.

Numerical simulation of the new calibration method and the tuner loss compensation technique presented in Chapter 3 verify these algorithms. Additionally, the effects of isolator noise have been shown, though this thesis makes no

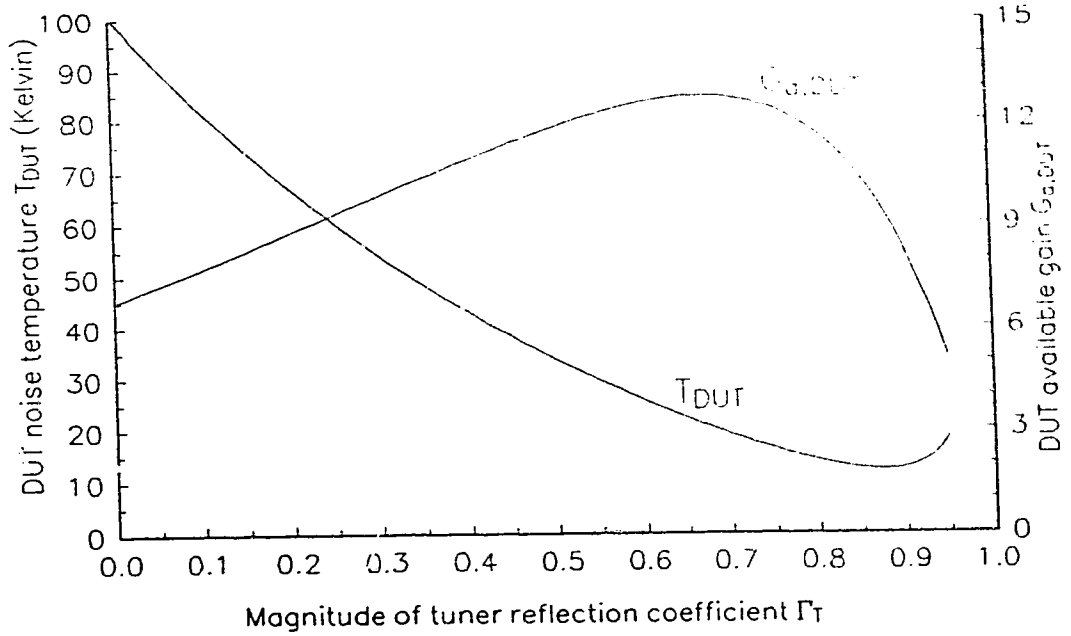

(a) Measurement of T_{DUT} and $G_{A,DUT}$

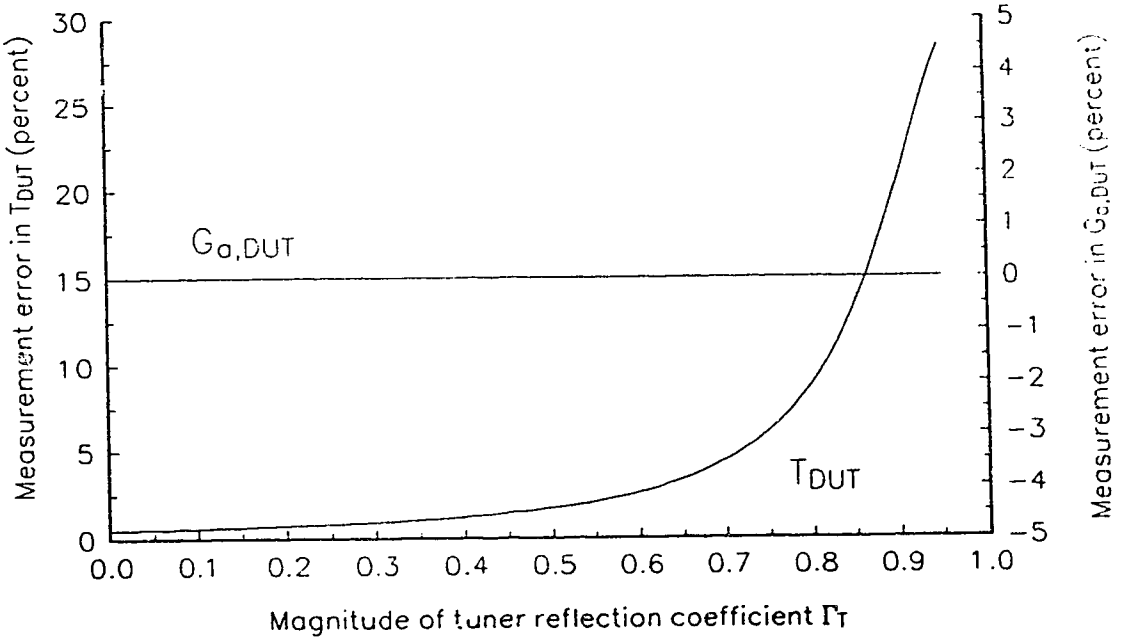

(b) Measurement error in 5.11(a).

Figure 5.11: HEMT simulation with noisy isolator and lossy tuner; and full tuner loss compensation.

attempt to correct such effects. The success of the simulation also supports the value of the N-T diagram analysis and the use of the two-port substitution method of Chapter 3.

5.2 Cryogenic S-parameter Measurements

S-parameter calibration measurements of cooled devices were performed only after the apparatus had established thermal equilibrium, six hours (or more) after all temperature sensors reached their final values. The first-tier OSLT calibration was performed, and successful completion was verified by measuring known (room temperature) devices not used as calibration standards. Data required for the second-tier 3ST calibration were then obtained by measuring the fixture placed in the cryostat. After measurement, the first-tier calibration was rechecked to ensure equipment integrity.

Three separate cryostat runs were performed to obtain the four sets of data needed. Calibration was performed at six frequencies, from 3750 to 4250 MHz in 100 MHz increments. The 3ST algorithm of Chapter 2 was then applied to obtain the error vectors, assuming both reference planes to be located 400 mm from the duroid edge of the input port. Input data for 3950 MHz is shown below:

$$M_A = 0.8265 \angle -62.55^\circ$$

$$M_B = 0.8200 \angle 67.85^\circ$$

$$M_C = 0.8300 \angle 168.80^\circ$$

$$M_D = 0.8460 \angle 174.70^\circ$$

$$M_F = 0.8235 \angle -65.25^\circ$$

$$M_G = 0.8100 \angle 70.85^\circ$$

$$M_{03} = 0.8110 \angle 67.24^\circ$$

$$M_{30} = 0.8110 \angle 67.24^\circ$$

The error vectors are then found to be:

$$E_{00} = 0.0913 \angle 113.85^\circ$$

$$E_{11} = 0.1089 \angle -122.20^\circ$$

$$E_{22} = 0.0712 \angle -0.19^\circ$$

$$E_{33} = 0.0732 \angle 157.15^\circ$$

$$E_{01}E_{10} = 0.8158 \angle 168.40^\circ$$

$$E_{01}E_{23} = 0.8144 \angle 67.61^\circ$$

$$E_{10}E_{32} = 0.8144 \angle 67.61^\circ$$

$$E_{23}E_{32} = 0.8211 \angle -39.03^\circ$$

Pairs of error vectors (eg. $E_{01}E_{10}$) can be cross checked using a relation of the form

$$E_{01}E_{10} = \frac{E_{01}E_{23}\ E_{10}E_{32}}{E_{23}E_{32}} .$$

Using this technique, the disagreements with the cross check values were found to be:

Vector	Δ Mag.	Δ ϕ
$E_{01}E_{10}$	0.008	5.9
$E_{01}E_{23}$	0.008	5.9
$E_{10}E_{32}$	0.008	5.9
$E_{23}E_{32}$	0.008	5.9

Calibration at other frequencies was less satisfactory,

but the cross check error was typically 0.02 in magnitude and 10° in phase. The worst case errors occurred at 3750 MHz with a magnitude error of 0.002 and a phase error of 16.0°, and at 4250 MHz with errors of 0.025 and 10.3°.

Although the cross check is useful for detecting large errors, verification by measuring a known DUT is also desirable. An attempt was therefore made to measure a microwave resistor installed across a gap in a 50 ohm stripline. The results obtained were entirely inconsistent with the predicted value. However, when the apparatus returned to room temperature, it was found the resistor had fractured into several pieces. A second attempt was made, this time with the shortest possible resistor leads to reduce thermal stress, with the same result. The time required to fabricate a suitable test stripline pattern for the fixture caused further verification efforts to be abandoned.

5.3 Experimental Noise Measurements

5.3.1 HEMT Measurements

The initial noise measurement experiments were performed using a HEMT (in the stripline fixture) as a DUT. Originally a chip transistor of type NE32000, manufactured by NEC, was attached to the test fixture conductor (Figure 4.6(d)) using silver epoxy. Gold bond wires were then attached to the stripline conductors using thermal compression bonding.

After assembling the test fixture containing the HEMT,

a quick room-temperature S-parameter measurement was made to ensure the device was functional. The transistor appeared functional, and did not exhibit any oscillations or unusual behaviour.

The chip HEMT was then installed in the cryostat, where its room temperature behaviour again seemed normal. Upon cooling, the transistor began to exhibit undesirable properties at a temperature of about 150K. Adjustment of I_{DS} was possible only over the range 13 to 15 mA, as if the gate voltage were not controlling much of the channel current. This phenomenon is not unlike that reported by Pospieszalski, et al. [5.2].

In the range 70 to 100K a "memory effect" was observed, where the device characteristics were no longer time invariant. A sudden manual increase in V_{DS} would cause an immediate anomalous rise in I_{DS}, which returned to its original value after a period of some 5 to 6 seconds. A quick decrease in V_{DS} would result in a corresponding I_{DS} decrease, which disappeared again after some 5 or 6 seconds. The origin of this behaviour is unknown.

As the temperature decreased further, the range of I_{DS} control diminished to essentially zero at 17K. Furthermore, the value of V_{GS} seemed to be about 0.1 V below the value of V_{DS}, regardless of the V_{DS} value. Current control using the bias supply I_{DS} adjustment was ineffective. The bias supply is a feedback design, so analysis of the problem would have to consider the possible effects of abnormal transistor behaviour on the control circuits.

The apparatus was allowed to return to room temperature, and a red LED [5.2] was installed in the top of the fixture to illuminate the HEMT. A current power supply was used to maintain a constant 20mA through the diode, regardless of temperature.

Upon cooling the chip HEMT again, it was found that the illumination prevented the memory effect previously experienced, and also provided a wider range of I_{DS} control at temperatures where V_{GS} did not control the drain current completely. Below 50K, the HEMT acted as a resistance from drain to source, with the gate voltage having no influence.

After returning to room temperature, the HEMT behaviour did not return to normal, indicating the likelihood of permanent device damage due to cooling. A large percentage of drain current remained uncontrolled by the gate voltage. During the installation of this transistor, ultrasonic bonding was inadvertently used to attach one of the bond wires to the die. This chipped a small piece off the corner of the transistor, although no visual damage was observed near the patterned regions of the device. The role of the damage in the HEMT failure was not determined.

Attempts to measure transistor noise parameters were then made using a Sony type 2SK676 packaged HEMT. Illumination of the transistor when cooled appeared to improve the I-V characteristics, so the LED was used for the remainder of the experiments. Control of I_{DS} from zero to I_{DSS} was possible.

This transistor operated in a normal and stable manner

until the temperature was reduced to about 150K, where the device probably began oscillating. Evidence of oscillation was observed in the form of unstable bias conditions. An interesting phenomenon was noticed wherein the bias voltage variations were locked to the sweep of the spectrum analyzer, whose input had been connected to the HEMT input to check for oscillations. Increasing the input attenuator setting from 0 dB to 50 dB resulted in stable bias readings. It is suspected that leakage of the local oscillator through the input mixer produced a signal which stimulated a HEMT response. If the transistor is only marginally stable, a signal near the frequency of instability could cause sufficiently large responses to perturb the bias readings.

As the temperature was reduced further, the transistor was found to be unstable over an increasing range of I_{DS} values. At 18K, oscillations occurred for all I_{DS} greater than 1 mA. Several signals appeared on the spectrum analyzer; the major components were found to be at 4.2 and 7.3 GHz. Some means of increasing the DUT stability was required.

Three methods were considered to control the oscillations:

1. Addition of loss to the input circuit.
2. Addition of loss to the output circuit.
3. Addition of intentional feedback, (eg. increase source inductance).

Method (1) was rejected, since it would interfere with presenting the HEMT with the necessary high input reflection

coefficient expected near Γ_{opt}. Feedback (method 3) was left as a last resort, since the parameters measured with the apparatus would then require de-embedding, adding error to the results. Accurately estimating the value of the source inductance would also be difficult. Therefore, adding loss to the output circuit was attempted. A packaged SMA attenuator was not considered; a unit built by Midwest Microwave had been tested previously and failed at cryogenic temperatures.

A hole was drilled in both dielectric pieces of the DUT fixture, such that a "pill-pack" type of attenuator could be installed in the drain circuit stripline. A 3dB attenuator manufactured by KDI Triangle was inserted. Unfortunately, this device failed upon cooling due to a fracture in the package material, producing a DC open circuit in the drain stripline.

An attempt was then made to construct an attenuator suitable for cryogenic use. Two pieces of microwave absorbing material were cut and filed to fit in the holes left by the experiment with the "pill-pack" device. A strip of gold plated brass shimstock was then used to bridge the hole to complete the stripline. The lossy material was found to be conductive (DC) with an ohmmeter, so two small mylar film discs were cut with a paper punch and used as insulating shims between the ground planes and the absorbing pieces. A crude room temperature estimate of the loss was obtained by performing S-parameter measurements and assuming the change in the magnitude of S_{21} was due to a matched

attenuator. The loss thus estimated was 4 dB.

A definite improvement was noticed, as the HEMT remained stable for the cable calibration conditions, where the tuner reflection coefficient is near zero. However, tuning in the direction of Γ_{opt} (as estimated from the manufacturer's data) resulted in oscillations. Due to time constraints, further attempts to measure the noise parameters of a transistor were discontinued. A passive DUT measurement, which poses no stability problems, was performed instead in an attempt to verify the method of Chapter 3 by experiment and to ascertain that the noise measurement apparatus and software were functioning.

5.3.2 Passive DUT Measurements

A passive DUT was fabricated using the HEMT fixture and two pieces of gold plated brass shimstock. A small strip of shimstock was placed across the transistor pad to provide a continuous stripline from input to output. The attenuator arrangement described previously was used without modification. The second shim was placed across the input stripline conductor, so as to form two transmission line stubs.

Iterative tuning of the input stubs was performed until the noise parameters, computed from room temperature S-parameter measurements, reached an acceptable value of Γ_{opt}. Eventually the magnitude of Γ_{opt} at 3950 MHz was approximately 0.7, with an input reflection coefficient of 0.85. This approximation of a HEMT has very low available

gain, which increases the effect of the isolator noise contribution which is uncorrected.

Subsequent experiments with the apparatus yielded results which were confusing and inconclusive. Further investigation revealed that switching the relays in the cryostat changed the noise power reading. For the same relay settings, noise power data varied by up to 100% in some cases. To ensure measurement integrity, all noise power readings were obtained in sets from the HP8970 noise figure meter, and the mean and standard deviation were recorded. Despite the large variation between sets of readings (which should be nearly identical) the standard deviation of readings within any one set was always less than 1% and typically less than 0.1%.

Initially this behaviour was believed to be due to relay problems; however, it was found that readings obtained without the use of the cryogenic isolator and LNA did not exhibit such erratic behaviour. Subsequent testing showed the LNA to be unstable when cooled. The LNA was then placed outside the cryostat, and the noise power readings became stable. This also resulted in an undesirable increase in the system noise temperature.

S-parameters of the cooled passive DUT were then measured following the usual first-tier calibration of the S-parameter test system. The results at 3950 MHz are:

$$S_{11} = 0.745 \angle 156.2^{\circ}$$

$$S_{12} = 0.257 \angle -6.15^{\circ}$$

$$S_{21} = 0.261 \angle -6.45^{\circ}$$

$$S_{22} = 0.657 \angle 3.2^{\circ}$$

When de-embedded, the corrected S-parameters are:

$$S_{11} = 0.8696 \angle -163.2^{\circ}$$

$$S_{12} = 0.3210 \angle -77.5^{\circ}$$

$$S_{21} = 0.3228 \angle -71.9^{\circ}$$

$$S_{22} = 0.8110 \angle -176.9^{\circ}$$

From the above, the noise parameters can be computed, assuming a physical temperature of 13K:

$$T_N = 14.5412 \text{ K}$$

$$T_{min} = 9.1026 \text{ K}$$

$$\Gamma_{opt} = 0.7656 \angle 167.4^{\circ}$$

These values were used in the simulation of section 5.1. Based on this data, the DUT should exhibit a noise temperature of 30.1K when presented with the impedance of the bypass during cable calibration.

From the second-tier error vectors, and previous measurements of the HP346 diode noise source (with isolator) the available gain of the input cable (with bypass) was calculated using equation 3.17 to be 0.81298. The input cable calibration, based on hot and cold noise source temperatures of 5654K and 301K respectively, yielded bypass noise temperatures of 4620K and 268.1K when calculated using the method of section 3.6.3. Using this data, the input cable effective temperature was calculated using equation 3.44 to be 125.0K. Unfortunately, another estimate of this value was not available for comparison, although the value is at least physically reasonable.

A tuner loss compensation was then performed, yielding

equivalent noise temperatures at the tuner output of 4131.8K and 241.2K. The receiver noise temperature was high (661K), partly due to the LNA being relocated outside the cryostat. Initial data from the control program was discouraging, indicating an unreasonable T_{DUT} of 4303K. Changes in tuner setting provided no useful data, so the experiment was discontinued. Upon later examination of the program and data, an error was found in the control program. The correct value of T_{DUT} computed from the original data was found to be 75.4K. While not in close agreement with the estimated value of 30.1K, this indicates the experiment may have been working. However, this value is in good agreement with the value predicted by the simulation, shown to be about 75K in Figure 5.6(a). Comparison with the simulated value is not necessarily valid, since the actual properties of the isolator are not known. Due to numerous equipment and apparatus failures, along with other setbacks, there was insufficient time to continue the experiments.

Chapter 6

Recommendations and Conclusions

6.1 Recommendations

6.1.1 System Hardware

A large amount of time was spent during the course of this project dealing with hardware limitations. A surprising number of equipment failures occurred, and some upgrading would certainly be welcome. This section outlines recommendations for problems associated with the experimental hardware. The suggestions presented here are intended for the information of others continuing this research. Implementing all suggestions would probably prove too time consuming; however, it is hoped that future users will find these comments of value.

The S-parameter test system was a major source of inconvenience. Ideally this should be replaced with more modern equipment (HP8510 or equivalent); however, financial constraints at the time of writing make this unlikely. As shown in Chapter 3, the existing system is unsuitable for use with the LRL calibration method.

The software currently being used for the S-parameter test system could be upgraded to be more useful. Only the OSLT method of calibration is available, and the software runs on a computer (HP-85) which is too small to conveniently handle even the existing system. The system would be more useful if the software could be rewritten for a more suitable machine, and preferably include (or at least allow future addition of) the following:

1. S-parameter functions should be callable from a main control program, so that manual intervention between readings is not required.
2. Provision should be made to allow the user to set attenuator and function settings. This is useful both for polar display viewing and to remove RF signals from a particular port. Switching off the RF oscillator is not a suitable alternative as this results in sweeping signals emanating from the source port.
3. The digital attenuator circuit in the HP8410 is both noisy and occasionally unreliable. It has been observed to assume an incorrect value, or to change value due to static discharge from the operator to the chassis. Circuit improvement, or possibly feedback of the actual setting to the control computer, should be considered.
4. Provision could be made to accommodate more than one calibration scheme. If these routines could be made callable from outside programs, then the software would be useful for multi-tier calibrations.

The bias supplies (constructed in this laboratory) are a potential source of trouble. The feedback design permits setting V_{DS} and I_{DS} while the supply automatically adjusts V_{GS} to maintain these requirements. However, the transistor being powered forms part of the control loop, and the control system may not be stable for all devices. Although

no difficulties which were proven to be caused by the supplies were experienced with this project, two incidents which suggest instabilities of this type were observed by the author.

First, a room temperature HEMT was seen to oscillate at microwave frequencies in such a manner that the frequency of oscillation varied greatly, as did the bias values on the power supply indicators. Replacement with a commercial supply (HP8717B) resulted in stable bias values, and a stable oscillation frequency of the HEMT. In the second event, the noise temperature of a three stage 1.4 GHz LNA was measured to be 125K with one of the suspect power supplies, but achieved 65K when the bias supply was replaced with a similar unit in which the grounding had been improved. This suggests that there are some problems with the unmodified units.

The author experienced difficulties with a 4 GHz two stage LNA (also built in-house). Erratic behaviour and/or oscillations occurred when the unit was cooled. Bias fluctuations were observed, which suggests that the bias supplies previously implicated may be partly responsible for the instability. Future experimenters are cautioned against assuming that an amplifier is stable, and that good room temperature performance guarantees acceptable behaviour when cooled.

The HP8970 noise figure meter frequency indication is 3MHz high. For example, when the instrument reads 1500 MHz, the 4 MHz wide passband is actually centered at about 1497

KHz. The first local oscillator is also somewhat unstable. An experiment to verify this revealed a maximum drift of 190 KHz over a six hour period. One remedy is to use an external mixer, and a source locking counter to phase lock the difference between the first LO and the external LO. This technique is described in a thesis by Eric Valk [6.1].

Perhaps the most difficult problem to solve is keeping an active DUT stable during experiments. The author's attempt to incorporate an attenuator proved inadequate. A possible alternative might be to place a series or shunt resistor at the output of the HEMT. In the case of a shunt resistance, it may also be possible to add a blocking capacitor, so as not to affect the bias of the transistor. Obviously the solution must be useable at cryogenic temperatures. Perhaps chip resistors attached with indium based solder would be suitable.

6.1.2 Experimental Procedures

This section contains recommendations for future research into the methods described in Chapters 2 and 3. Although the noise measurement technique used was shown to be correct by the simulation performed in section 5.1, there was insufficient time to assess the effect of experimental error by performing a sensitivity analysis. The noise parameter experiments may be sensitive to the accuracy of S-parameter and reflection coefficient errors. The sensitivity of the input cable calibration to the accuracy of the available gain estimate would also be of interest.

Accuracy of noise measurement could be improved by direct measurement of the DUT output reflection coefficient. (In the author's experiments, this was computed from the DUT S-parameters and the tuner output reflection coefficient.) However, direct measurement would incur an additional relay operation and measurement sequence for each noise temperature estimate.

Compensation for the isolator noise could be added to enhance accuracy. There are several possible ways to approach this problem; one method is to assess the receiver noise temperature for a sufficient number of input impedances to permit calculation of the receiver noise parameters. Its noise contribution could then be calculated properly for any DUT output conditions.

6.2 Conclusions

Despite initial concerns regarding the use of a mechanical tuner at cryogenic temperatures, this part of the apparatus worked well. The stepper motor controller cards, motor mechanism and tuner worked without difficulty for all the experiments. Room temperature measurements of the tuner showed the tuner to be lossy, and it may be possible to improve the slug design to reduce dielectric losses. No mechanical or electrical problems were encountered with the stripline package design, and this type of fixture can be recommended for future applications.

Equations were presented for the 3ST calibration method, for both twelve and eight error vector models. A

sensitivity analysis for the twelve vector solutions of the OSLT, 3ST, and LRL methods were performed, and the results clearly demonstrate that the LRL method is not applicable to the hardware of the HP8410 system. The analysis technique presented is easily used by others to assess the measurement sensitivity of a particular configuration of S-parameter instrumentation.

The most useful result of the thesis is the new input cable calibration method, which can also be used to estimate both the equivalent noise temperature at the end of the cable, and the effective temperature of the cable itself. Noise-temperature diagrams were used to derive this technique in a reasonably intuitive manner. Additionally, a similar analysis was used to present an alternative derivation to the tuner loss compensation results of Martines and Sannino. New results were also presented which address the substitution and insertion of two-ports in a noise measurement system.

Despite a large number of hardware failures, and the disappointing outcome of some of the experiments, a number of very useful results, applicable to both noise and scattering parameter measurements, have been produced and presented.

References

1.1 Johnson, J. B.; "Thermal Agitation of Electricity in Conductors", Physical Review, Vol. 32., July 1928, pp. 97 - 109.

1.2 Nyquist, H.; "Thermal Agitation of Electric Charge in Conductors", Physical Review, Vol. 32., July 1928, pp. 110 - 113.

1.3 Friis, H.T.; "Noise Figures of Radio Receivers", Proceedings of the IRE, Vol. 32, 1944, pp. 419 - 422.

1.4 Rothe, H. and Dahlke, W.; "Theory of Noisy Fourpoles", Proceedings of the IRE, Vol. 44, June 1956, pp. 811 - 818.

1.5 IRE Subcommittee on Noise; "IRE Standards on Methods of Measuring Noise in Linear Twoports, 1959", Proceedings of the IRE, Vol. 48, Jan. 1960, pp. 60 - 68. 68.

2.1 Soares, R. (Ed.); "GaAs MESFET Circuit Design", c. 1988 Artech House, Inc., 685 Canton Street, Norwood, MA, chapter 2.

2.2 Gonzalez, Guillermo; "Microwave Transistor Amplifiers", c. 1984 Prentice Hall, Inc., Englewood Cliffs, N.J., Chapter 1.

2.3 Engen, Glenn F.; "The Six-Port Reflectometer : An Alternative Network Analyzer", IEEE MTT-25, No 12, Dec 1977, pp 1075 - 1080.

2.4 Hackborn, Richard A.; "An Automatic Network Analyzer System:, Microwave Journal, May 1968, pp 45-52.

2.5 Hewlett Packard; "Network Analyzer 8410A and Harmonic

Frequency Converter 8411A Operating and Service Manual", Hewlett Packard Co., 1501 Page Mill Road, Palo Alto, CA., c.1968.

2.6 Speciale, R.A.; Grabowski, R.E.; Franzen, N.R.; "Accurate Scattering Parameter Measurements on Non-Connectable Microwave Networks", Proc. 6th European Microwave Conference, 1976., pp 210 - 214.

2.7 Fitzpatrick, Jim; "Error Models for Systems Measurement", Microwave Journal, May 1978, pp 63 - 66.

2.8 Franzen, N.R.; Speciale, R.A.; "A New Procedure for System Calibration and Error Removal in Automated S-Parameter Measurements", Proc. 5th European Microwave Conference, 1975., pp. 69-73.

2.9 Gonzalez, Guillermo; "Microwave Transistor Amplifiers", c. 1984 Prentice Hall, Inc., Englewood Cliffs, N.J., pp. 83 - 86.

2.10 Chau, Ming-Chun; "Microprocessor-Controlled ANA System for De-Embedding FET Parameters", M.Sc. Thesis, University of Alberta, Edmonton, 1984.

2.11 Maury, M. A. Jr., March, S. L. and Simpson G. R.; "LRL Calibration of Vector Automatic Network Analyzers", Microwave Journal, May 1987, pp. 387 - 392.

2.12 Hoer, C. A. and Engen, G. F.; "Calibrating a Dual Six-port or Four-port for Measuring Two-ports with any Connectors", IEEE MTT-S Digest 1986, pp. 665 - 668.

2.13 E.C.Valk, Private Conversation, Oct. 1989.

2.14 Soares, R. (Ed.); "GaAs MESFET Circuit Design", c. 1988 Artech House, Inc., 685 Canton Street, Norwood,

MA 02062, pp. 198.

3.1 Meer, David E.; "Noise Figures", IEEE Proceedings of the National Aerospace and Electronics Conference 1989, Vol. 1 of 4, pp. 269-276.

3.2 IRE Subcommittee 7.9 on Noise; "Representation of Noise in Linear Twoports", Proceedings of the IRE, Jan. 1960, pp. 69-74.

3.3 Lange, Julius; "Noise Characterization of Linear Twoports in Terms of Invariant Parameters", IEEE Journal of Solid-state Circuits, Vol. SC-2, No. 2, June 1967, pp. 37-40.

3.4 Vendelin, George D.; "Feedback Effects on the Noise Performance of GaAs MESFETS", IEEE MTT-S Int. Microwave Symp., 1975, pp. 324-326.

3.5 Pospieszalski, Marian W.; "Modelling of Noise Parameters of MESFET's and MODFET's and Their Frequency and Temperature Dependence", IEEE MTT-37, No. 9, Sept. 1989, pp. 1340 - 1350.

3.6 Gupta, Madhu S., "Impossibility of Linear Two-port Noise-parameter Measurement with a Single Temperature Noise Source", IEEE IM-32, No. 2, Sept. 1983, pp, 443-445.

3.7 Hewlett-Packard; "Fundamentals of RF and Microwave Noise Figure Measurements", HP Application Note 57-1, Hewlett Packard Co., 1501 Page Mill Road, Palo Alto, CA., July 1983, pp.7-12.

3.8 Caruso, Giuseppe and Sannino, Mario; "Analysis of Frequency-Conversion Techniques in Measurements of

Microwave Transistor Noise Temperatures", IEEE MTT-25, No. 11, Nov. 1977, pp. 870-873.

3.9 Strid, Eric W.; "Measurement of Losses in Noise-Matching Networks", IEEE MTT-29, No. 3, Mar. 1981, pp. 247-252.

3.10 Martines, G. and Sannino, M.; "A Method for Measurement of Losses in the Noise-Matching Microwave Network While Measuring Transistor Noise Parameters", IEEE MTT-35, No. 1, Jan. 1987, pp.71-75.

3.11 Kuhn, Niclas J.; "Curing a Subtle But Significant Cause of Noise Figure Error", Microwave Journal, June 1984, pp. 85-98.

3.12 Weinreb, Sander; "Low-Noise Cooled GASFET Amplifiers", IEEE MTT-28, No. 10, Oct. 1980, pp. 1041-1054.

3.13 Pospieszalski, Marian W., "On the Measurement of Noise Parameters of Microwave Two-Ports", IEEE MTT-34, No. 4, Apr. 1986, pp. 456-459.

3.14 Haus, H. A. and Adler, R. B.; "Optimum Noise Performance of Linear Amplifiers", Proceedings of the IRE, Aug. 1958, pp. 1517-1533.

3.15 Hartmann, Karl and Strutt, Max J. O.; "Changes of the Four Noise Parameters Due to General Changes of Linear Two-Port Circuits", IEEE ED-20, No. 10, Oct. 1973, pp. 874-877.

3.16 Engberg, Jacob; "Simultaneous Input Power Match and Noise Optimization Using Feedback", Dig. Tech. Papers, European Microwave Conference, Sept. 1974, pp. 385-389.

3.17 Iversen, S.; "The Effect of Feedback on Noise Figure",

Proc. IEEE, Vol. 63, Mar. 1975, pp. 540-542.

3.18 Niclas, Karl B.; "The Exact Noise Figure of Amplifiers with Parrallel Feedback and Lossy Matching Circuits:, IEEE MTT-30, No. 5, May 1982, pp. 832-835.

4.1 Sando, S.; "A Two Stage 3.7 to 4.2 GHz GaAs FET LNA Using Two NE21889's or Two NE72089's", Microwave Journal, Oct. 1981, pp. 107 - 110.

4.2 Bahl, I. and Bhartia,P.; "Microwave Solid State Cicuit Design", John Wiley and Sons, Inc., New York, 1988, pp. 40.

4.3 Gunston, M. A. R.; "Microwave Transmission-line Impedance Data", Van Nostrad Reinhold Company, London, 1971, pp 64.

4.4 Gunston, M. A. R.; "Microwave Transmission-line Impedance Data", Van Nostrad Reinhold Company, London, 1971, pp 6.

4.5 Acarnley, P.P.; "Stepping Motors: a guide to modern theory and practice (IEE Control Engineering Series; no. 19)" 1982, Peter Peregrinus Ltd., Stevenage, UK on behalf of the Institution of Electrical Engineers, ch. 1 and 2.

4.6 Deeprose, K. and Plato, J.; "General Purpose Interface Card," University of Alberta LNA Laboratory internal manual.

4.7 Lancaster, D.; "TTL Cookbook", Howard W. Sams and Co., Inc., 1974, pp. 269-275.

4.8 Lancaster, D.; "TTL Cookbook", Howard W. Sams and Co., Inc., 1974, pp. 209-211.

5.1 Pospieszalski, M.; "Low-Noise. 8.0 - 8.5 GHz, Cooled, GASFET Amplifier", NRAO Electronics Division Internal Report No. 254, NRAO, Dec. 1984.

5.2 Pospieszalski, M., Weinreb, S., Norrod, R. D. and Harris, R.; "FET's and HEMT's at Cryogenic Temperatures- Their Properties and Use in Low-Noise Amplifiers", IEEE MTT-36, No. 3, March 1988, pp. 552 - 559.

6.1 Valk, E. C.; "Techniques of Microwave Noise Measurement on Cooled Transistors", Ph.D. Thesis, University of Alberta, Edmonton, 1990.

Appendix I Noise Parameter Conversions

Equations are presented for the conversion between various sets of noise parameter representations. Reference is made to Figures in the thesis text where applicable.

A. $\langle v^2\rangle$, $\langle i^2\rangle$, α_{vi} (see Fig. 1.1(d)) to
$\langle v_1^2\rangle$, $\langle v_2^2\rangle$, α_{12} (see Fig. .1.(c))

$$\langle v_1^2\rangle = \langle v^2\rangle + |Z_{11}|^2\langle i^2\rangle - 2(\langle v^2\rangle\langle i^2\rangle)^{1/2}\mathrm{Re}\{\alpha_{vi}^* Z_{11}\}$$

$$\langle v_2^2\rangle = |Z_{21}|^2\langle i^2\rangle$$

$$\alpha_{12} = \frac{Z_{21}^*\left(Z_{11}\langle i^2\rangle - (\langle v^2\rangle\langle i^2\rangle)^{1/2}\alpha_{vi}\right)}{(\langle v_1^2\rangle\langle v_2^2\rangle)^{1/2}}$$

Inverse conversion:

$$\langle v^2\rangle = \langle v_1^2\rangle + \frac{|Z_{11}|^2\langle v_2^2\rangle}{|Z_{21}|^2} - 2(\langle v_1^2\rangle\langle v_2^2\rangle)^{1/2}\mathrm{Re}\left\{\alpha_{12}^* \frac{Z_{11}}{Z_{21}}\right\}$$

$$\langle i^2\rangle = \frac{\langle v_2^2\rangle}{|Z_{21}|^2}$$

$$\alpha_{vi} = \left(\frac{Z_{11}\langle v_2^2\rangle}{|Z_{21}|^2} - \frac{(\langle v_1^2\rangle\langle v_2^2\rangle)^{1/2}\alpha_{12}}{Z_{21}^*}\right)(\langle v^2\rangle\langle i^2\rangle)^{-1/2}$$

Note: For all correlation coefficients, $|\alpha| \leq 1$.

B. $\langle v^2 \rangle$, $\langle i^2 \rangle$, α_{vi} (see Fig. 1.1(d)) to F_{min}, Y_{opt}, N

$$\gamma = \gamma_r + j\gamma_i = \alpha_{vi}$$

$$|Y_{opt}|^2 = \frac{\langle i^2 \rangle}{\langle v^2 \rangle}$$

$$Y_{opt} = |Y_{opt}| \left((1-\gamma_i^2)^{1/2} + j\gamma_i \right)$$

$$N = \frac{1}{4kT_0\Delta f} \left((1-\gamma_i^2) \langle v^2 \rangle \langle i^2 \rangle \right)^{1/2}$$

$$F_{min} = 1 + \frac{(\langle v^2 \rangle \langle i^2 \rangle)^{1/2}}{2kT_0\Delta f} \left(\gamma_r + (1-\gamma_i^2)^{1/2} \right)$$

Inverse Conversion:

$$\langle v^2 \rangle = \frac{4kT_0\Delta f N}{Re\{Y_{opt}\}}$$

$$\langle i^2 \rangle = \langle v^2 \rangle |Y_{opt}|^2$$

$$\langle vi^* \rangle = \langle v^2 \rangle \left(\frac{(F_{min} - 1)\, Re\{Y_{opt}\}}{2N} - Y_{opt}^* \right)$$

$$\alpha_{vi} = \frac{\langle vi^* \rangle}{(\langle v^2 \rangle \langle i^2 \rangle)^{1/2}} \qquad \text{where} \quad |\alpha_{vi}| \leq 1$$

Associated noise parameter equation:

$$F = F_{min} + \frac{N|Y_S - Y_{opt}|^2}{Re\{Y_S\} Re\{Y_{opt}\}}$$

C. F_{min}, N, Y_{opt} to T_{min}, N, Γ_{opt}

N remains unchanged.

$$T_{min} = T_0(F_{min} - 1)$$

$$\Gamma_{opt} = \frac{1 - Y_{opt}}{1 + Y_{opt}}$$

Inverse conversion:

$$F_{min} = \frac{T_{min}}{T_0} + 1$$

$$Y_{opt} = \frac{1 - \Gamma_{opt}}{1 + \Gamma_{opt}}$$

Associated noise parameter equations:

$$F = F_{min} + \frac{N\,|Y_S - Y_{opt}|^2}{Re\{Y_S\}Re\{Y_{opt}\}}$$

$$T = T_{min} + \frac{4NT_0|\Gamma_{opt} - \Gamma_S|^2}{(1-|\Gamma_S|^2)(1-|\Gamma_{opt}|^2)}$$

Note: $T_{min} \leq 4NT_0$ for any physical two-port [3.5].

D. F_{min}, R_n, Y_{opt} to G_n, R_{n0}, Y_{cor} (from Vendelin [3.4])

$$G_n = R\,(G_{opt}^2 - G_{cor}^2) \qquad \text{where} \qquad G_{opt} = \mathrm{Re}\{Y_{opt}\}, \quad G_{cor} = \mathrm{Re}\{Y_{cor}\}$$

$$R_{n0} = R_n$$

$$Y_{cor} = G_{cor} + jB_{cor} \qquad \text{where} \qquad G_{cor} = \frac{(F_{min}-1)}{2R_n} - G_{opt}, \quad B_{cor} = -B_{opt}$$

Inverse Conversion:

$$G_{opt} = \left(\frac{G_n + R_{n0}G_{cor}^2}{R_{n0}} \right)^{1/2}$$

$$F_{min} = 1 + 2R_{n0}(G_{cor} + G_{opt})$$

$$R_n = R_{n0}$$

$$Y_{opt} = G_{opt} + jB_{opt} \qquad \text{where} \qquad B_{opt} = -B_{cor}$$

Associated noise parameter equations:

$$F = F_{min} + \frac{R_n}{G_S}\,|Y_S - Y_{opt}|^2$$

$$F = 1 + \frac{G_n}{G_S} + \frac{R_{n0}}{G_S}\,|Y_S - Y_{cor}|^2$$

E. F_{min}, r_n, Y_{opt} to F_{min}, r_n, Γ_{opt}

$$\Gamma_{opt} = \frac{1 - Y_{opt}}{1 + Y_{opt}}$$

Inverse conversion:

$$Y_{opt} = \frac{1 - \Gamma_{opt}}{1 + \Gamma_{opt}}$$

Associated equations:

$$F = F_{min} + \frac{r_n}{g_s} |Y_s - Y_{opt}|^2 \qquad \text{where } g_s = \text{Re}\{Y_s\}$$

$$F = F_{min} + \frac{4r_n |\Gamma_s - \Gamma_{opt}|^2}{(1-|\Gamma_s|^2)\ |1+\Gamma_{opt}|^2}$$

Notes:

1. Y_s, Y_{opt}, r_n, and g_s are normalized with respect to Z_0.
2. The following relation is useful for the derivation of the equations:

$$g_s |1 + \Gamma_s|^2 = 1 - |\Gamma_s|^2$$

Appendix II Initial Configuration of J12 on stepper motor control card

Patch Area Jumpers:

1 - 38

5 - 39

6 - 37

8 - 48

9 - 47

10 - 46

12 - 32

14 - 43

15 - 42

16 - 41

18 - 31

19 - 30

20 - 29

21 - 28

22 - 27

23 - 26

24 - 25

The following pins have no connections:

2, 3, 4, 7, 11, 12, 13,

33, 34, 35, 36, 40, 44, 45.

Appendix III Table of Motor Control Card IC functions

IC	Device	Function
U1	555	free running oscillator
U2	74HC00	run/stop logic
U3	74HC74	one-and-only-one synchronizer
U4	74HC76	walking ring counter
U5	74HC00	ϕ_1 and ϕ_2 decode logic
U6	74LS00	ϕ_1 and ϕ_2 sequence (direction) logic
U7	74HC251	IEEE-488 talk handshake circuit
U8	74HC06	HOME / INDEX logic
U9	74HC10	misc. logic
U10	74HC86	card address decoding
U11	74LS569	tristate binary counter
U12	74LS569	tristate binary counter
U13	4N35	ϕ_1 drive opto-isolator
U14	4N35	ϕ_2 drive opto-isolator
U15	4N35	$\overline{\phi_1}$ drive opto-isolator
U16	4N35	$\overline{\phi_2}$ drive opto-isolator
U17	74LS14	debouncing / misc. logic
U18	74HC157	manual / remote selector logic
U19	74LS190	BCD index counter
U20	74LS190	BCD index counter
U21	74LS190	BCD index counter
U22	7447	7-segment LED display driver for BCD counter
U23	7447	7-segment LED display driver for BCD counter
U24	7447	7-segment LED display driver for BCD counter

Appendix IV Remote Command (IEEE-488) Summary

Output Byte Format

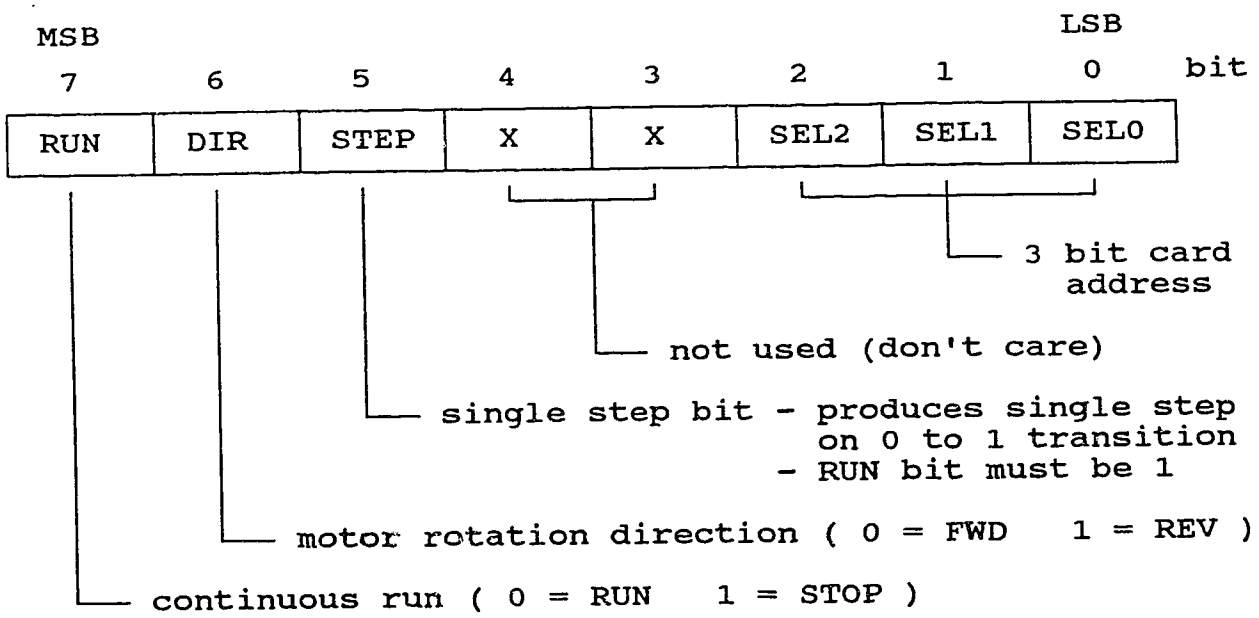

CONTROL COMMANDS (HP-86 SYNTAX)

GENERAL CONTROL OUTPUT

OUTPUT 712 USING "#,B";*byte*

where - 712 is the IEEE-488 address of the associated interface card

- *byte* is the output byte as above

Appendix IV (continued)

SINGLE STEP CONTROL

OUTPUT 712 USING "#,B";*byte*

where bit 5 = 0 and bit 7 = 1 in *byte*

motor steps in selected direction, provided bit 5 was previously a 1

OUTPUT 712 USING "#,B";*byte*

where bit 5 = 1 and bit 7 = 1 in *byte*

no motor motion, but bit 5 is reset for subsequent steps

POSITION COUNTER READ

OUTPUT 712 USING "#,B";*byte*

where address bits of *byte* select the desired controller card

Note: motor can be running or stopped (as selected by *byte*) during read

ENTER 712;N

reads the counter register value into variable N

N = 255 - N

corrects for inverted data

Note: The position counter can be read even if the card is in manual control mode.

Appendix V Table of Motor Control Card Jumpers

Jumper	Function	
J1	SEL 0	Sets the motor controller card 3 bit address. Shorting a jumper block corresponds to a 0.
J2	SEL 1	
J3	SEL 2	
J4	REVERSE	Selects limit switch operation. Jumper only one. Set J10 first.
J5	FORWARD	
J6	DEFEAT	
J7	REVERSE	Selects home switch operation. Jumper only one. Set J10 first.
J8	FORWARD	
J9	DEFEAT	
J10	Jumper left or right to match motor rotation with front panel FWD/REV switch labelling.	
J11	Selects counter increment direction (independent of J10).	
J12	VME bus interface patch area. See schematic diagram for application and Appendix II for the initial configuration.	

Note: See Figure 4.19 for location of jumper blocks.